# Structural characterization of intermediate and metastable phases by electron microscopy

Dissertation zur Erlangung des Grades

"Doktor der Naturwissenschaften"

im Fachbereich Chemie, Pharmazie und Geowissenschaften

der Johannes Gutenberg-Universität Mainz

vorgelegt von

**Iryna Andrusenko**

geboren in Romny, Ukraine

Mainz, 2014

# Erklärung

Die vorliegende Dissertation wurde zwischen April 2009 und Juli 2014 am Institut für Anorganische Chemie und Analytische Chemie der Johannes Gutenberg Universität Mainz angefertigt.

Ich versichere hiermit, dass ich die Dissertation selbstständig verfasst habe, so wie alle angewandten Quellen und Hilfsmittel angegeben habe.

Iryna Andrusenko, Mainz, im Juli 2014

# Abstract

Structure characterization of nanocrystalline intermediates and metastable phases is of primary importance for a deep understanding of synthetic processes undergoing solid-to-solid state phase transitions. Understanding the evolution from the first nucleation stage to the final synthetic product supports not only the optimization of existing processes, but might assist in tailoring new synthetic paths. A systematic investigation of intermediates and metastable phases is hampered because it is impossible to produce large crystals and only in few cases a pure synthetic product can be obtained. Structure investigation by X-ray powder diffraction methods is still challenging on nanoscale, especially when the sample is polyphasic. Electron diffraction has the advantage to collect data from single nanoscopic crystals, but is limited by data incompleteness, dynamical effects and fast deterioration of the sample under the electron beam. Automated diffraction tomography (ADT), a recently developed technique, making possible to collect more complete three-dimensional electron diffraction data and to reduce at the same time dynamical scattering and beam damage, thus allowing to investigate even beam sensitive materials (f.e. hydrated phases and organics). At present, ADT is the only technique able to deliver complete three-dimensional structural information from single nanoscopic grains, independently from other surrounding phases. Thus, ADT is an ideal technique for the study of on-going processes where different phases exist at the same time and undergo several structural transitions. In this study ADT was used as the main technique for structural characterization for three different systems and combined subsequently with other techniques, among which high-resolution transmission electron microscopy (HRTEM), cryo-TEM imaging, X-ray powder diffraction (XRPD) and energy disperse X-ray spectroscopy (EDX).

As possible laser host materials, i.e. materials with a broad band emission in the near-infrared region, two unknown phases were investigated in the **ternary oxide system $M_2O$-$Al_2O_3$-$WO_3$ ($M$ = K, Na).** Both phases exhibit low purity as well as non-homogeneous size distribution and particle morphology. The structures solved by ADT are also affected by pseudo-symmetry.

Sodium titanate nanotubes and nanowires are both **intermediate products in the synthesis of $TiO_2$ nanorods** which are used as additives to colloidal $TiO_2$ film for improving efficiency of dye-sensitized solar cells (DSSC). The structural transition from nantubes to nanowires was investigated in a step by step time-resolved study. Nanowires were discovered to consist of a hitherto unknown phase of sodium titanate. This new phase, typically affected by pervasive defects like mutual layer shift, was structurally determined *ab-initio* on the basis of ADT data.

The third system is related with **calcium carbonate** nucleation and early crystallization. The first part of this study is dedicated to the extensive investigations of calcium carbonate formation in a step by step analysis, up to the appearance of crystalline individua. The second part is dedicated to the structure determination by ADT of the first-to-form anhydrated phase of $CaCO_3$: vaterite. An exhaustive structure analysis of vaterite had previously been hampered by diffuse scattering, extra periodicities and fast deterioration of the material under electron irradiation.

# Zusammenfassung

Zum besseren Verständnis von Syntheseprozessen, die über einen fest-fest-Phasenübergang ablaufen, müssen die beteiligten nanokristallinen Zwischenstufen und metastabilen Phasen strukturell charakterisiert werden. Ein tieferer Einblick in diesen Ablauf, von der ersten Nukleationsphase bis hin zum Endprodukt, unterstützt nicht nur die Optimierung bestehender Prozesse, sondern kann auch bei der Entwicklung neuer Synthesewege helfen. Eine systematische Untersuchung der Zwischenprodukte und metastabilen Phasen durch Rötgenbeugungsmethoden ist stark eingeschränkt, da oft keine Einkristalle vorliegen und nur in wenigen Fällen reine Syntheseprodukte erhalten werden können. Eine Strukturaufklärung mit Hilfe der Röntenpulverdiffraktion ist im nanokristallinen Bereich immer noch sehr schwierig, besonders für mehrphasige Materialien. Vorteil der Elektronenbeugung ist es, dass Daten eines einzelnen Nanokristall gesammelt werden können, sie wird aber limitiert durch die geringe erreichbare Datenmenge, dynamische Beugungseffekte und Elektronenstrahlschäden in der Probe. Die automatische Beugungstomographie (ADT), eine kürzlich entwickelte Methode, erlaubt es, wesentlich vollständigere dreidimensionale Daten mit stark reduzierten dynamischen Effekten zu sammeln. Strahlenschäden sind hier so stark verringert, dass sogar strahlempfindliche Materialien, wie Hydratphasen oder organische Materialien, vermessen werden können. Momentan ist ADT die einzige Methode, die vollständige dreidimensionale Strukturinformationen von nanoskopischen Körnern liefert. Deswegen ist ADT die ideale Technik, um Prozessabläufe zu untersuchen, in denen mehrere Phasen gleichzeitig existieren und sich ineinander umwandeln. In dieser Arbeit wurde ADT als Hauptmethode zur strukturellen Charakterisierung dreier verschiedener Systeme verwendet und die Ergebnisse mit anderen Techniken untermauert (Hochauflösende Transmissionselektronenmikroskopie (HRTEM), Cryo-TEM Abbildung, Röntgenpulverdiffraktometrie (XRPD) und energiedispersive Röntgen-spektroskopie (EDX)).

Als mögliche Laser-Wirtsmaterialien wurden zwei unbekannte Phasen des **ternären oxidischen Systems $M_2O$-$Al_2O_3$-$WO_3$ ($M$ = K, Na)** untersucht. Beide Phasen zeigen eine schlechte Reinheit und haben keine einheitliche Größenverteilung und Partikelmorphologie. Die mit ADT gelösten Strukturen wiesen beide eine Pseudosymmetrie auf.

Natriumtitanat Nanoröhren und Nanodrähte sind **Zwischenprodukte in der Synthese von $TiO_2$ Nanostäbchen.** Diese sind Additive in einem kolloidalen $TiO_2$ Film, der als Elektrodenmaterial für Farbstoff Solarzellen (DSSC) genutzt wird. Der strukturelle Übergang von Nanoröhren zu Nanodrähten wurde zeitaufgelöst untersucht. Es wurde festgestellt, dass Nanodrähte aus einer bisher unbekannten Natriumtitant-Phase bestehen. Diese neue Phase, die *ab-initio* auf der Basis von ADT Daten gelöst wurde, weist typische Defekte wie Schichtversetzungen auf.

Das dritte System liegt im Bereich der C**alciumcarbonat** Keimbildung und frühen Kristallisation. Im ersten Teil der Untersuchung wurde eine schrittweise Analyse dieses Vorgangs, bis hin zur Bildung einzelner Kristallite durchgeführt. Im zweiten Teil wurde eine

ADT Strukturaufklärung der ersten Anhydratphase von $CaCO_3$, dem Vaterite, durchgeführt. Eine ausführliche Strukturanlayse von Vaterit war bislang durch das Auftreten starker diffuser Streuung, zusätzlicher Periodizitäten und der schnellen Zerstörung des Materials im Elektronenstrahl nicht möglich.

# List of Publications

1. F. Porrati, R. Sachser, M. Strauss, **I. Andrusenko**, T. Gorelik, U. Kolb, L. Bayarjargal, B. Winkler, M. Huth (**2010**) "Artificial Granularity in Two-Dimensional Arrays of Nanodots Fabricated by Focused-Electron-Beam-Induced Deposition" *Nanotechnology* **21**: 375302 (7pp). DOI: 10.1088/0957-4484/21/37/375302.

2. **I. Andrusenko**, E. Mugnaioli, T.E. Gorelik, D. Koll, M. Panthöfer, W. Tremel, U. Kolb (**2011**) "Structure Analysis of Titanate Nanorods by Automated Electron Diffraction Tomography" *Acta Crystallogr. B* **67**: 218-225. DOI: 10.1107/S0108768111014534.

3. J.-L. Zhuang, K. Lommel, D. Ceglarek, **I. Andrusenko**, U. Kolb, S. Maracke, U. Sazama, M. Fröba, A. Terfort (**2011**) "The Synthesis of a New Copper-Azobenzene Dicarboxylate Framework in Form of Hierarchical Bulk Solids and Thin Films without and with Patterning" *Chem. Mater.* **23**: 5366-5374. DOI: 10.1021/cm2021092.

4. E. Mugnaioli, **I. Andrusenko**, T. Schüler, L. Niklas, R.E. Dinnebier, M. Panthöfer, W. Tremel, U. Kolb (**2012**) "Ab initio Stucture Determination of Vaterite by Automated Electron Diffraction" *Angew. Chem., Int. Ed.* **51**: 7041-7045. DOI: 10.1002/anie.201200845.

5. S. Fütterer, **I. Andrusenko**, U. Kolb, W. Hofmeister, P. Langguth (**2013**) "Structural Characterization of Iiron Oxide/Hydroxide Nanoparticles in Nine Different Parenteral Drugs for the Treatment of Iiron Deficiency Anaemia by Electron Diffraction (ED) and X-ray Powder Diffraction (XRPD)" *J. Pharm. Biomed. Anal.* **86**:151-160. DOI: 10.1016/j.jpba.2013.08.005.

6. D. Koll, **I. Andrusenko**, E. Mugnaioli, A. Birkel, M. Panthöfer, U. Kolb, W. Tremel (**2013**) "Snapshots of the Formation of $NaTi_3O_6(OH)\cdot 2H_2O$ Nanowires: A Time-Resolved XRD/HRTEM Study" *Z. Anorg. Allg. Chem.* **639**: 2521–2526. DOI: 10.1002/zaac.201300411.

7. M. Dietzsch, **I. Andrusenko**, R. Branscheid, U. Kolb, W. Tremel (**2014**) "Snapshots of Calcium Carbonate Formation – A Step by Step Analysis" (in preparation).

8. **I. Andrusenko**, E. Mugnaioli, Y. Krysiak, T.E. Gorelik, U. Kolb, D. Nihtianova (**2014**) "Structural Insights about $M_2O$-$Al_2O_3$-$WO_3$ ($M$ = Na, K) System by Automated Electron Diffraction Tomography " *Acta Crystallogr. B* (in preparation).

# Content

# List of Figures

3.10 TEM overview images of the sodium titanate sample after 10 minutes heating ramp and 5 minutes of reaction time ("5 minute sample").

3.11 TEM overview images of the sodium titanate sample after 10 minutes heating ramp and 10 minutes of reaction time ("10 minute sample").

3.12 TEM overview images of the sodium titanate sample after 10 minutes heating ramp and 120 minutes of reaction time ("120 minute sample").

3.13 Thermogravimetric curve of sodium titanate nanowires.

3.14 Reconstructed three-dimensional diffraction volume obtained by ADT data from the final product.

3.15 Final model of sodium titanate $NaTi_3O_6(OH)\cdot 2H_2O$ structure.

3.16 Rietveld fit of $NaTi_3O_6(OH)\cdot 2H_2O$ structure.

3.17 Scheme of $CaCO_3$ precipitation (slow method).

3.18 TEM snapshot taken during the second stage of the $CaCO_3$ formation (slow method).

3.19 TEM snapshots taken during the third stage of the $CaCO_3$ formation (slow method).

3.20 TEM snapshots taken during the third stage of the $CaCO_3$ formation (fast method).

3.21 Cryo-TEM snapshots taken 60 seconds after the beginning of third stage of the $CaCO_3$ formation (fast method).

3.22 SEM and STEM overview images of typical vaterite nanocrystals from the aqueous synthesis.

3.23 STEM overview images of vaterite nanoparticles from non-aqueous synthesis.

3.24 Reconstructed three-dimensional diffraction volume obtained by ADT data from a vaterite crystal.

3.25 Comparison of different vaterite cells.

3.26 Final 2-layer model of vaterite crystal structure.

3.27 Diffuse scattering and local modulation along **c*** in vaterite structure (NED observation).

3.28 Diffuse scattering and local modulation along **c*** in vaterite structure (HRTEM confirmation).

3.29 Final 6-layer model of vaterite crystal structure.

3.30 Selected projections of vaterite 2-layer and 6-layer models.

3.31 Structure refinement of vaterite 2-layer and 6-layer models against XRPD data.

4.1 Phase diagram of $K_2O$-$Al_2O_3$-$WO_3$ system.

4.2 Structurally related phases in the $M_2O$-$Al_2O_3$-$WO_3$ system.

4.3 Phase diagram of $Na_2O$-$Al_2O_3$-$WO_3$ system.

4.4 Summary of the growth steps of $NaTi_3O_6(OH)\cdot 2H_2O$ nanowires.

4.5 Comparison of $NaTi_3O_6(OH)\cdot 2H_2O$ with related structures.

4.6 Structure comparison between 2-layer monoclinic model of vaterite and high-temperature polymorph of $(Y_{0.92}Er_{0.08})BO_3$.

# List of Tables

# Chapter I. Introduction and Overview

## 1.1 Crystallization process

Crystallization is a general term describing several different phenomena related to the formation of a periodic (lattice) structure by the precipitation from a solution or a melt, or more rarely by the direct sublimation from a gas [Mullin, 2001]. In fact, it is one of the most simple self-assembly processes to create order from the atomic to the macroscopic scale [Cölfen & Antonietti, 2008]. Either in natural or artificial environments, crystallization often implies the simultaneous and dynamical formation of multiple phases.

Crystallization processes have been studied for a long time, first as "elemental operations" in alchemy and since the end of the $18^{th}$ century as a systematic science. Reanalyzing the literature, it turns out that the science of crystallization is often a "rediscovery", because many important original observations were forgotten and hidden in the past, as they simply could not be completely explained [Cölfen & Antonietti, 2008].

Crystallization is one of the most thoroughly studied processes in academia and has a number of concrete industrial applications, which are divided in two major groups: crystal production (e.g. powder salt for food industry; silicon crystal wafer production; production of sucrose from sugar beet) and elemental purification (e.g. separation of a product from a liquid feed stream; obtainment and improvement of pure substances; purity verification) [Tavare, 1995]. The manufacturing market is growing very fast.

For example, the annual salt production has increased over the past century from 10 million tons to over 200 million tons today and nearly 100 nations have salt producing facilities ranging from basic solar evaporation to advanced, multi-stage evaporation in salt refineries [Hanneman, 2013]. The total polysilicon production in 2010 was 209.000 tons and by the end of 2012 this number has reached 385.000 tons [Huang, 2011, 2012]. The standard sugar beet has a sucrose content of 16%, which yields 130 kg of sugar per 1 ton of sugar beet processed at a sugar plant. It accounts for 20% of the world's sugar production [Punda & Prikhodko, 2009].

One expects, that a process of such scientific and technological importance, which has been studied for centuries, is well understood down to the finest details, but this is not fully true. Although the later stages of a crystallization process are fairly well understood, a large knowledge gap exists regarding the early stages, i.e. nucleation and early growth, still leaving behind unsolved questions. It is known that the classical model does not agree well with many experiments, and there are modern theories that can better explain phase transition processes in terms of spinodal decomposition or prenucleation clusters. A brief description of the classical nucleation theory (CNT) and of the new radical concepts which emerged over the last decade is given below.

### 1.1.1 Nucleation

#### *Classical nucleation theory (CNT)*

The theory of classical crystallization was established by Becker and Döring in the 1930s [Becker & Döring, 1935] on the basis of the quantitative treatment by Volmer and Weber [Volmer & Weber, 1925]. It considers the different stages of precipitation and describes the crystallization process as a layer-wise deposition of atom/ion/molecules on the surfaces of a crystal nucleus, increasing it within the constraints dictated by the crystal unit cell. According to the classical theory, this process consists of two main successive stages: nucleation and crystal growth. The interaction between these two steps determines the crystal characteristics, i.e. atomic structure, size distribution and morphology of the crystals.

In this work we will focus on the crystallization from a solution, which starts from dissolved molecules, or in case of salts, from dissolved ions. The solution must be supersaturated in order to observe nucleation and, later, crystal growth. Several expressions are used for defining supersaturation. The most common one defines supersaturation as a dimensionless ratio of the actual concentration of the species in solution before the crystallization event $C_i$, divided by its saturated or equilibrium concentration $C_s$ under a given set of conditions (pressure, temperature, border conditions…):

$$\beta = \frac{C_i}{C_s} \tag{1.1}$$

If $\beta > 1$, crystals grow; if $\beta < 1$, crystals dissolve; and if $\beta = 1$, crystals and solution are in equilibrium [Boistelle & Astier, 1988].

Other authors prefer to express supersaturation as:

$$\sigma = \ln(\beta) \tag{1.2}$$

This new definition was introduced for a sake of convenience. In this case the condition of equilibrium corresponds to $\sigma = \ln 1 = 0$.

The supersaturation of the solution is therefore the thermodynamic driving force for crystallization and is directly connected with the difference between the chemical potential of the solute molecules in the supersaturated ($\mu$) and saturated ($\mu_s$) states respectively (i.e. the free energy that can be absorbed or released during a chemical reaction). For one molecule the expression of this difference is:

$$\Delta\mu = \mu - \mu_s = kT\ln(\beta) \tag{1.3}$$

where $k$ is the Boltzmann constant and $T$ is the temperature [Boistelle & Astier, 1988].

According to CNT (Fig. 1.1), the primary step in all natural and artificial crystallization processes is nucleation, i.e. the stage when the solute molecules dispersed in the solvent start to gather into aggregates. These aggregates constitute the first nuclei of the system, but they are not stable and may redissolve. Only after reaching a critical size ($r^*$) the aggregates become stable.

$$r^* = \frac{2\Omega\gamma}{kT\ln(\beta)} \tag{1.4}$$

The free energy needed to form this critical radius, also defined as nucleation barrier, is described by

$$\Delta G = \frac{16\pi\Omega^2\gamma^3}{3(kT\ln(\beta))^2} \tag{1.5}$$

based on

$$\Delta G = \frac{1}{3}(4\pi r^{*2}\gamma) \tag{1.6}$$

where $\Omega$ is the volume of a molecule inside the crystal and $\gamma$ is the interfacial free energy between nuclei and solution. The nuclei possess a distinct interface with the surrounding solution and the resulting interfacial free energy represents the origin of the nucleation barrier [Boistelle & Astier, 1988].

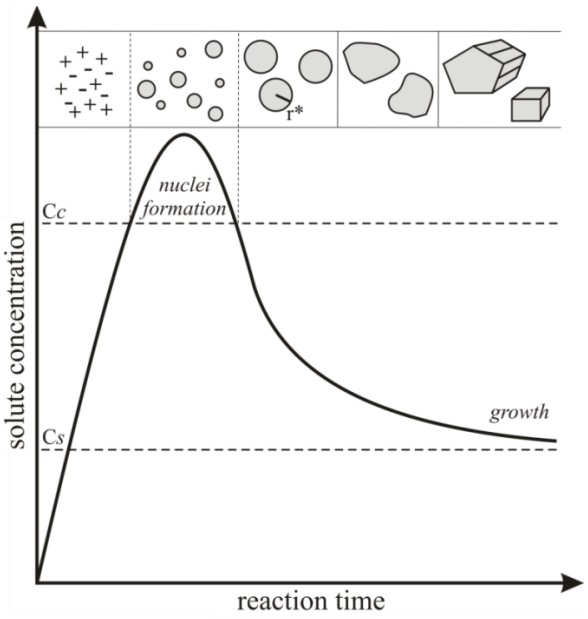


**Figure 1.1 Scheme of classical crystallization process.** When the concentration of a solute $C_i$ increases in time, nucleation usually does not set in immediately when the solubility level ($C_s$) is crossed, but only after a certain supersaturation/concentration threshold $C_c$ is reached. This effect is caused by the nucleation barrier, defined in Equation 1.5. After the initial nucleation, the concentration or supersaturation of the growth species decreases and drops below $C_c$ unless there is a constant supply of new molecules. The postnucleation stage is solely characterized by constant crystal growth which consumes solute molecules until their concentration drops to the level of the equilibrium concentration $C_s$.

The nucleation rate or nucleation frequency ($J$) is the number of crystals that form in a supersaturated solution per unit time and volume [Zettlemoyer, 1969; Abraham, 1974; Toschev, 1973; Kashchiev, 2000]. It can be expressed as [Mangin *et al.*, 2009]:

$$J = N_0 \nu_0 \exp\left(\frac{-f\Omega^2\gamma^3}{(kT)^3 \ln^2(\beta)}\right) \tag{1.7}$$

where *f is* the nuclei form factor. The term $N_0\nu_0$ can be simply described as a pre-exponential factor $K_0$ ($N_0$ – solubility of the material expressed as the number of molecules per unit volume, $\nu_0$ – frequency at which nuclei with critical size become supercritical and develop into crystals) [Boistelle & Astier, 1988].

Equation 1.7 shows that the frequency of nucleation ($J$) depends not only on the supersaturation ($\beta$) but also on the concentration of molecules ($N_0$) and on the interfacial free energy ($\gamma$). All things being equal, supersaturation included, the higher the probability of intermolecular contact, the easier the nucleation. Systems with high solubility meet this condition. For systems with low solubility, the solute molecules are separated by larger distances and by a greater number of solvent molecules. The probability that the molecules will come into contact and form a nucleus is thus lower.

### *Non-classical nucleation theory - Spinodal decomposition (SD)*

Spinodal decomposition (SD) is a pure diffusion phenomenon by which phase separation in a solution of two or more components is delayed until the system enters the unstable region.

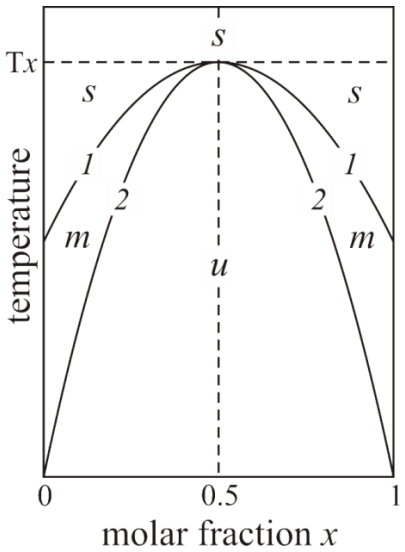


**Figure 1.2 A phase diagram for two partially miscible solutions according to spinodal decomposition theory** (temperature against molar fraction of a component $x$). The diagram is symmetrical around $x$ = 0.5 for the regular solution model. Line (*1*) is the phase boundary. Above the line the two liquids are miscible and the system is stable (*s*), below there is a metastable region (*m*) where the system is stable to small fluctuations but is unstable to large ones. Line (*2*) is the spinodal. Below this line the system is unstable (*u*). Regions (*m*) and (*u*) constitute the miscibility gap where the system turns from a one-phase to a two-phase system. Above temperature ($T_x$) the two liquids are miscible in all proportions.

In a phase diagram (Fig. 1.2) this region is defined by the limit of stability of a solution (line (*2*) in the diagram). When a system has crossed this locus, phase separation occurs spontaneously without the presence of a nucleation step (Fig. 1.3) undergoing SD. Commonly this process results in a high interconnectivity of the new-formed phases [Favvas & Mitropoulos, 2008], but it is also possible that the first-formed species start to nucleate inside ion-rich droplets.

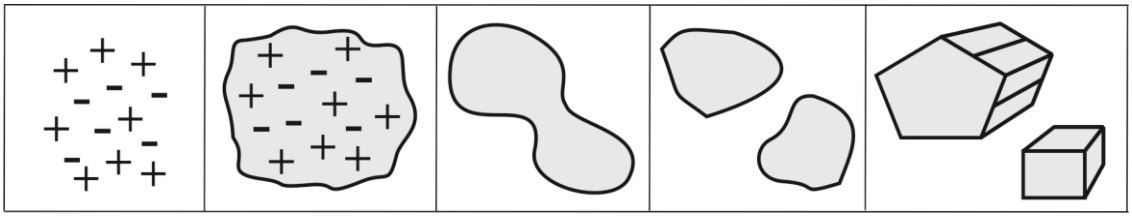

**Figure 1.3 Scheme of non-classical nucleation *via* spinodal decomposition.** Phase separation occurs by ion diffusion from ion-poor to ion-rich regions presumably forming a liquid-amophous precursor, followed by crystallization.

The kinetics of SD may be described by the Cahn-Hilliard model [Chan & Hilliard, 1958, 1959], that adds a correction to the homogeneous free energy function to account for spatial inhomogeneity. Similar models were used by Van der Waals to model liquid-vapor interfaces, and by Landau to study superconductors. SD can be also derived from the CNT assuming that the nucleation barrier becomes 0 ($\Delta G \rightarrow 0$) at very high supersaturation ($\beta \rightarrow \infty$).

Although crystallization *via* SD is commonly observed in polymer mixtures [Smolders *et al.*, 1971; Kuwahara *et al.*, 1992] and solid solutions [Langer, 1971; Hono & Hirano, 1987; Miller *et al.*, 1995] there are only few published cases of mineral formation from solution *via* SD [Faatz *et al.*, 2004].

### *Non-classical nucleation theory – Prenucleation clusters (PNC)*

The second main non-classical pathway discussed in literature involves stable clusters prior to nucleation. These clusters are thermodynamically stable and not metastable as classically considered. They are solutes and hence do not have an interface to the surrounding solution. They are considered to be the stable species of the one-phase-system. Gebauer *et al.* [Gebauer *et al.*, 2008], in their experiments based on the measurement of ions concentrations at constant pH values and by measurements of sedimentation coefficients with analytical ultracentrifugation (AUC), provided convincing evidence that dissolved calcium carbonate contains stable prenucleation ion clusters (PNC), which even form in undersaturated solution. One year later, Pouget *et al.* [Pouget *et al.*, 2009], by using high-resolution cryo-TEM, could visualize PNC and support their role in the nucleation process. Beyond that, their experiments showed that the PNC persisted after nucleation. This is in contrast to the previous observations [Gebauer *et al.*, 2008], that showed the disappearing of cluster species after nucleation.

It has also been shown [Gebauer & Coelfen, 2011] that non-classical nucleation *via* stable PNC is a highly valuable concept for specified complex crystal structures [Navrotsky, 2004; Horn & Rieger, 2001; Perry, 2003; Furrer *et al.*, 2002; Casey & Swaddle, 2003; Larson & Garside, 1986;

Larson, 1991], which may hardly be explained by classical nucleation theory. Possibly, the PNC concept is of broader importance and shall apply to a number of other materials, but the generality of this concept still needs to be tested.

### 1.1.2 Crystal growth

Once nuclei are formed, they first develop into small crystals and later increase their own dimension. Classically, there are two major mechanisms of crystal growth that were distinguished by Burton and Cabrera in 1949 [Burton & Cabrera, 1949*a*, 1949*b*]. In these models an ideal crystalline surface grows by the spreading of single layers – uniform normal growth (Fig. 1.4a) – or by the lateral advance of the growth steps bounding the layers – non-uniform lateral growth (Fig. 1.4b).

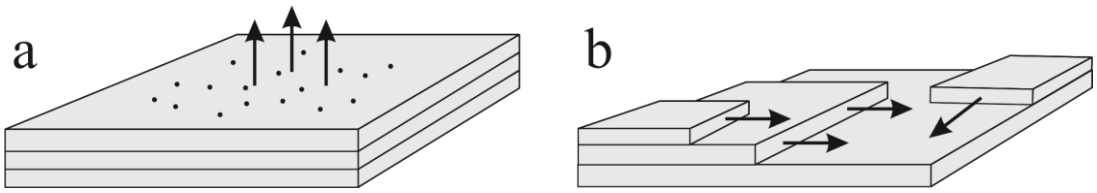


**Figure 1.4 Models of classical crystal growth mechanism.** (**a**) Uniform normal growth. (**b**) Non-uniform lateral growth. The arrows show direction of crystal growth.

It has been shown that the energy necessary for crystal growth is only reached at relatively high supersaturation [Cubillas & Anderson, 2010], while crystals can in fact grow at much lower supersaturation [Volmer & Schultz, 1931]. A possible solution for this dilemma was proposed by Frank [Frank, 1949], who postulated that crystal surfaces are intercepted by dislocations. In the initial stage the dislocation creates a step in the surface (Fig. 1.5). Growth units attach to the step making it advance and thus generating a second step. The so called spiral growth requires less energy than a layer mechanism, and can therefore proceed at lower supersaturation.

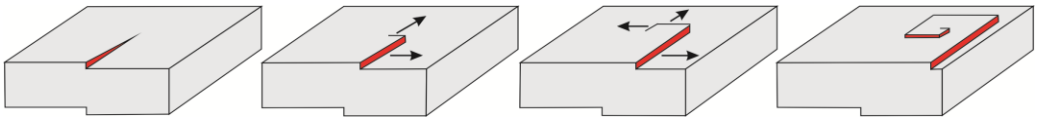

**Figure 1.5 Development of spiral crystal growth.** The arrows indicate direction of crystal growth.

Each crystal is limited by its faces. The growth mechanism and growth rate of each face depends on different external (pressure, temperature, impurities) and internal (structure, bonds, defects) factors. A set of equivalent faces resulting from the crystal symmetry is called a form. All forms present on a crystal define the morphology of the crystal [Mangin *et al.*, 2009]. In 1980, Hartman

and Bennema demonstrated the possibility to determinate the relative growth rates of the faces [Hartman & Bennema, 1980]. Almost 30 years later, it was shown experimentally that the shape (habit) of the crystal only includes the faces with the slowest growth rates [Astier & Veesler, 2008].

Crystal growth can either be thermodynamically or kinetically controlled. If the crystal growth is strictly thermodynamically controlled, the equilibrium morphology, associated with the minimum total surface energy, is obtained. Kinetically controlled crystal growth often leads to different morphologies and/or phases. At high supersaturation, kinetically controlled growth dominates, whereas large single crystals in their equilibrium morphology can only be obtained at very low supersaturation conditions, slightly above the solubility limit (low growth kinetics).

A strong influence on the growth kinetics comes from the growth medium that can affect the process in different ways. For example, the medium can speed or slow down the growth rate for certain faces or affect the hydrodynamics [Rosenberger, 1979]. Finally, the presence of impurities or additives also affects the growth rates of the different faces of the crystal [Ohara & Reid, 1973; Boistelle & Astier, 1988].

### 1.1.3 Metastable phases

The term phase is used to designate a certain solid type. Phases that have the same chemical composition but different crystal structure are called polymorphs. Very often, nucleation does not directly lead to the formation of the most stable phase but to a phase with a slightly higher free energy. In most systems, especially if they are closed, there is a continuous decrease of the supersaturation during crystallization. As a result, both the nucleation and the crystal growth kinetics decrease, and these processes favor phase transitions. Metastable phases may stay in their metastable state for a few seconds or several centuries, but the transformation of a metastable phase into a stable one always points to the minimum free energy of the system [Mangin *et al.*, 2009]. Therefore, in an isolated system, a phase transformation can only occur from a less stable to a more stable solid phase. In solution, when several phases coexist, the stable phase is always the least soluble one (characterized by the highest $\Delta\mu$, see Equation 1.3) [Boistelle & Astier, 1988]. However, according to the Ostwald rule of stages [Ostwald, 1897], only rarely the most stable phase nucleates first, so that an unstable system does not necessarily transform directly into the most stable state, but rather into the metastable, transient state, which is closest in energy. This can lead to the occurrence of metastable nanocrystals, and possibly to rare or unknown polymorphs [Mangin *et al.*, 2009].

In order to study these intermediates, the reaction needs to be stopped to trap metastable intermediates. This kind of samples has been defined as "snapshots" [Beck *et al.*, 2007; Sander & Golas, 2011]. This term comes from photography and it is used here to indicate any frozen stage of a reaction that could be stopped during its regular evolutionary process. Snapshots give us the opportunity to investigate the crystallization process step by step and possibly to reconstruct it completely.

## 1.2 Structural characterization of crystallization stages

Most of the newly discovered mineral phases, as well as many new synthesized industrial materials, appear only in form of nanocrystals. The development of techniques which allow investigating the structure of nanocrystalline materials is therefore one of the most important frontiers of crystallography.

### 1.2.1 X-ray crystallography

In 1912 Laue and co-workers Friedrich and Knipping [Friedrich *et al.*, 1912] showed that crystalline solids diffract when they are passed by X-rays, in this way opening the way to structure characterization of crystalline materials. In a century, structural crystallography allowed the description of the atomic structure of millions of phases, both organic and inorganic, with a resolution unachievable with conventional optical instruments. In a diffraction pattern, reflection arrangement makes it possible to identify the fundamental unit cell parameters of the crystal, while the intensity of reflections provides information about the position that the atoms occupy within this cell. The knowledge of the structures at the atomic scale is of fundamental importance for understanding the properties of the materials and the processes that have led to their formation, and constitutes the starting point for the engineering of new compounds with advanced technical properties.

Over time, many types of diffractometers have been developed and several technical improvements (X-ray sources, goniometers, detectors and automation) allowed accessing crystals with a size of less than one cubic millimeter using standard laboratory sources and few micrometers using synchrotron radiation [Holton & Frankel (2010)].

For crystals of smaller size, X-rays can be used for the investigation of a polycrystalline powder. The first X-ray powder diffraction data (XRPD) were collected by Debye and Scherrer [Debye, 1915; Debye & Scherrer, 1916] and in parallel by Hull [Hull, 1917, 1919, 1921] in the early 1990s. Structure solution using XRPD developed rapidly only in the last forty years and was significantly accelerated by the development of Rietveld's method [Rietveld, 1969]. Nowadays, XRPD is the most widespread technique providing relatively fast and well consolidated routes for structure analysis of nanocrystalline materials. Nevertheless, XRPD suffers from intrinsic 1D reduction of structural information that greatly limits its applicability due to peak broadening and overlapping, which complicates the accurate determination of the position and intensity of diffraction peaks [Dorset, 2003]. Peak broadening is usually caused by very small crystallites, namely less than 50 nm. Overlapping of peaks is problematic mainly for intensity integration, but in case of polyphasic mixtures or significant amount of impurities, also cell parameter determination and reflection indexing can become problematic. Furthermore, a powder diffractogram is strongly influenced by experimental factors, which are not always predictable or properly modelled, such as preferential orientation of the grains or presence of individual fragments with anomalous dimensions [David *et al.*, 2002]. Finally, this technique is however hardly applicable to mixtures where the phase of interest is not dominant [Weirich, 2003].

### 1.2.2 Electron scattering and transmission electron microscope

In 1924, Louis de Broglie postulated that to any particle with a certain mass and velocity, can be assigned a wavelength.

$$\lambda = \frac{h}{p} = \frac{h}{mV} \cdot \sqrt{1 - \frac{V^2}{c^2}} \tag{1.8}$$

where $\lambda$ is the wavelength, $h$ is the Planck constant, $p$ is the momentum, $m$ is the rest mass, $V$ is the velocity and $c$ is the speed of light in a vacuum.

Inspired by this, in 1927 Davisson and Germer in the low energy range (54 eV) [Davisson & Germer, 1927*a*, 1927*b*] and Thomson and Reid in the high energy range (20.000 – 60.000 eV) [Thomson & Reid, 1927] showed the first diffraction experiments originated by the interaction of electrons with matter. Unlike X-rays, electrons are easily deflected by magnetic fields and it is therefore possible to: (i) focus the beam in probes of few nanometers and (ii) recombine the scattered information in real space microscographs (i.e to build microscopes operating with electromagnetic lenses). In the following years, a series of important discoveries took place: Ruska and Knoll built the first transmission electron microscope (TEM) prototype based on electron lenses [Ruska & Knoll, 1931; Knoll & Ruska, 1932] and Ruska succeeded in beating the resolution of an optical microscope [Ruska, 1935]. A few years later TEMs became available commercially from several companies. Today, they constitute one of the most efficient and versatile tools for the characterization of materials. Historically, TEMs were developed because of the limited image resolution of light microscopes, which is imposed by the wavelength of visible light [Williams & Carter, 1996*a*]. Only after electron microscopes had been developed, it became evident that there are many other equally sound reasons for using electrons. TEM can in fact be used for performing chemical spectroscopic analysis [Williams & Carter, 1996*c*] and electron diffraction [Williams & Carter, 1996*b*]. The possibility of combining electron diffraction with TEM imaging was realized by Kossel and Möllenstedt in 1939 [Kossel & Möllenstedt, 1939].

TEM uses a beam of electrons accelerated by a voltage of a few hundreds of kV as light source. Under these conditions, electrons can be considered a radiation with a wavelength smaller than visible light and X-rays, and therefore, they theoretically enable better spatial resolution. Furthermore, the interaction of the electrons with matter is about $10^6$ times higher compared to X-rays, and it is therefore possible to obtain well-resolved diffraction pattern also from extremely reduced volumes of material [Cowley *et al.*, 2001]. At the same time the ratio between scattering coefficients of heavy and light atoms is relatively small (Fig. 1.6), thus ensuring a better detection of light atoms [Vainshtein & Ibers, 1958; Doyle & Turner, 1968; Dorset, 1996]. The technological advancement has allowed constructing TEMs with resolutions of less than 1 Å, which can be used now to investigate single nanocrystals, nanocomplexes and even individual defects.

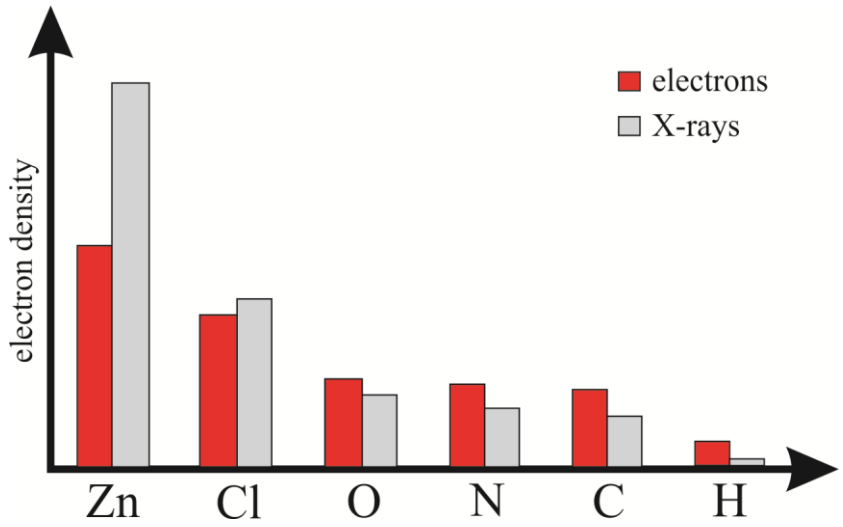


**Figure 1.6 Comparison between electron density amplitude of heavy and light atoms for X-rays and electrons.**

***HRTEM***

High resolution transmission electron microscopy (HRTEM), the most established techniques for nanostructure imaging, provides direct space structural information down to 0.8-0.5 Å resolution [Kisielowski *et al.*, 2008*a*, 2008*b*]. Unfortunately, the electromagnetic lenses, in particular the objective of the microscope, are characterized by aberrations that significantly restrict the resolution and compromise the immediate interpretation of HRTEM images. Only the latest generation of microscopes, equipped with energy filters and electromagnetic multi-pole correctors, can partially overcome these aberrations reaching down to a resolution of 0.05 nm [Rose, 1990; Haider *et al.*, 1998; Shlossmacher *et al.*, 2005]. Additionally, HRTEM imaging requires a relatively high intensity illumination and a large electron dose on the sample. Under these conditions, nearly all organic and most of inorganic materials suffer a fast deterioration due to beam damage. The necessity to orient the particle in order to record meaningful HRTEM images further increases the exposure time. This may lead to a modification of the crystalline structure or to complete amorphization or sublimation of the sample [Spence, 2003; Reimer & Kohl, 2008; Kolb *et al.*, 2010].

***Cryo-TEM***

Since beam damage is often the most limiting factor for HRTEM investigation, several methods for beam damage reduction have been developed. Cooling at liquid $N_2$ or He temperature is a way of stabilizing a sample inside a TEM or of increasing its resistance to electron beam damage. Cryo-conditions are essential for biological investigations, but they are also important for working with any organic or metastable material [Kolb *et al.*, 2010; Danino, 2012], to slow down the beam illumination on the sample [Williams & Fisher, 1970], or to improve the efficiency of the signal detection [Crewe *et al.*, 1975]. Cryo-fixation or vitrification is the easiest and most consolidated methods of cryo-TEM sample preparation. Since 1976, when Taylor and Glaeser [Taylor & Glaeser, 1976] proved that water does not significantly evaporate when the sample is cooled by refrigerating liquid such as $N_2$, people started to develop methods for rapidly freezing

the sample. The biggest progress was done by Dubochet in 1980s [Dubochet *et al.*, 1988], who first built a machine for cryo-sample preparation. It was a very simple devise, consisting of tweezers and a swimming pool for cryogen. Nowadays, commercial machines for cryo-sample preparation still work based on the same principle, completed by few improvements (using paper filter and liquid ethane or propane as cryogen) proposed by Adrian in 1984 [Adrian *et al.*, 1984].

### 1.2.3 Electron diffraction

In contrast to HRTEM, electron diffraction can deliver structural information at a comparable resolution with good signal to noise ratio. Electron diffraction is usually performed with a parallel illumination on the specimen. Illumination of the sample with a higher beam convergence leads to diffraction discs (Fig. 1.7a) rather than focused spot patterns (convergent beam electron diffraction – CBED). This technique provides accurate cell parameters and even full crystal symmetry information, but has almost no application for metastable materials, which are often beam sensitive, since high convergence of the beam causes high electron dose on the sample. Moreover, long crystallographic axes cause overlap of the diffraction disks and limit the useful information in CBED patterns.

On the contrary, spot-like electron diffraction patterns can be created by parallel illumination of the sample through two different approaches: (i) by the insertion of a selected area aperture (selected area electron diffraction – SAED) in the objective lens back focal plane (Fig. 1.7b), or (ii) by the use of a small condenser aperture (10 μm) to generate a semi parallel beam (Fig. 1.7c) with a diameter down to 10 nm on the sample (nano electron diffraction – NED). In SAED mode, a large area of the sample is unavoidably illuminated, while the diffraction information is only collected from the part inside the selected area aperture. In NED mode, the information is collected only from the area directly illuminated by the beam [Ohnishi & Hiraga, 1996]. Therefore, SAED is less efficient for beam sensitive materials than NED, as beam damage can be still a major issue in electron diffraction for materials like organics or water-containing media.

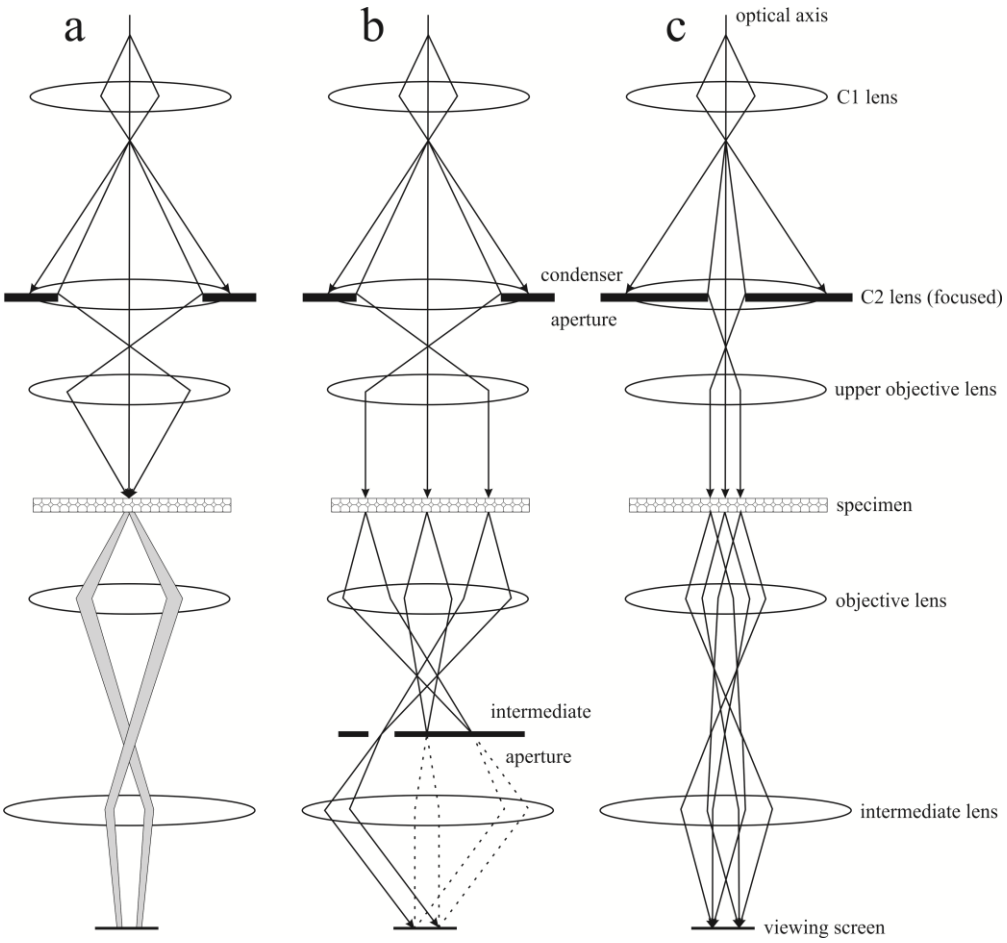


**Figure 1.7 Electron beam geometry**. (**a**) Convergent beam electron diffraction. (**b**) Selected area electron diffraction. (**c**) Nano electron diffraction.

The strong interaction of electrons with matter and the simultaneous diffraction of many reflections, as well as the lack of mosaicity in a single nanocrystal, generate dynamic diffusion effects that are not negligible. The electron beam can in fact be diffracted several times while crossing the crystal and each diffracted beam can in turn give rise to additional diffractions. The dynamic effects lead to a disturbance in the intensities of reflections that can hamper solution and refinement of the structure. Unfortunately, the mathematical models to describe this phenomenon are extremely complex [Howie & Whelan, 1961; Cowley, 1995; Fultz & Howe, 2002; McLaren, 1991; Peng *et al.*, 2004] and insufficient in the presence of lateral thickness variations or defects [Dorset, 1995*a*]. Furthermore, their strict application requires *a priori* knowledge of at least part of the examined structure [Dorset, 1996].

Another classical limitation of electron diffraction is the incompleteness of intensity data sets. In fact, the conventional way of electron diffraction data collection is based on acquisition of oriented zones. However, dynamic effects are maximized in oriented zones, and only a limited number of reflections are accessible (namely only reflections that belong to low index zones). All

these problems derive basically from the instrumentation and the methods used for electron diffraction data collection.

The application of electron diffraction data for structure solution dates back to 1936 [Rigamonti, 1936], but for a long time, European and American scientists considered electron diffraction to be of little use due to the presence of dynamic effects [Cowley, 1956; Lipson & Cochran, 1966]. Thus, attempts of structure solution, performed often through a combination of diffraction and imaging data, focused on weak scatterers such as organic [Dorset & Hauptman, 1976; Dorset, 1995*a*] or biological samples [Dorset, 1995*b*; Kühlbrandt *et al.*, 1994; Unwin & Henderson, 1975] which were expected to deliver nearly kinematic diffraction data.

Nevertheless, excellent results were achieved solving structures from data sets collected by an electron diffraction camera developed by Pinsker and Vainshtein in Moscow during the 1950s [Pinsker, 1953; Vainshtein, 1956, 1964)]. The data collection technique, which was generally used by these authors and named oblique textured electron diffraction (OTED), is based on the illumination of a large amount of slightly disoriented crystals in order to mimic intrinsic mosaicity of the sample (Fig. 1.8) [Zvyagin, 1967]. Sample preparation for OTED measurement is highly problematic because the obtained diffraction pattern derives from the reflections of many crystals which need to be oriented approximately in the same way. Nevertheless, in OTED, dynamic effects, which are maximized in oriented zones, are significantly reduced and a number of organic and inorganic phases were solved, up to the localization of hydrogen atoms in the structure [Zhukhlistov *et al.*, 1997; Zhukhlistov & Zvyagin, 1998]. The main limit of OTED is that it is impossible to analyze a single nanocrystal with this apparatus, as it is normally done with a TEM. In sum, on one hand this technique can be extremely advantageous for the detection of light atoms; on the other hand it does not guarantee the solution of individual nanostructures within polyphasic aggregates or mixtures [Dorset, 1996].

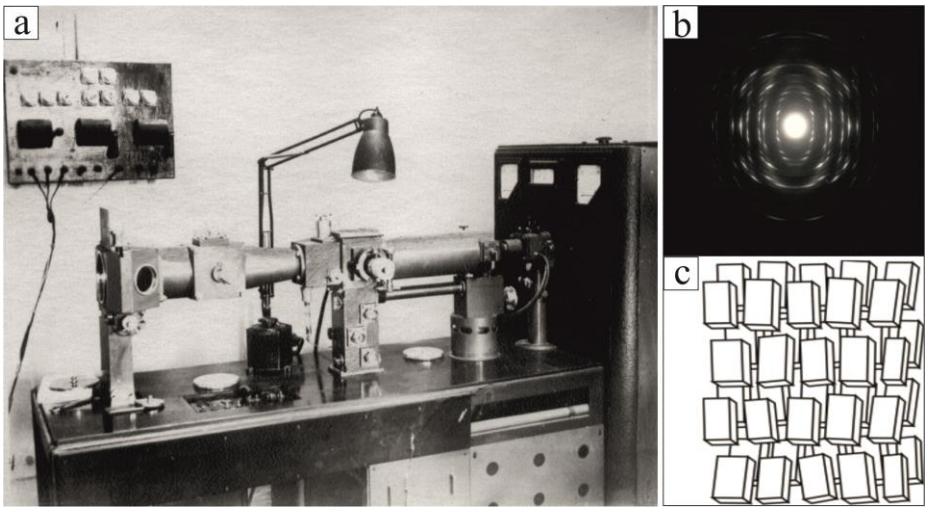


**Figure 1.8 Oblique textured electron diffraction.** (**a**) The electron diffraction camera developed by Pinsker and Vainshtein. (**b**) Exemplary diffraction pattern obtained with OTED. (**c**) Scheme of a sample needed for OTED technique.

From the second half of the 1970s, a new interest for electron diffraction and crystallography has arisen. It was demonstrated that structure characterization can be successfully performed using electron diffraction data collected with a TEM, and deriving it from individual nanocrystals [Dorset & Hauptman, 1976]. In the following 30 years, both organic and inorganic structures have been extensively investigated [Dorset, 1995*a*]. The leading idea of this work is that by collecting data from very thin crystals (e.g. less than 50 Å), the dynamic effects are reduced so much that a kinematic approximation ($I \approx F^2$) is valid for structure solution [Nicolopoulos *et al.*, 1995; Voigt-Martin *et al.*, 1995; Weirich *et al.*, 1996; Wagner *et al.*, 1999; Dorset *et al.*, 2005; Dorset, 2007].

While OTED was dependent on special sample properties, the electron beam precession method invented by Vincent and Midgley [Vincent & Midgley, 1994] in 1994 was able to reduce dynamical effects by changing the data collection process. Here the electron beam undergoes a precession movement around an axis comprising a conical path, so that the sample is never fully oriented along a main axis (Fig. 1.9). A second very important effect of the beam precession is the integration of reflections by the precessing Ewald sphere that eliminates, or at least reduces drastically, the uncertainty in intensity determination caused by the excitation error [Williams & Carter, 1996*b*]. An increasing number of structure solutions achieved by using precession electron diffraction (PED) data are reported in literature, even for relatively thick samples [Weirich *et al.*, 2006; Dorset *et al.*, 2007; Gemmi *et al.*, 2010].

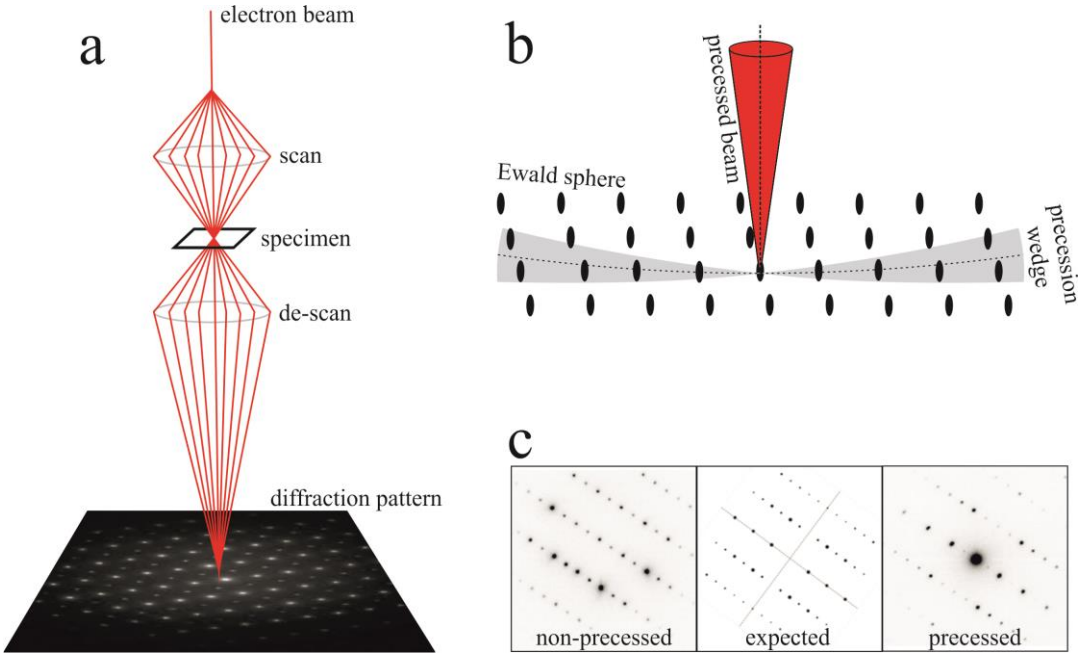


**Figure 1.9 Precession electron diffraction.** (**a**) Beam precession geometry. (**b**) Sketch of Ewald sphere movement during precession. (**c**) Experimental in-zone diffraction patterns collected without precession and with precession, compared to expected one from theoretical simulation.

Electron diffraction has been frequently used in combination with X-ray powder data. A recent example of structure solution of nanocrystalline material combining electron diffraction with *a priori* obtained crystallochemical information, HRTEM and XRPD data is reported by Baerlocher *et al.* [Baerlocher *et al.*, 2007]. This method has been successfully applied for some complicate zeolite structures, but until now it cannot be considered a routine path for structure analysis, as any working case needs a specific, different approach.

### 1.2.4 Automated electron diffraction tomography (ADT)

As outlined in the previous chapter, there is still a need for routine methods, which allow the acquisition of more complete and close-to-kinematic electron diffraction data. This demand recently led to the development of the automated electron diffraction tomography (ADT) method [Kolb *et al.*, 2007, 2008]. The ADT distinguishes itself radically from the traditional way of electron diffraction data acquisition based on oriented zones. In conventional electron crystallography (Fig. 1.10), 3D electron diffraction data are collected by a tilt of a pre-oriented nanocrystal around a crystallographically pronounced axis. Such planar reciprocal space cuts only provide the collection of prominent zones, ignoring a number of high indexed reflections. In the ADT method (Fig. 1.11), the tilt axis is an arbitrary axis rather than a special crystallographic direction (principally avoiding oriented zones) and the reciprocal space is sliced sequentially in fixed tilt steps. This allows the collection of a larger amount of reflections, shortens the total exposure time and, most importantly, provides reflections from non-oriented cuts through the reciprocal space (off-zone data), reducing dynamical effects significantly. It is especially important to avoid the tilt around a specific crystallographic axis since in this case oriented zones are collected accidentally and dynamic effects are enhanced. The idea is closely related to routines used nowadays in single crystal X-ray diffraction with two-dimensional CCD detectors. Nevertheless, a direct application of the X-ray concepts to electron diffraction is not possible due to significant differences in technical instrumentation and the nanometer size of the sample.

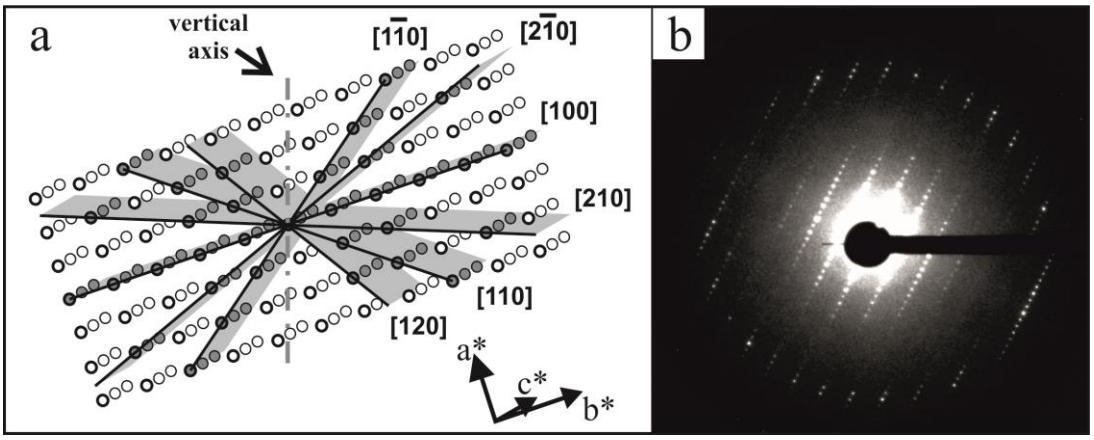


**Figure 1.10 Traditional electron diffraction.** (**a**) Sketch showing data acquisition based on the manual orientation of low-index oriented zones (grey planes) by a tilt around **c***. Reflections of the reciprocal lattice are sketched as spheres (filled spheres: effectively sampled reflections; empty spheres: missed reflections). The three main crystallographic axes are shown at the bottom. The Ewald sphere is approximated as a plane. (**b**) An exemplary in-zone diffraction pattern.

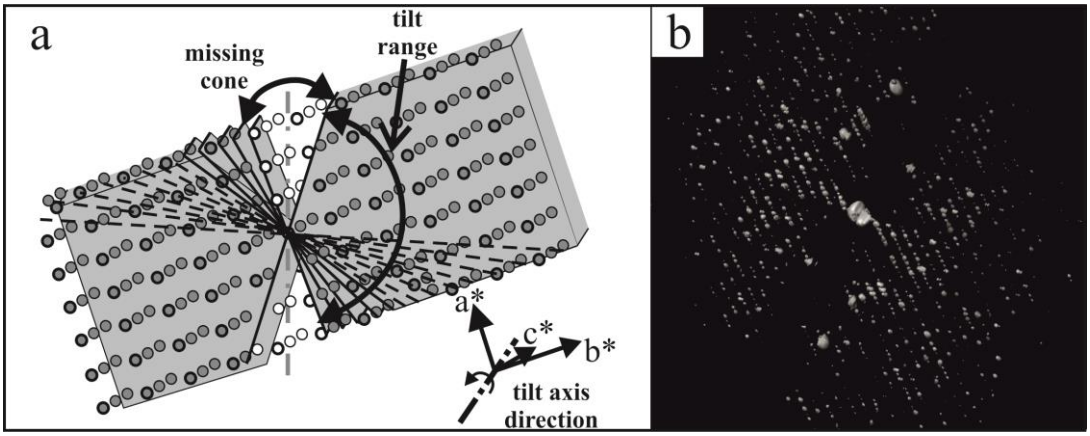


**Figure 1.11 Automated electron diffraction tomography.** (**a**) Sketch showing ADT sequential acquisition of non-oriented patterns in fixed tilt steps of 1° around an arbitrary axis not corresponding with any recognizable crystallographic orientation. Reflections of the reciprocal lattice are sketched as spheres (filled spheres: effectively sampled reflections; empty spheres: missed reflections). The three main crystallographic axes are shown at the bottom. The Ewald sphere is approximated as a plane. (**b**) An exemplary 3D diffraction reconstruction based on ADT method.

In order to reduce the electron dose on the sample and perform long acquisitions even on beam sensitive samples, a beam size down to 30 nm on the sample with almost parallel illumination is used. Diffraction patterns are acquired in NED mode, using a small condenser aperture (C2) of 10 μm.

Even crystals perfectly adjusted in eucentric height move slightly through crystal tilting. Therefore, the crystal position needs to be tracked manually or automatically by correlation with a reference image taken in TEM or STEM mode. With these settings, the illumination, and thus the electron dose on the sample, can be significantly reduced down to an electron dose rate of 0.15-0.20 $e^{-1}$ $Å^{-2}$ $s^{-1}$ [Kolb *et al.*, 2007]. Dedicated software allows automation of data acquisition [Kolb *et al.*, 2008]. Automation of the procedure is not only convenient for increasing the feasibility of the experiment, but more importantly for reducing the overall exposure time and consequently reducing beam damage; this further increases the chance to collect complete 3D data acquisitions from beam sensitive samples [Kolb *et al.*, 2010; Gorelik *et al.*, 2012*a*]. The electron dose received by a sample during STEM image recording is several orders of magnitude lower than that used for electron diffraction acquisition [Kolb *et al.*, 2007]. Therefore, by using the automated acquisition module, combining STEM and NED mode and assuming an exposure time of 1 s per diffraction pattern, it becomes possible to collect a full tilt series with a total exposure time of 2 minutes. Possibly beam damage can be further reduced by using cooling conditions [Zhuang *et al.*, 2011; Gorelik *et al.*, 2012*b*] or by slightly moving the beam around the crystal during the acquisition.

The complete tilt series acquisition including tilting, crystal tracking, diffraction pattern recording and data saving takes about 1-2 h depending on the specific angular range. After the acquisition, a stack of 2D non-zonal diffraction patterns is stored. The tilt series is analyzed by the in house developed software package *ADT3D* coupled with additional *MatLab* scripts [Kolb *et al.*, 2008, 2011; Mugnaioli *et al.*, 2009]. The 3D reciprocal space can be reconstructed and used for direct visualization of disorder, twinning and polycrystallinity. Cell vectors (cell parameters + orientation matrix) are defined by automated routines based on clustering in difference vector space [Schlitt *et al.*, 2012]. The approach allows the determination of unit cell parameters with an accuracy of about 2-3% and can be successful even for sparse data sets or small tilt ranges.

Finally, reflections are indexed and intensities are integrated. Because all reflections inside the available tilt range are sampled, ADT intensity data sets have a significantly higher coverage of reciprocal space than those obtained by conventional electron diffraction zonal acquisition. Depending on the crystal family, completeness ranges from 60% for triclinic, to 70-90% for monoclinic, 90% for orthorhombic and 100% for cubic lattices. Reflection intensities integrated by the ADT approach are expected to be more kinematic than those measured in oriented patterns, as they are collected off-zone and dynamic effects are therefore drastically reduced. Nevertheless, a significant deviation from expected values is still present, mainly due to the excitation error, i.e. the distance at which the Ewald sphere cuts the reflection from the center [Williams & Carter, 1996*b*]. In order to perform a complete integration of reflection intensities, PED can be coupled with ADT [Mugnaioli *et al.*, 2009]. The resulting data sets proved to be of high quality and in the last years a number of complicate structures have been solved *ab-initio* by direct methods with a fully kinematic approach [Mugnaioli *et al.*, 2009, 2012*a*, 2012*b*, 2012*c*; Rozhdestvenskaya *et al.*, 2010, 2011; Kolb *et al.*, 2010, 2011; Birkel *et al.*, 2010; Andrusenko *et al.*, 2011; Denysenko *et al.*, 2011; Gemmi *et al.*, 2011; Gorelik *et al.*, 2011; Jiang *et al.*, 2011; Palatinus *et al.*, 2011; Sedlmaier *et al.*, 2011; Bellussi *et al.*, 2012; Feyand *et al.*, 2012; Gemmi *et al.*, 2012; Gorelik *et al.*, 2012*a*; Sarakinou *et al.*, 2012; Boullay *et al.*, 2013; Gemmi *et al.*, 2013; Mugnaioli & Kolb, 2013; Rius *et al.*, 2013; Zubko *et al.*, 2013].

## 1.3 Materials selected for investigation

### 1.3.1 Laser host materials

During the last years the interest in tunable and very-short-pulse solid-state lasers increased due to their promising application in new technologies, like medical devices, optical communication and navigation systems [Kaminskii, 1996]. This interest stimulated the study of single crystal materials with a broad band emission in the near-infrared region. The study involved several tungstates [Nikolov *et al.*, 2003*a*, 2003*b*, 2003*c*, 2003*d*, 2004; Hermanowicz, 2006; Ivanova *et al.*, 2007; Cavalli *et al.*, 2008; Tzvetkov *et al.*, 2009; Koseva *et al.*, 2011], molybdates [Hermanowicz *et al.*, 2001*a*, 2001*b*; Wang *et al.*, 2007, 2008], germanates [Bykov *et al.*, 2005], gallate spinels [Kim *et al.*, 2004], silicates [Avanesov *et al.*, 1997; Chen & Boulon, 2003; Padlyak *et al.*, 2003; Gluchowski *et al.*, 2009], aluminates [Gurov *et al.*, 2008], borates [de

Backer *et al.*, 2003; Brik *et al.*, 2007], fluorides [Torchia *et al.*, 2002; Tanner, 2004; da Silva *et al.*, 2006] and oxides [Kuck *et al.*, 2000; Patra *et al.*, 2005]. Moreover, it has been proved that $Cr^{3+}$ doped $NaAl(WO_4)_2$ [Nikolov *et al.*, 2004] and $KAl(MoO_4)_2$ [Wang *et al.*, 2008]crystals are suitable laser hosts having high absorption, efficient pumping and broad laser emission.

Looking for other possible candidates as laser host materials, we focused on the study of the ternary oxide system $M_2O$-$Al_2O_3$-$WO_3$ ($M$ = alkaline metals). New compounds in these systems are promising laser materials due to their high and continuous transparency in the wide range of near-infrared region [Nikolov *et al.*, 2003*b*, 2003*c*]. A number of these materials is characterized by low thermal expansion values, which makes them especially promising for special ceramics [Krell *et al.*, 2009; Lupei, 2009].

The study performed up to now has not been systematic and exhaustive, so it was not possible to determine the optimum composition of the material with respect to a given application or to a given synthetic condition. Understanding and optimizing the properties of such phases and their production requires the knowledge of the atomic structure. Yet, for most tungstates the final synthetic products are nanocrystalline polyphasic mixtures, as several secondary phases crystallize in parallel [Koseva *et al.*, 2011].

### 1.3.2 Electrode materials for dye-sensitized solar cells (DSSC)

In 1991 O'Regan and Graetzel published an article on the use of a colloidal $TiO_2$ film as electrode material for a very efficient dye-sensitized solar cell (DSSC) [O'Regan & Graetzel 1991], demonstrating the usefulness of $TiO_2$ nanoparticles in technological applications. Henceforth $TiO_2$ nanoparticles have been synthesized in various sizes and morphologies [Chen & Mao 2007] and have been attracted considerable attention for more than ten years due to their wide range of interesting applications, for example as photocatalyst [Adachi *et al.*, 2000], carrier material for catalytically active nanoparticles [Hsu *et al.*, 2010], potential adsorbents for the removal of heavy metal ions and dyes [Huang *et al.*, 2011], dye-sensitized solar cells [Ngamsinlapasathian *et al.*, 2004], robust gas sensors [Varghese *et al.*, 2003], lithium [Kavan *et al.*, 2004] and hydrogen [Lim *et al.*, 2005] storages or electrochromic devices [Bach *et al.*, 2002].

In order to obtain highly efficient DSSCs two counteracting requirements have to be met. First a large number of dye/semiconductor interfaces is needed to ensure a high photocurrent (i.e. high surface area), and at the same time a high transport rate of electrons towards the front electrode is necessary (i.e. few grain boundaries). By using $TiO_2$ nanorods as an additive to the commonly used nanoparticular $TiO_2$ semiconductor, these demands can be met.

Sodium titanate nanowires and nanotubes represent important intermediate products in the synthesis of $TiO_2$ nanorods. They can be obtained from any $TiO_2$-based precursor by hydrothermal treatment in a highly concentrated NaOH solution and converted to $TiO_2$ *via* an acidic treatment, followed by calcination. Despite the importance of sodium titanate nanostructures as intermediate precursors for long $TiO_2$ nanorods, no big effort has been made to investigate the crystal structure of these nanostructures. It is generally accepted that sodium

titanate nanotubes are the first structures to form and later transform into sodium titanate nanowires.

Numerous publications deal with the synthesis of sodium titanate nanotubes at different conditions [Huang *et al.*, 2009, 2011], but their growth mechanism is still not fully understood. Nanotube structures were proposed as anatase [Kasuga *et al.*, 1998], layered trititanate [Chen *et al.*, 2002], lepidocrocite-like structures [Ma *et al.*, 2003; Yang *et al.*, 2003]. These models were just derived by comparison of the available poor X-ray powder and electron diffraction data with known structures. Nevertheless, often low-quality X-ray powder diffraction data are presented, which renders a real phase determination very difficult [Kolen'ko *et al.*, 2006]. The formation mechanism proposed includes the dissolution of the precursor (crystalline anatase type $TiO_2$ nanoparticles), followed by the formation of nanosheets, which roll up to form nanotubes. According to several authors [Lan *et al.*, 2005; Huang *et al.*, 2009] these nanotubes form an extended wire-like structure *via* oriented attachment and Ostwald ripening. In the widely accepted model, sodium titanate nanotubes are formed at temperatures below 135°C, while the formation of nanowires is favored above 155°C. [Umek *et al.*, 2007] Nevertheless, recent findings by Huang *et al.* show that nanotube formation is indeed possible at higher temperatures, as an inevitable step in the formation of sodium titanate nanowires, which are the thermodynamically favored product. [Huang *et al.*, 2009] The fact that previous researchers did not produce nanotubes at higher temperatures can be due to their long reaction duration.

A detailed structural analysis of the nanowires is missing as well. Recent results by Peng *et al.* [Peng *et al.*, 2008] point towards a different nanowire composition compared to nanotubes. Based on XRPD, Raman and TEM studies, these authors claim that nanowites consist of pseudo-lepidocrocite arrangement ("$Cs_2Ti_6O_{12}$") rather than $Na_2Ti_3O_7$, as previously reported [Bavykin *et al.*, 2006; Morgado *et al.*, 2007].

Knowing the crystal structure of both sodium titanate intermediate precursors and the mechanism that makes the nanotubes to evolve into nanowires might give insight into the formation mechanism of long $TiO_2$ nanorods and may aid the synthesis of a more defined reaction product.

### 1.3.3 Calcium carbonate - formation and crystallization

***Formation process***

Calcium carbonate ($CaCO_3$) is among the most common compounds on Earth and its scientific relevance is as wide-spread as its abundance. $CaCO_3$ has a pivotal role in geosciences, biology and industrial applications. It is of enormous importance for industry, mainly used as filler in plastics and for paper production, as extender in paints or in drilling fluids for the oil industry [Patnaik, 2003] or used as a raw material for construction chemicals. Finally, the effective inhibition of $CaCO_3$ scale incrustation is still a demanding question because scale may cause severe problems, such as impedance of heat transfer, increase of energy consumption, and unscheduled equipment shutdown [López-Sandoval *et al.*, 2007]. $CaCO_3$ is considered to be one of the three key biominerals besides calcium phosphate and silica. Consequently, the

crystallization behavior of calcium carbonate has been investigated for more than one century [Morse *et al.*, 2007]. Especially over the last decade, the early stages of $CaCO_3$ formation, i.e. nucleation and early growth, have drawn a lot of attention as it became increasingly evident that published data could not be reconciled with the classical nucleation and crystallization theory. A new model for $CaCO_3$ nucleation proposed by Gebauer *et al.* [Gebauer *et al.*, 2008] assumes the formation of nanometer-sized $CaCO_3$ prenucleation clusters (PNC) that are in equilibrium with hydrated $Ca^{2+}$ and $CO_3^{2-}$ and, therefore, represent the thermodynamically stable species of the single-phase system. Cryo-TEM [Pouget *et al.*, 2009] and mass spectrometry [Wolf *et al.*, 2011] as well as molecular dynamics simulations [Demichelis *et al.*, 2011] have supported the existence of PNC.

Besides CNT and PNC theories, spinodal decomposition (SD) has been postulated as an alternative precipitation pathway for $CaCO_3$ at high supersaturations. SD implies a barrier-free and hence only diffusion controlled demixing of a system. (see Chapter 1.1.3.)

### *Vaterite – structural characterization*

Vaterite, one of the common natural $CaCO_3$ polymorphs, plays a pivotal role in weathering and biomineralization processes. Vaterite is the first anhydrated phase of $CaCO_3$ to form, but it is metastable and easily transforms to calcite or aragonite after contact with water. [Faivre & Wallaeys, 1950] Calcite [Bragg, 1913] and aragonite [Bragg, 1924] grow up to well define single crystals, so their structures are well known since long time and investigated in detail. Differently from calcite and aragonite, vaterite typically forms polycrystalline spheres of 1-2 μm in diameter composed of small nanosized crystallites with size range of 10-50 nm. [Brecevic *et al.*, 1996; Andreassen, 2005] This has prevented so far any reliable structure determination. Like for many other natural and synthetic nanocrystalline materials, the structure of vaterite is still an unsolved dilemma despite its common occurrence, its relevance in biomineralization processes and the impressive number of published studies around the subject.

So far, five structural models for vaterite have been proposed over the last twenty years on the basis of X-ray diffraction [Meyer, 1959, 1969; Kamhi, 1963; Lippmann, 1973; le Bail *et al.*, 2011]. All these models have geometrically related cells that are difficult to distinguish on the basis of the low-quality data available for nanocrystalline vaterite. All models propose a single carbonate $\{CO_3\}^{2-}$ group in the asymmetric unit and mainly differ in its predicted site symmetry. Raman spectra provide controversial information, as vaterite is contaminated with other $CaCO_3$ polymorphs. [Anderson, 1996; Wehrmeister *et al.*, 2010] While Anderson [Anderson, 1996] supports Lippmann's model, [Lippmann, 1973] Gabrielli *et al.* [Gabrielli *et al.*, 2000] are in favor of Meyer's second model. [Meyer, 1969] Behrens *et al.* [Behrens *et al.*, 1995] and Wehrmeister *et al.* [Wehrmeister *et al.*, 2010] claim that none of the proposed models is consistent with the Raman spectra because they indicate the presence of two or more $\{CO_3\}^{2-}$ groups in the asymmetric unit. NMR spectroscopy studies [Bryce, 2008] of vaterite support a hexagonal symmetry but are not of help in selecting among the available models. Recently, a new structure model for vaterite with hexagonal symmetry, a longer hexagonal axis and two $\{CO_3\}^{2-}$ groups in

the asymmetric unit was proposed based on molecular dynamic simulations and geometry optimization calculations [Wang & Becker, 2009]. Although none of the vaterite models is in accord with all experimental findings, some structural features are generally accepted: (i) the Ca atoms form a hexagonal sub-lattice; (ii) all $\{CO_3\}^{2-}$ groups are oriented along the hexagonal axis; (iii) the number of formula units per unit cell (Z) is at least 12; (iv) the presence of only one $\{CO_3\}^{2-}$ group in the asymmetric unit cannot explain the observed Raman spectra.

# Chapter II. Experimental

## 2.1 Materials and syntheses

### 2.1.1 $M_2O$-$Al_2O_3$-$WO_3$ ($M$ = Na, K) system

Analytical reagent pure $Al_2O_3$, $WO_3$ and $K_2CO_3$ or $Na_2CO_3$, respectively, were used for the synthesis. This was carried out in a single zone resistance furnace ensuring maintenance of temperature with an accuracy of ± 0.2 °C (Eurotherm controller). Solutions with a mass ranging from 20 to 40 g were prepared by successive charging with portions of the mixed powdery reagents taken in a definite ratio, followed by melting in platinum crucibles with a height of 30 mm and a diameter of 30 mm. In order to achieve complete dissolution of $Al_2O_3$, the solution temperature was increased by about 100-150 °C above the expected crystallization temperature until a thoroughly transparent solution was obtained. After several hours of homogenization, the temperature was decreased relatively quickly down to values exceeding the crystallization temperature by 10-20 °C only. Further on, the temperature was decreased by 2-5 °C at every 30 min until the appearance of crystals on a platinum rod immersed in the high-temperature solution. On registration of the temperature at which these crystals appeared, part of them (about 500 mg) was withdrawn, cleaned and characterized. The whole procedure is described in details in Nikolov *et al.*, 2003*a*, 2003*b*.

### 2.1.2 Snapshots of the formation of $NaTi_3O_6(OH)\cdot 2H_2O$ nanowires

A MARS XPress microwave digestion system (CEM Corporation) was used for the microwave-assisted hydrothermal synthesis. The synthesis is based on the method published by Kasuga *et al.* [Kasuga *et al.*, 1998] with some modifications for the specific reaction system. Compared to conventional hydrothermal reactions in stainless steel autoclaves, microwave-assisted reactions offer several advantages, such as rapid heating due to a direct response of the solvent to microwaves, short cooling cycles due to the lower heat capacity of the reaction vessel compared to a stainless steel autoclave. Another advantage of the microwave-assisted pathway is the overall lower energy consumption and, most importantly, reduced reaction duration [Birkel *et al.*, 2011]. The conventional hydrothermal synthesis of sodium titanate nanowires takes at least 24 h in most cases [Bavykin & Walsh, 2009], compared to 2 h in a microwave oven. Owing to the aforementioned lower heat capacity, the microwave reaction vessel cools down radiatively in a short time, therefore it is possible to quench the reaction at every point during the synthesis. With this method it was possible to get snapshots of the reaction progress and therefore to investigate intermediate products. Each snapshot of the reaction progress was made in the same way: 500 mg of titania powder ($TiO_2$-P25, Degussa) were mixed with 50 ml of a 10 M NaOH solution (made from NaOH pellets, 98.5% p.A., Acros Organics and MilliQ Water) by vigorous magnetic stirring in a 100 ml Teflon liner for 15 minutes. Afterwards the vessel was sealed and subjected to hydrothermal treatment in a microwave furnace. The reaction mixture was heated over 10 minutes at a maximum power output of 800 W until an internal pressure of 20 bar was reached.

This pressure was kept constant for various times between 0 and 120 minutes. Afterwards the reaction mixture was allowed to cool down radiatively for 30 minutes. All reaction products were thus obtained after a heating time of 10 minutes, a reaction time of "X" minutes and a cooling period of 30 minutes (samples are referred to as "X minute samples"). The microwave system was equipped with a temperature sensor, but an exact temperature control was not possible because the sensor tubing is made from sapphire and would dissolve in the NaOH solution. After the synthesis the nanopowders were separated from the supernatant solution by centrifugation at 9000 rpm for 10 minutes and the reaction products were washed several times with methanol (99.8%, p.A., J.T. Baker) until a neutral reaction of the supernatant solution was reached. Finally, the samples were dried in vacuum overnight.

### 2.1.3 Snapshots of calcium carbonate formation

$CaCl_2 \cdot 2H_2O$ (purity > 99 %), dimethyl carbonate (DMC) (purity > 99 %) and diethyl carbonate (DEC) (purity > 99 %) were purchased from Sigma-Aldrich. The sodium hydroxide solutions were obtained by diluting a 0.1 M stock solution from Acros Organics. The precipitation experiments were performed using the Faatz-Wegner (FW) precipitation method [Faatz *et al.*, 2004], which is based on the hydrolysis of a dialkyl carbonate (DAC) precursor (dimethyl carbonate (DMC) and diethyl carbonate (DEC)) and generates carbonate under homogeneous conditions and allows to choose the rate with which supersaturation is reached by adjusting the precursor (DMC vs. DEC) and the sodium hydroxide concentration properly. In all experiments, one solution containing $CaCl_2$ and DAC precursor and a second solution containing NaOH were prepared with degassed Millipore water (18.2 MΩ) by ultrasonication for 20 minutes at water concentrations twice as high as the target concentrations. The chemicals were used without further purification. All used solutions were kept at a temperature of 20 ± 1 °C. To start the reaction, 50 mL of the NaOH solution were added dropwise to 50 mL of the $CaCl_2$/DMC or $CaCl_2$/DEC solution with the aid of a graded pipette within 90 s at a stirring rate of 400 rpm. The addition of the last droplet marks the starting point of the reaction. 40 droplets of the resulting mixture were then filtered through a Millex-VV filter unit (pore size 100 nm) into a cylindrical (20 mm outer diameter) quartz glass cuvette (Hellma). DMC and DEC were both used as carbonate precursors, resulting in different precipitation and growth kinetics.

Slow method: $[Ca^{2+}]$ = [DEC] = 15 mM, [NaOH] = 12 mM.

Fast method: $[Ca^{2+}]$ = [DMC] = 10 mM, [NaOH] = 8 mM.

### 2.1.4 Vaterite (μ-$CaCO_3$)

Two samples of synthetic vaterite, prepared by different routes, were analysed.

#### *Acqueous synthesis*

The first sample was prepared by mixing 250 mL of 0.1 M aqueous solutions of $Ca(NO_3)_2$ and 250 mL of 0.1 M $Na_2CO_3$. The suspension was stirred for 20 minutes at ambient temperature and the white product was separated by filtration, washed with water, acetone and ethanol and dried

in air at 70°C for 30 minutes [Dandeu *et al.*, 2006]. In order to obtain single vaterite nanocrystals, the sample was crushed with a FRITSCH Pulverisette 7 ball mill equipped with $ZrO_2$ balls.

***Non-acqueous synthesis***

The second vaterite sample was made by an independent non-aqueous approach [Schüler & Tremel, 2011]. Briefly, 5 mmol of calcium chloride tetrahydrate ($CaCl_2 \cdot 4H_2O$; 99.9999%, Chempur) were dissolved in 50 mL of ethylene glycol (99%+, Sigma Aldrich) by sonication at about 40°C (Elmasonic S30H, max. power 320 W, effective power 80 W, sweep mode), and 10 mmol of sodium bicarbonate ($NaHCO_3$, Ultra, Sigma Aldrich) dispersed in 50 mL of ethylene glycol by mechanical stirring were added. The resulting dispersion was heated up for 30 minutes by different methods. $CaCO_3$ nanoparticles were separated from the turbid product sol by centrifugation (9000 rpm, 30 minutes), washed two times with water and ethanol and dried *in vacuo*.

## 2.2 Material characterization

In order to characterize the above described materials electron microscopy techniques were mainly used. High-resolution transmission electron microscopy (HRTEM) and cryo-TEM for imaging of formation stages, energy disperse X-ray spectroscopy (EDX) for chemical analysis of nanoparticles and automated electron diffraction tomography (ADT) for structure solution. As an additional diffraction technique X-ray powder diffraction (XRPD) was utilized to validate and refine the results derived from electron diffraction data. Dynamic light scattering (DLS), thermogravimetric analysis (TGA) and Zeta-Potential measurements were performed additionally.

### 2.2.1 Electron microscopy and automated electron diffraction tomography (ADT)

Scanning electron microscopy (SEM) analysis was applied only for vaterite sample. SEM images were taken with a FEI Nova NanoSEM 630 SFEG scanning electron microscope working at 15 kV.

For transmission electron microscopy and automated electron diffraction tomography (ADT) investigations powdered samples were dispersed in ethanol using an ultrasonic bath and sprayed on carbon-coated copper and gold grids using a sonifier [Mugnaioli *et al.*, 2009]. Snapshots of $CaCO_3$ were prepared by taking a drop of the crystallization solution during the in situ measurement and placing it on copper grid coated with amorphous carbon.

Conventional TEM, high-resolution transmission electron microscopy (HRTEM), scanning transmission electron microscopy (STEM), selected area electron diffraction (SAED), nano electron diffraction (NED), energy-dispersive X-ray (EDX) spectroscopy and ADT measurements were carried out with a FEI TECNAI F30 S-TWIN microscope equipped with field emission gun and working at 300 kV. SAED patterns were collected with using a 10 μm area-selection aperture. TEM/HRTEM images and electron diffraction patterns were acquired

with a CCD camera (14-bit GATAN 794MSC, 1024×1024 pixels) by Gatan *DigitalMicrograph* software (Gatan Inc., Pleasanton, CA, USA). STEM images were collected by a FISCHIONE high angular annular dark field (HAADF) detector (E.A. Fischione Instruments, Export, PA, USA) and acquired by *Emispec ES Vision* software (Emispec Systems Inc., Tempe, AZ, USA).

EDX data were collected at the same microscope using an Oxford EDAX EDX spectrometer, equipped with a Si/Li detector and an ultrathin window and quantified by *Emispec TIA* software (Emispec Systems Inc., Tempe, AZ, USA). For a quantitative EDX analysis the sodium-contained samples ($Na_2O$-$Al_2O_3$-$WO_3$ system and snapshots of the formation of $NaTi_3O_6(OH)\cdot 2H_2O$ nanowires) were deposited on a gold grid, because in EDX the *K*-lines of sodium (1040.98-1071.1 eV) partially overlaps with the *L*-lines of cupper (929.7-949.8 eV).

Cryo-TEM was used only for investigation of $CaCO_3$ formation. The samples were vitrified in liquid propane using the climate chamber of a Vitrobot (FEI, Eindhoven, Netherlands) at room temperature and 80 % humidity. The cryo-TEM measurements were performed at 120 kV with a Tecnai 12 (FEI, Eindhoven, Netherlands) equipped with a BIO-TWIN-lens and a 4k×4k CCD camera (Tietz Video and Image Processing Systems GmbH, Gauting, Germany).

In order to perform structure analysis, 3D electron diffraction data were collected using an automated electron diffraction tomography (ADT) acquisition module developed for FEI microscopes [Kolb *et al.*, 2007]. In order to maximize the tilt range, all acquisitions were performed with a FISCHIONE tomography holder (MODEL 2040). A condenser aperture of 10 μm and mild illumination setting were used in order to produce a semi-parallel beam of 50 nm in diameter on the sample. Diffraction patterns were focused additionally with the diffraction lens. This introduces an effective camera length change, which can be handled through an additional calibration [Kolb *et al.*, 2011]. Crystal position tracking was performed in microprobe STEM mode and NED patterns were acquired sequentially in steps of 1°. Tilt series were collected within a total tilt range up to 120°, occasionally limited by overlapping of surrounding crystals or grid edges.

ADT data were collected both with and without electron beam precession (precession electron diffraction, PED) [Vincent & Midgley, 1994]. PED was used in order to improve the reflection intensity integration quality [Mugnaioli *et al.*, 2009], while data sets without precession were used for a more accurate cell parameter determination. PED was performed using a *SpinningStar* unit developed by *NanoMEGAS* company. The precession angle was kept at 1.2°. *ADT3D* software package coupled with *MatLab* scripts [Kolb *et al.*, 2008; Mugnaioli *et al.*, 2009] was used for 3D electron diffraction data processing. The 3D reciprocal space was visualized using *ADT3D* software or, in case of $NaTi_3O_6(OH)\cdot 2H_2O$ nanowires, using *UCSF Chimera* [Pettersen *et al.*, 2004] in order to emphasize the diffuse scattering. Only ADT/PED data were used for structure solution.

*Ab-initio* structure solution was performed assuming the kinematic approximation $I \approx F_{hkl}^2$ by direct methods implemented in the programs *SIR2008* and *SIR2011* [Burla *et al.*, 2007, 2012].

Difference Fourier maps and least square refinements were performed with the software *SHELX97* [Sheldrick, 2008]. Scattering factors for electrons were taken from [Doyle & Turner, 1968]. The scattering factor for tungsten ($M_2O$-$Al_2O_3$-$WO_3$ ($M$ = Na, K) system), as for other heavy elements, is not reported in this publication and is therefore not present in the *SIR2008/SIR2011* data banks. *SIR* is able to extrapolate the scattering of tungsten using the Mott formula. As *SHELX* doesn't offer this possibility, for refinement the scattering factors of the neighboring element tantalium were used.

### 2.2.2 X-ray powder diffraction (XRPD)

Both investigated samples in $M_2O$-$Al_2O_3$-$WO_3$ ($M$ = Na, K) system were crashed with an agate mortar. XRPD data for $K_2O$-$Al_2O_3$-$WO_3$ sample were collected using a STOE Stadi-P diffractometer equipped with a linear PSD detector in transmission by Debye-Scherrer geometry using curver germanium-monochromated Cu-$K\alpha_1$ ($\lambda$ = 0.154178 nm) radiation, tilt range $2\Theta$ = 3-70° in steps of 0.01°. XRPD for $Na_2O$-$Al_2O_3$-$WO_3$ sample were acquired using a Siemens D500 powder diffractometer using Cu-$K\alpha_1$ radiation, tilt range $2\Theta$ = 2-62° in steps of 0.02°. In case of snapshots of the formation of $NaTi_3O_6(OH)\cdot 2H_2O$ nanowires XRPD data were collected using a Bruker-AXS D8-Discover diffractometer equipped with a HiStar detector. The measurements were performed in reflection geometry using graphite-monochromated Cu-$K\alpha_1$ radiation, tilt range $2\Theta$ = 5-75° in steps 0.02°.

High resolution synchrotron powder diffraction data on the more crystalline vaterite sample obtained from non-aqueous synthesis were collected at ID31 diffractometer at the European Synchrotron Radiation Facility (ESRF). The Si (111) reflection was used to select an X-ray energy of 25 keV. The size of the beam was adjusted to 2 x 0.6 $mm^2$ using slits. The wavelength was determined as 0.049589(2) nm from a silicon standard. The samples of vaterite were contained in 0.5 mm lithium borate glass capillaries, and were rotated around theta in order to improve randomization of the crystallite orientation. The diffracted beam was analyzed with a nine-crystal analyzer stage (nine Ge (111) crystals separated by 2-theta intervals and detected with nine Na (Tl) I scintillation counters simultaneously. The incoming beam was monitored by an ion chamber for normalization of the decay of the primary beam. 15 minute scans were taken at $T$ = 298 K in continuous mode for several hours. They were later normalized and converted to step scan data for values of $2\Theta$ from 1.0° to 60.00° in steps of 0.005° ($2.2 \leq Q/nm^{-1} \leq 127.0$).

Full-pattern profile fits, Pawley fits, Rietveld refinements and attempts of structure solution were performed using TOPAS-*Academic* [Coelho, 2007*a*, 2008], applying the fundamental parameter approach for reflection profiles [Cheary & Coelho, 1992].

### 2.2.3 Zeta-Potential

Zeta-potentials measurements were performed for snapshots of the formation of $NaTi_3O_6(OH)\cdot 2H_2O$ nanowires and determined with a Malvern Zetasizer Nano ZS.

### 2.2.4 Thermogravimetric analysis (TGA)

Thermogravimetric investigations were applied only for $NaTi_3O_6(OH)\cdot 2H_2O$ nanowires and performed using a NETZSCH STA 429 Thermal analyzer. Roughly, 50 mg of the sample was placed in a ceramic sample holder, which was covered by a ceramic cap. Gases evolving upon heating the sample were released through a hole in the ceramic cap. Data evaluation was performed with the *NETZSCH Proteus* thermal analysis software (Version 4.3.1). The sample was heated from room temperature to 1373 K at a heating rate of 1 K $min^{-1}$.

### 2.2.5 Dynamic light scattering (DLS)

The dynamic light scattering (DLS) was used to investigate early stages of $CaCO_3$ formation. DLS setup consisted of an ALV-5000 correlator, equipped with an ALV/SP125 goniometer and Avalanche photodiode detector. An argon ion laser ($\lambda_0$ = 514.5 nm, $P$ = 500 mW output power) served as a coherent light source. The DLS cuvettes were cleaned by flushing with acetone for 30 minutes and filtering steps were carried out in a flow box to avoid contamination by dust. All experiments were performed at a temperature $T$ = 20°C and a scattering angle of $\Theta$ = 30°. The correlation time was adjusted to the current growth rate of the experiment and ranged from 5 to 60 s.

# Chapter III. Results

## 3.1. Ternary oxide system $M_2O$-$Al_2O_3$-$WO_3$ ($M$ = Na, K)

### 3.1.1 TEM overview and EDX

Syntheses of both $K_2O$-$Al_2O_3$-$WO_3$ and $Na_2O$-$Al_2O_3$-$WO_3$ systems result in particles of a size ranging from fifty to some hundreds of nanometers. Only the smallest particles consist of a single crystalline domain. In $K_2O$-$Al_2O_3$-$WO_3$ sample only one phase was detected by EDX, containing O, K, Al and W. The elemental ratio K:Al:W is close to 5:1:6 leading to a stoichiometry of $K_5Al(W_3O_{11})_2$ and is constant for different particles (Fig. 3.1a and b). In $Na_2O$-$Al_2O_3$-$WO_3$ sample two phases were detected. The two phases could not be easily distinguished by habit and contrast in TEM images. EDX spectra show that most of the crystals contain O, Na, Al and W, with an elemental ratio Na:Al:W close to 1:1:2 (phase II) leading to the formula $NaAl(WO_4)_2$ (Fig. 3.1c and d). Some crystals (phase I) do not contain any Al but only O, Na and W, with a ratio Na:W 1:1, comprising a stoichiometry of $Na_2W_2O_7$ (Fig. 3.1e and f). Independently ADT three-dimensional diffraction reconstructions from crystals with and without aluminum plainly show that the two phases have different cell parameters. This is in agreement with Koseva *et al.* [Koseva *et al.*, 2011], where it is claimed that it is impossible to obtain a single phase sample of sodium-aluminum tungstate *via* the described synthetic route.

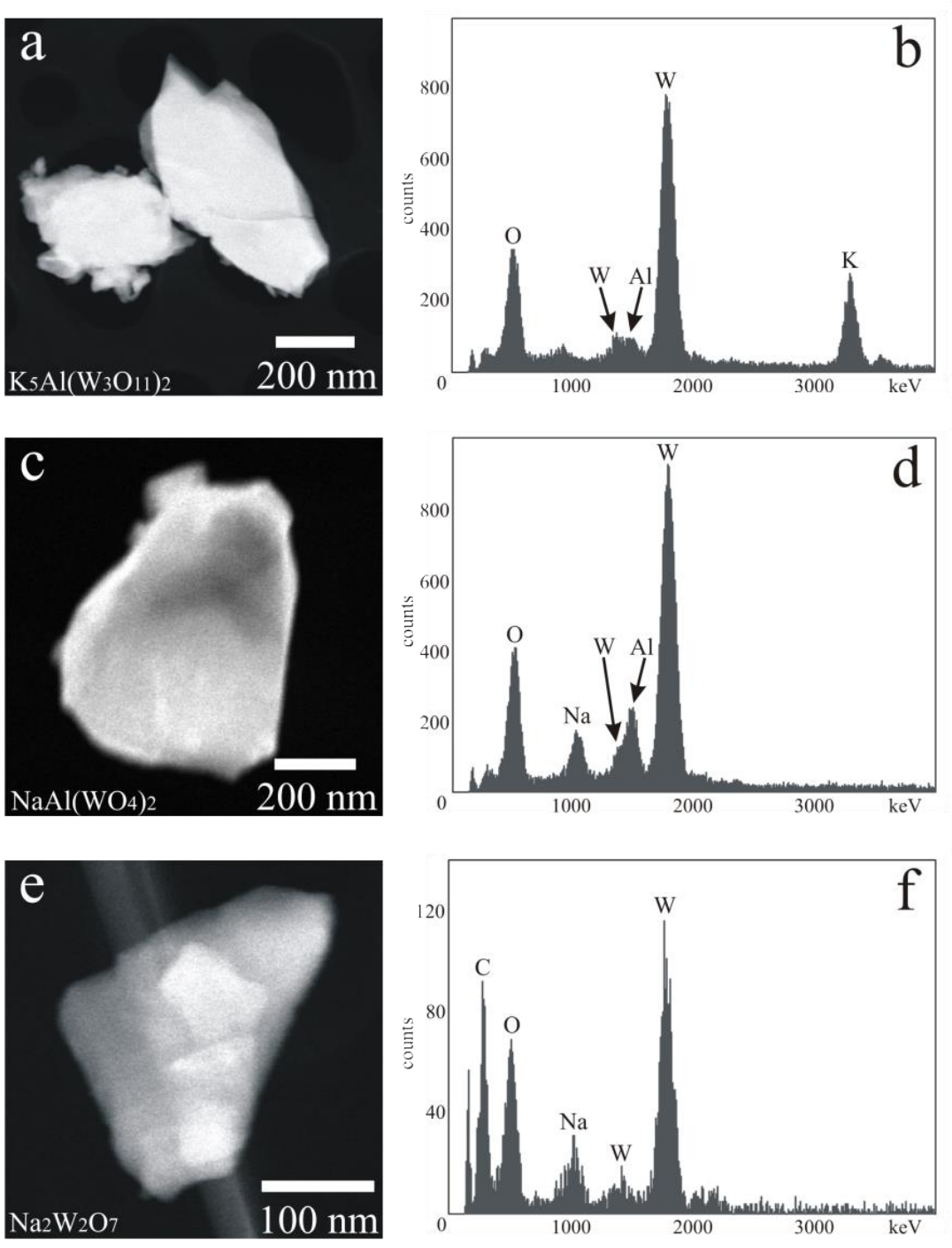


**Figure 3.1 STEM images and corresponding EDX spectra of $K_2O$-$Al_2O_3$-$WO_3$ and $Na_2O$-$Al_2O_3$-$WO_3$ samples.** (**a - b**) $K_5Al(W_3O_{11})_2$, (**c - d**) $NaAl(WO_4)_2$ (phase II) and (**e - f**) $Na_2W_2O_7$ (phase I).

### 3.1.2 ADT analysis and structure determination

***$K_2O$-$Al_2O_3$-$WO_3$ system***

Three independent ADT data sets were collected from different crystals and reconstructed in three-dimensional diffraction volumes. All diffraction volumes delivered a *C*-centered monoclinic cell (Fig. 3.2a and b and Table 3.1, first column), with weak diffuse scattering along **c***. Moreover, looking the reconstructed diffraction volume down **b*** direction (see Fig. 3.2b), it is possible to distinguish that reflections *hk*0 with *h* = 1, 3, 5 are very weak. With the availability of only low-quality diffraction data (rather ordinary for nanocrystalline materials), such evidence could easily be misinterpreted as systematic extinctions due to a glide plane orthogonal to **c***. The unambiguous cell determination derived by three-dimensional ADT data makes clear the crystallographic inconsistency of such a glide plane for a metrically monoclinic lattice. Indeed, a closer look reveals that reflections *hk*0 with *h* = 7 are fairly strong.

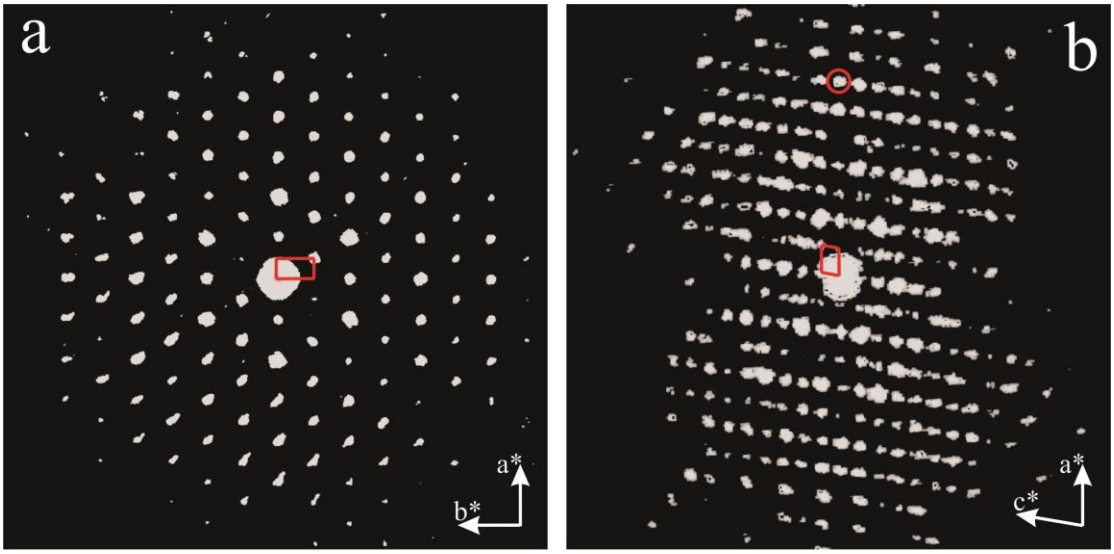


**Figure 3.2 Reconstructed three-dimensional diffraction volumes obtained by ADT data from $K_2O$-$Al_2O_3$-$WO_3$ sample.** (**a**) Diffraction volume projected down **c***. (**b**) Diffraction volume projected down **b***, where reflections 7*k*0 are marked with a circle. Cells are sketched in red.

The analysis of the internal residual after merging symmetric equivalent reflections ($R_{sym}$) showed that the Laue class is truly monoclinic (Table 3.2, first column). As no further extinction was detected, the extinction symbol was determined as *C1-1*, consistent with space groups *C2*, *Cm*, *C2*/*m*. The alleged extinctions along *hk*0 are due to a pseudo glide plane that appeared evident after the structure solution.

**Table 3.1 Selected crystallographic information and ADT experimental details for $K_5Al(W_3O_{11})_2$, $Na_2W_2O_7$ and $NaAl(WO_4)_2$.**

| System | $K_2O$-$Al_2O_3$-$WO_3$ | $Na_2O$-$Al_2O_3$-$WO_3$ | |
|---|---|---|---|
| | $K_5Al(W_3O_{11})_2$ | Phase I $Na_2W_2O_7$ | Phase II $NaAl(WO_4)_2$ |
| ***Crystallographic information*** | | | |
| space group | *C2* | *Cmce* | *C2/c* |
| *a* (Å) | 13.59 | 7.22 | 9.66 |
| *b* (Å) | 7.81 | 11.90 | 5.40 |
| *c* (Å) | 19.88 | 14.72 | 13.04 |
| *α* (°) | 90 | 90 | 90 |
| *β* (°) | 99.17 | 90 | 90.18 |
| *γ* (°) | 90 | 90 | 90 |
| no. of independent atoms | 36 | 9 | 8 |
| ***Experimental details*** | | | |
| tilt range (°) | 2×(-60/+60) | 2×(-60/+60) | -60/+60 |
| no. of total reflections | 6518 | 2867 | 1528 |
| no. of independent reflections | 1843 | 454 | 565 |
| resolution (Å) | 0.8 | 0.9 | 0.8 |
| reflection coverage (%) | 84 | 91 | 81 |
| $R_{sym}$ (%) | 13.15 | 17.97 | 17.12 |
| overall *U* (Å$^2$) | 0.032 | 0.026 | 0.036 |
| residual *R*(F) (*SIR*2011) (%) | 19.71 | 19.45 | 25.30 |
| reflections / parameter ratio | 13.5 | 16.2 | 23.5 |
| residual *R*1(F) (*SHELX*97) (%) | 20.97 | 25.01 | 26.60 |

For *ab-initio* structure solution and structure refinement two precessed tilt series with orthogonal tilt axis were acquired from the same nanocrystal. The resulting integrated intensities were merged with a scale factor of 1. Structure solution in space group *C2* converged to a solution with a final residual *R* of 19.71%. Structure solutions in space groups *Cm* and *C2*/*m* didn't converge to any crystallochemical interpretable structure and were characterized by higher residuals (21.32% for *Cm* and 25.95% for *C2*/*m*).

The potential map obtained for space group *C2* has 6 strong maxima (from 6.40 to 5.41 e/Å$^3$) corresponding to the 6 independent tungsten atoms. The next 8 maxima (from 2.94 to 2.28 e/Å$^3$) corresponded to the 2 aluminum and the 6 potassium positions. Remarkably potassium atoms should have a higher scattering potential than aluminum, but their maxima are less sharp due to weaker coordination and a related higher thermal factor. The next 20 maxima corresponded to oxygen atoms (from 1.40 to 0.77 e/Å$^3$). Two missing oxygen positions were actually detected in the first Fourier map. The final composition was $K_5Al(W_3O_{11})_2$, consistent with the EDX analysis.

### *$Na_2O$-$Al_2O_3$-$WO_3$ system*

Two phases were detected inside the sample $Na_2O$-$Al_2O_3$-$WO_3$, either on the basis of EDX and ADT data (see Fig. 3.1 and Fig. 3.3). The two phases are respectively characterized by the absence (phase I) or presence (phase II) of aluminum. Both phases show a pseudo-hexagonal lattice. For phase II vectors **a** and **b** have respectively lengths of 5.55 and 5.40 Å and γ angle is 120.91°. This cell is metrically hexagonal inside the ADT error for cell parameter determination, estimated as 2-3% for cell lengths and 1° for cell angles [Kolb *et al.*, 2011]. The real symmetry of the structure could be unrevealed only through the analysis of the three-dimensional reflection intensity distribution. Both phase I and phase II data delivered a rather high $R_{sym}$ for all possible hexagonal or trigonal crystal families (Table 3.2). Both cells were then transformed in *C*-centered orthorhombic lattices (see Table 3.1, second and third columns). The convenient orthorhombic cell (among the three possible transformations shown in Fig. 3.3a) was the one with the lowest $R_{sym}$.

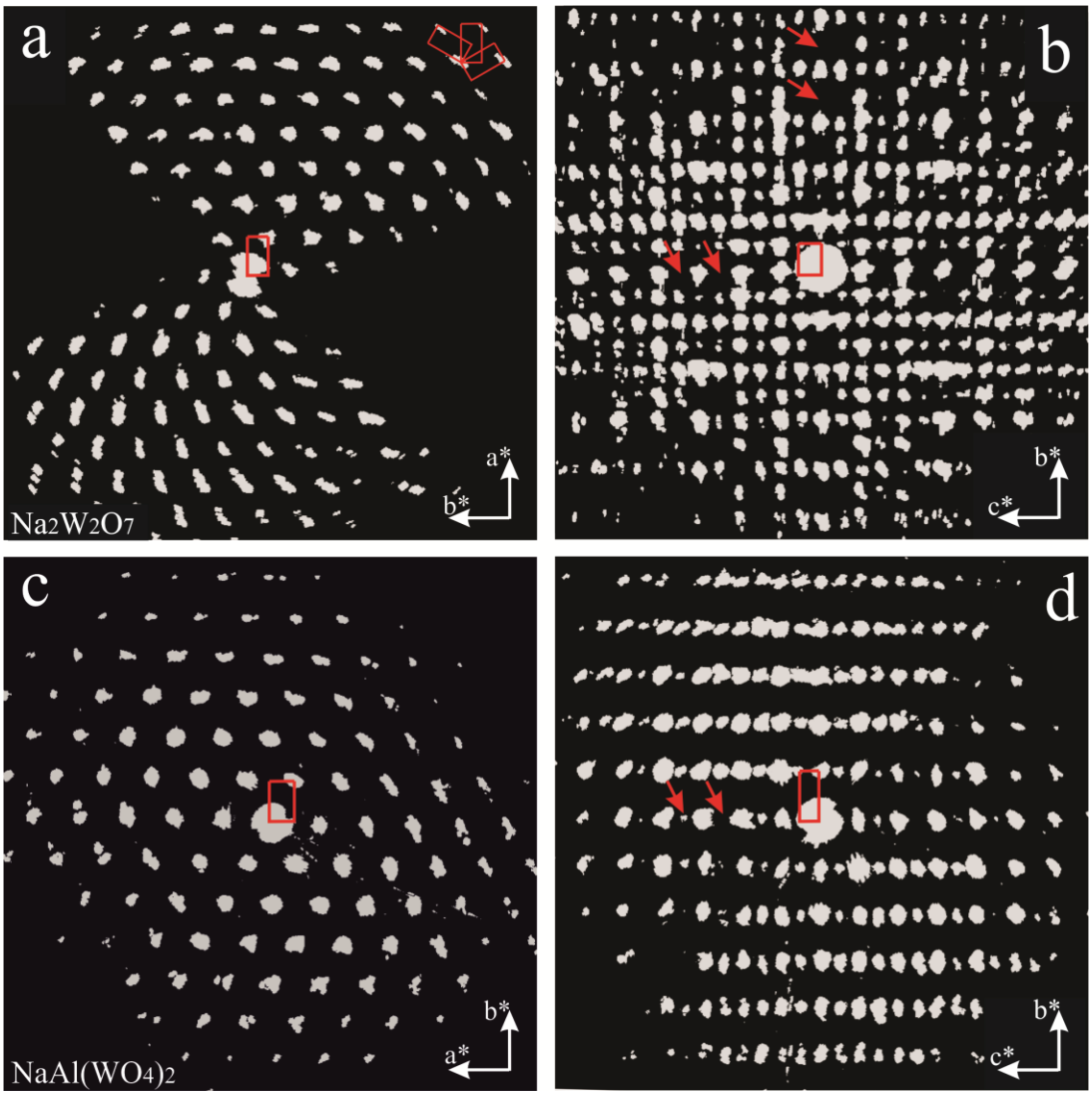


**Figure 3.3 Reconstructed three-dimensional diffraction volumes obtained by ADT data from $Na_2O$-$Al_2O_3$-$WO_3$ sample.** $Na_2W_2O_7$ (phase I) diffraction projected down **c*** (**a**) and **a*** (**b**). $NaAl(WO_4)_2$ (phase II) diffraction projected down **c*** (**c**) and **a*** (**d**). Cells are sketched in red. In the upper-right corner of (**a**) the three possible *C*-centered orthorhombic cells suitable to describe the diffraction volume are shown in red. Extinctions due to *c*-glide planes are marked by arrows.

For phase I the $R_{sym}$ associated with the orthorhombic symmetry (Laue class *mmm*) is significantly lower than the one associated with any hexagonal or trigonal Laue class (Table 3.2). Extinctions are consistent with extinction symbol *C–c*(*ab*) (Fig. 3.3b). *Ab-initio* structure solution of this phase in space group *Cmce* (formerly named *Cmca*) resulted in the known structure of $Na_2W_2O_7$, previously determined based on single crystal X-ray data by Okada *et al.* (1975).

For phase II no reduction of $R_{sym}$ was observed after the transformation into the orthorhombic setting. Extinctions were consistent with extinction symbol *C–c–* (Fig. 3.3c and d), associated with space groups *Cmc2*$_1$, *C2cm* and *Cmcm*. Though, no structure solution in any of these space groups did converge. A further reduction of symmetry led to monoclinic Laue class "*1 2/m 1*".

After this transformation we observed a reduction of $R_{sym}$ down to 17.18% (Table 3.2). Such reduction is significant even assuming that in part it is due to the physiological relaxation of the symmetry constrains [Camalli *et al.*, 2012].

**Table 3.2 $R_{sym}$ (%) of ADT data associated with different Laue classes for $Na_2W_2O_7$ and $NaAl(WO_4)_2$.** The higher symmetry space groups were selected for the test: *P6/mmm*, *P6/m*, *P-31m*, *P-3m1*, *P-3*, *Cmmm* and *C2/m*. In bold is indicated the correct Laue class.

| Laue class | $Na_2W_2O_7$ | $NaAl(WO_4)_2$ |
|---|---|---|
| *6/mmm* | 32.81 | 33.01 |
| *6/m* | 28.07 | 32.53 |
| *-31m* | 31.68 | 31.85 |
| *-3m1* | 31.06 | 25.13 |
| *-3* | 25.37 | 23.09 |
| *mmm* | **18.27** | 25.87 |
| *2/m* | 16.87 | **17.22** |

The resulting extinction symbol is *C1c1*, and indeed a structure solution was achieved straightforwardly in space group *C2*/*c*. The strongest two maxima (6.41 and 2.79 e/Å$^3$, respectively) in the potential map corresponded to tungsten and aluminum atoms. The following four peaks (from 1.64 to 1.02 e/Å$^3$) corresponded to oxygen atoms and the seventh peak (0.79 e/Å$^3$) to sodium. As observed for $K_5Al(W_3O_{11})_2$, the potential corresponding to the alkaline atom is smeared down. In accordance with EDX data, the final composition for phase II was $NaAl(WO_4)_2$. This structure is isotypic with $NaFe(MoO_4)_2$ [Klevtsova, 1975], as already proposed by Kolb *et al.* [Kolb *et al.*, 2005] on the basis of metric, symmetry and compositional resemblances determineted by conventional diffraction and spectroscopic measurements.

### 3.1.3 X-ray powder diffraction

Attempts to solve $K_5Al(W_3O_{11})_2$ structure by direct methods implemented in *EXPO*2009 [Altomare *et al.*, 2009] based on X-ray powder diffraction data were not successful due to overlapping reflections in the medium-high resolution range. A Rietveld refinement was carried out with *TOPAS-Academic* [Coelho, 2008] using atomic positions and cell parameters obtained by electron diffraction data as starting values. Four tungstate $WO_6$-octahedra, two tungstate $WO_5$-pyramids and two aluminate $AlO_4$-tetrahedrons were restrained. The potassium was refined absolutely free. Refined atomic positions were similar to the starting model. Taking into account a preferred orientation along [001], the refinement converged at $R_{wp}$ = 7.0 % (Fig. 3.4a). The geometry of one aluminate tetrahedron (Al1) is distorted (one angle is 130°). Except for aluminum, the isotropic thermal factor values are acceptable. Selected crystallographic and experimental parameters are listed in Table 3.3.

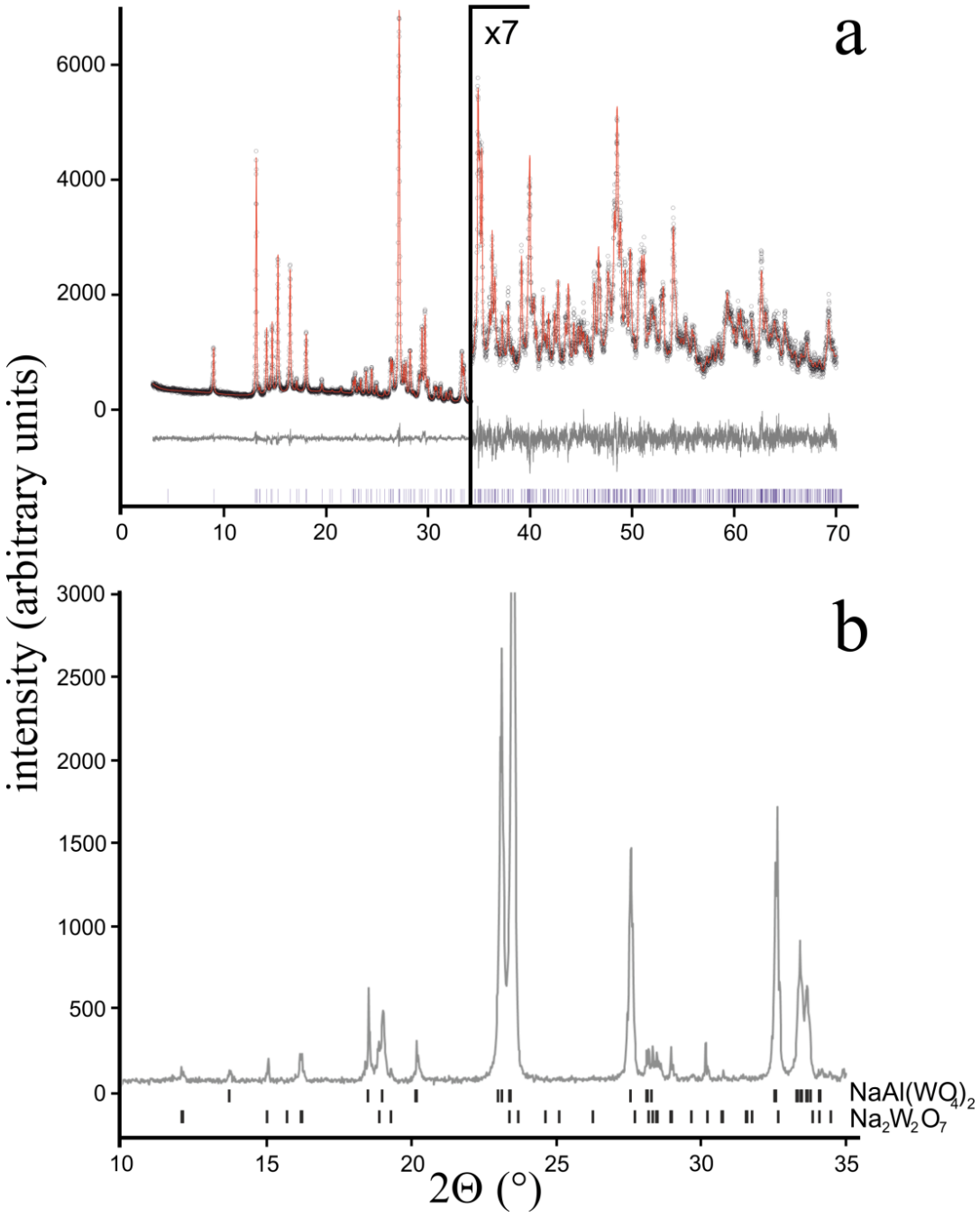


**Figure 3.4 XRPD data from $K_2O$-$Al_2O_3$-$WO_3$ and $Na_2O$-$Al_2O_3$-$WO_3$ samples.** (**a**) Rietveld refinement of $K_5Al(W_3O_{11})_2$. calculated patterns (red), experimental patterns (black) difference plot (grey). (**b**) XRPD pattern of $Na_2O$-$Al_2O_3$-$WO_3$ sample. Ticks mark the interatomic distances of $NaAl(WO_4)_2$ (phase II) and $Na_2W_2O_7$ (phase I).

$Na_2O$-$Al_2O_3$-$WO_3$ sample is a multiphasic mixture of $NaAl(WO_4)_2$ and $Na_2W_2O_7$ and its XRPD pattern (Fig. 3.4b) includes reflections belonging to both phases. Cell parameters of both phases were refined against XRPD data ($R_{wp}$ = 24.0 % after poly-fit). $NaAl(WO_4)_2$ peaks are stronger, consistently with the higher amount of this compound. No Rietveld refinement was attempted for this sample. The volumetric ratio $NaAl(WO_4)_2$ : $Na_2W_2O_7$ was estimated as 3.3.

**Table 3.3 Selected crystallographic information and experimental details for the Rietveld refinement of $K_5Al(W_3O_{11})_2$.**

| **Refined structure** | **$K_5Al(W_3O_{11})_2$** |
|---|---|
| ***Crystallographic information*** | |
| space group | *C2* |
| *a* (Å) | 13.6173(5) |
| *b* (Å) | 7.8285(3) |
| *c* (Å) | 19.9191(9) |
| *ß* (°) | 99.164(2) |
| V (Å$^3$) | 2096.31(56) |
| $B_{iso}$(W) (Å$^2$) | 1.58 |
| $B_{iso}$(Al1) (Å$^2$) | -3.80 |
| $B_{iso}$(Al2) (Å$^2$) | -1.47 |
| $B_{iso}$(K) (Å$^2$) | 2.04 |
| $B_{iso}$(O) (Å$^2$) | 2.65 |
| ***Experimental details*** | |
| 2$\Theta$ range (°) | 3.0 – 70.0 |
| $\Delta 2\Theta$ (°) | 0.1 |
| $R_p$ (%) | 5.7 |
| $R_{wp}$ (%) | 7.0 |
| $R_{exp}$ (%) | 5.4 |
| GoF | 1.2 |
| preferred orientation | 27% in (001) |
| no. of observations | 6700 |
| no. of reflections | 519 |
| no. of parameters | 146 |
| no. of geometrical restraints | 78 |

### 3.1.4 Refinement against electron diffraction data

Least square refinements of $K_5Al(W_3O_{11})_2$, $Na_2W_2O_7$ and $NaAl(WO_4)_2$ were performed against ADT data, imposing soft geometrical restraints (SADI) on Al-O and W-O distances and using the cell parameters refined by XRPD. All refined structures were characterized by reasonable atomic distances and regular polyhedra of coordination for aluminum and tungsten cations (Fig. 3.5 and 3.6). Remarkably, all thermal factors were positive and inside a reasonable range. Potassium and sodium atoms have in average higher thermal factors, as expected due to their loose coordination. Differences in atomic positions between refinement against XRPD and refinement against ADT data are listed in Table 3.4.

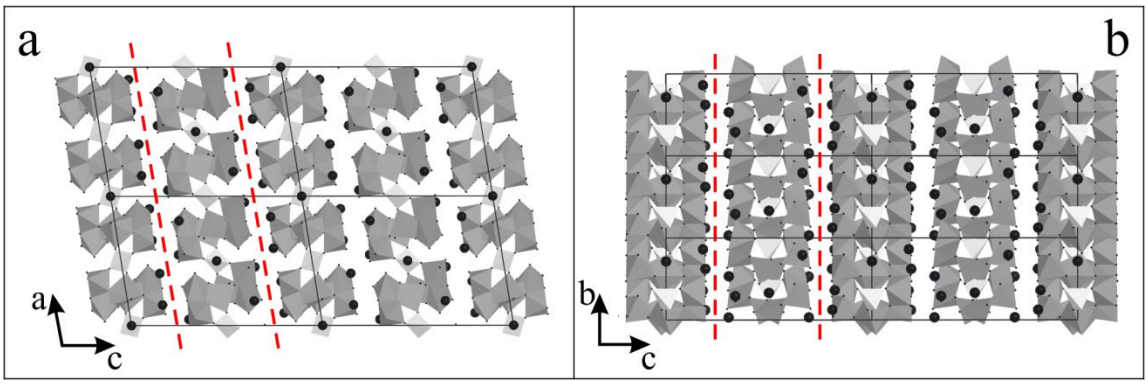


**Figure 3.5 $K_5Al(W_3O_{11})_2$ crystal structure.** (**a**) View down [010] projection. (**b**) View down [100] projection. $WO_5$-square pyramids are shown in dark grey, $AlO_4$-tetrahedra in light grey and K atoms in black. Pseudo-glide planes orthogonal to **c*** are marked by dashed lines.

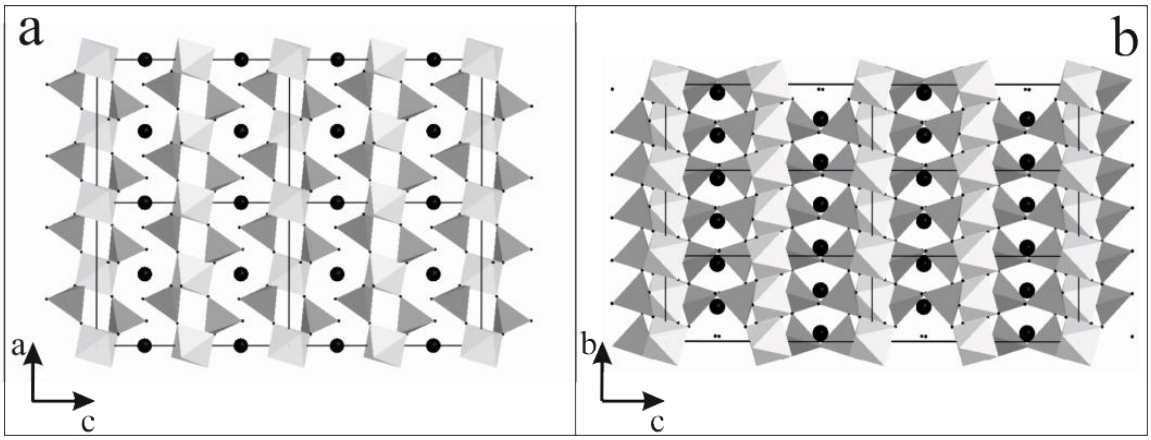


**Figure 3.6 $NaAl(WO_4)_2$ crystal structure.** (**a**) View down [010] projection. (**b**) View down [100] projection. $WO_4$-tetrahedra are shown in dark grey, $AlO_6$-octahedra are in light gray and Na atoms in black.

The final residual, although high when compared with structure refinements against X-ray diffraction data (Table 3.1), is in the range of other reported refinements performed with electron diffraction data [Klein, 2011; Kolb *et al.*, 2011]. The high residual is likely due to persistent dynamical effects and the missing corrections for absorption and Lorentz factor. Despite the higher residual, all the three structures could be refined imposing only soft restrains, Al and W form rather regular coordination polyhedral and all atoms have reasonable isotropic thermal factors.

**Table 3.4 Differences in atomic positions between refinement against XRPD data and refinement against ADT data for $K_5Al(W_3O_{11})_2$.**

| | W | Al | K | O |
|---|---|---|---|---|
| **Average (Å)** | 0.05188 | 0.06480 | 0.19247 | 0.32111 |
| **Maximum (Å)** | 0.06661 | 0.10928 | 0.32745 | 0.77549 |

## 3.2 Snapshots of $NaTi_3O_6(OH)\cdot 2H_2O$ nanowires formation

### 3.2.1 X-ray powder diffraction

Figure 3.7 compares X-ray powder diffraction (XRPD) patterns of the "snapshot samples" obtained at different stages of the reaction with the diffractogram of $TiO_2$-P25 precursor nanoparticles. $TiO_2$-P25 powder is a standard material in the field of photocatalytic reactions, which contains a phase mixture of anatase (73-85%), rutile (14-17%) and amorphous $TiO_2$ (0-18%) [Ohtani *et al.*, 2010].

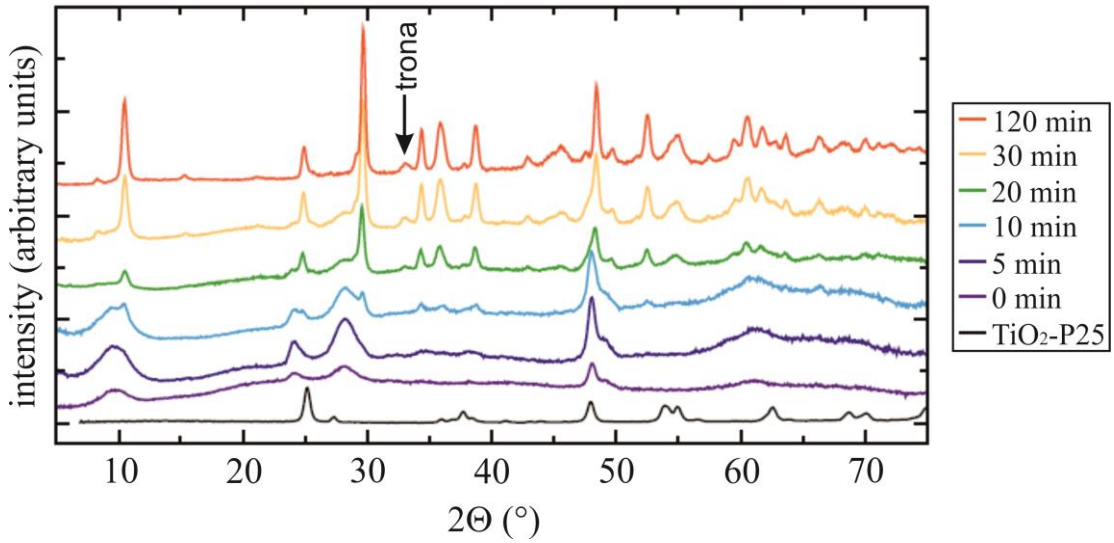


**Figure 3.7 XRPD patterns of the snapshots during the $NaTi_3O_6(OH)\cdot 2H_2O$ formation.** $TiO_2$-P25 (bottom trace) and samples obtained after hydrothermal treatment of $TiO_2$-P25 after 0, 5, 10, 20, 30 and 120 minutes (sequence from bottom to top). A reflection belonging to the trona impurity is marked with an arrow.

All reflections of the $TiO_2$-P25 precursor had vanished after a 10 minute heating ramp ("0 minute sample") and new broad reflections appeared at $2\Theta$ = 9.6°, 24.2°, 28.2°, 48.0° and 61.2° (equivalent to *d*-values 9.2 Å, 3.7 Å, 3.2 Å, 1.9 Å and 1.5 Å). These reflections could not be assigned to any known $TiO_2$ polymorph which indicates that already at this stage the precursor has completely reacted with the NaOH solution forming a new compound.

After a reaction time of 5 minutes, these reflections are still the only feature observed in the XRPD pattern, but their intensities increase and their profiles become sharper.

Reflections of the final product started to appear after 10 minutes at $2\Theta$ = 10.5°, 24.9°, 29.6° and three additional reflections around 36° (equivalent to *d*-values 8.4 Å, 3.6 Å, 3.0 Å and 2.5 Å), while all reflections of the unidentified intermediate compound were still present. The main intensities of the final product were in the high scattering angle flanks of the reflections of the first intermediate phase, which indicates a mutual structural relation, i.e. a systematic decrease of lattice parameters due to progressive ordering or dehydration processes.

The reflections assigned to the final product became more prominent with increasing reaction time, while those of the intermediate vanish progressively. After 20 minutes the reflections of the transient phase appeared only as weak shoulder in the low angle flanks of the reflections of the final product (5-10 % weight, based on the peak profiles of the intermediate). After the reaction was complete (120 minutes) the diffractogram showed only intensities of the final product.

The product of the hydrothermal reaction also contains a small amount (estimated at 1-2 % volume) of $Na_3(CO_3)(HCO_3)\cdot 2H_2O$ (trona) [Shirpour *et al.*, 2013].

### 3.2.2 HRTEM, SAED and EDX

#### *$TiO_2$-P25 precursor*

The commercial precursor Degussa $TiO_2$-P25 consists (as shown by TEM in Fig. 3.8) of irregularly shaped nanoparticles with the diameters ranging from 10 nm to 100 nm, the majority of the particles being in the size range of 20-40 nm. The $TiO_2$-P25 nanoparticles have the tendency to aggregate.

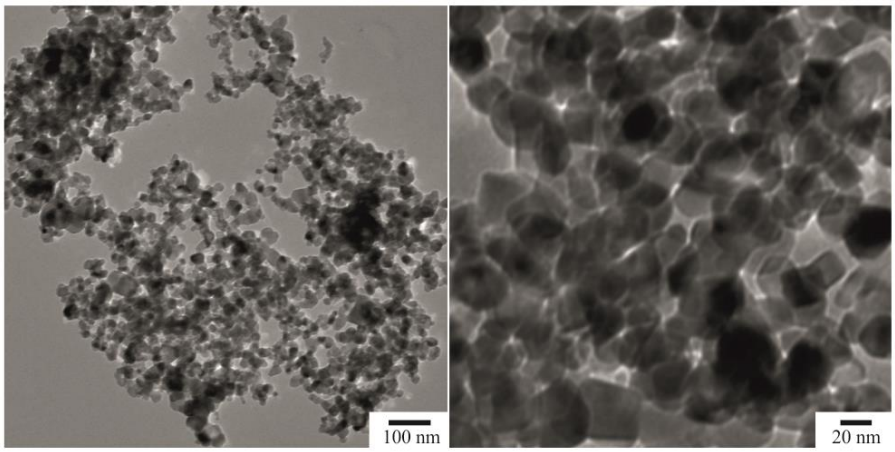


**Figure 3.8 TEM overview images of $TiO_2$-P25 precursor.**

#### *Short reaction times ("0-3 minute samples")*

Figure 3.9 shows TEM images of the "0 minute sample". At this stage the sample consists mainly of flake-like and relatively bulky aggregates of nanosheets and nanotubes. The nanotubes have a strong tendency to aggregate, despite continuous stirring of the reaction mixture. However, few isolated nanotubes were observed (Fig. 3.9b). Tube lengths range from 30 to several hundred of nanometers, the diameter of the nanotubes being always approximately 10 nm.

No trace of the precursor and no amorphous sodium titanate nanoparticles (as reported by Huang *et al.*, 2011) for reaction in caustic solution were found, i.e. amorphous nanoparticles are not a necessary and unavoidable step in the formation of nanowires.

Nanosheets of sodium titanate intermediate roll up to form nanotubes. At this stage different shapes can be distinguished: (i) irregular nested onion-like particles, (ii) scrolls, and (iii) regular open nanotubes (Fig. 3.9c). The terms "nanotube" is used here for indicating all these wrapped shapes. The nanotubes are crystalline and their wall thickness is usually from two to five layers (Fig. 3.9c and d). The *d*-spacing between two adjacent layers is 7.5-8.0 Å (equivalent to $2\Theta$ = 11.8°-11.1°). A second *d*-spacing of about 3.7 Å (equivalent to $2\Theta$ = 24.0°) is also frequently observed.

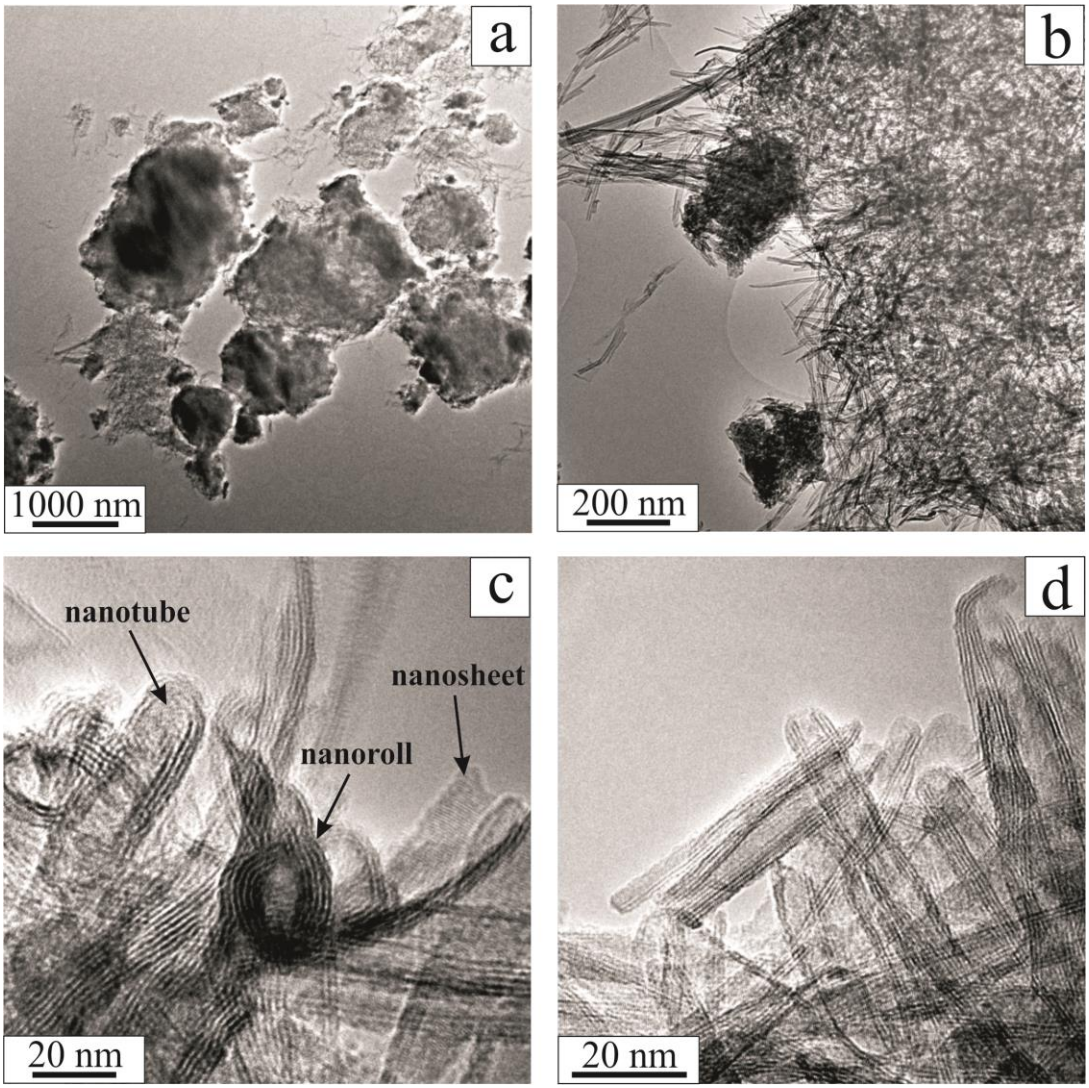


**Figure 3.9 TEM overview images of the sodium titanate sample directly after 10 minutes heating ramp ("0 minute sample").** (**a**) Overview of flake-like nanosheets and nanotubs aggregates. (**b**) Rim of an aggregate showing agglomerated nanoscrolls/nanotubes. (**c**) HRTEM of a section from (**b**), showing nanosheets, nanoscrolls/nanotubes and nested fullerene-like nanoparticles. (**d**) HRTEM of an aggregate showing both well defined and irregular nanoscrolls/nanotubes.

EDX analysis confirms the presence of Na:Ti in a ratio of 1:4, both for the flake-like aggregates and the isolated nanotubes. TEM analyses of reaction snapshots after 1 and 3 minutes do not

show any significant difference to the "0 minute sample"; the length and diameter of the nanotubes remains constant.

Beside the tubes, roundish particles with a diameter of 5-30 nm can be observed (Fig. 3.10a). EDX analysis on these nanoparticles revealed only sodium and oxygen but no titanium. It is likely that they are, in fact, trona ($Na_3(CO_3)(HCO_3)\cdot 2H_2O$) [Shirpour *et al.*, 2013]. Due to the low solubility of sodium bicarbonate and sodium carbonate in methanol [Ellingboe & Runnels, 1966], they could not be fully removed by the washing process. Similar observations were also made by other groups [Peng *et al.*, 2008]. It is difficult to establish if these particles are present in the solution or just precipitate when the sample is dried. In any case these particles are present with the same characteristics in all the snapshot samples, indicating that until the end the solution is oversaturated in $Na^+$ ions.

### *Intermediate reaction times ("5-10 minute samples")*

After a reaction time of 5 minutes the sample still contained flake-like aggregates and isolated nanotubes (Fig. 3.10a and b). The amount of isolated nanotubes increased but the tube length and diameter remained unchanged. The tubes became more regular, and the nested fullerene particles disappeared.

Flake-like aggregates and isolated nanotubes showed equivalent electron diffraction pattern with typical *d*-values of 3.7, 3.0, 2.4 and 1.9 Å (equivalent to $2\Theta$ = 24.0°, 29.7°, 37.4° and 47.8°), i.e. aggregates and nanotubes can be assumed to have the same phase composition.

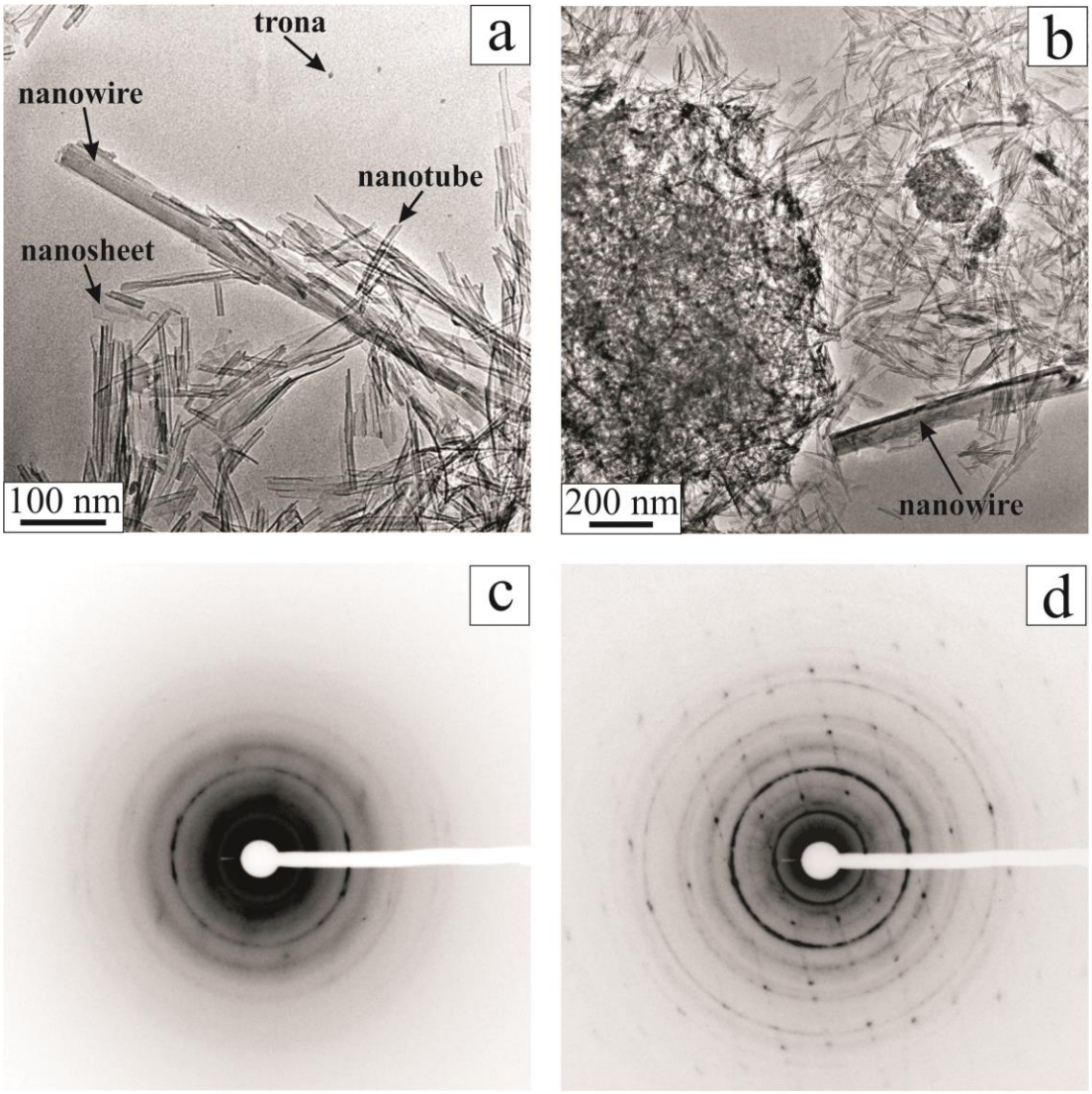


**Figure 3.10 TEM overview images of the sodium titanate sample after 10 minutes heating ramp and 5 minutes of reaction time ("5 minute sample").** (**a - b**) Overview images showing the nanotubes and nanowires. (**c**) SAED pattern of a flake-like aggregate. (**d**) SAED pattern of a bundle of nanotubes (diffraction rings) and a nanowire (diffraction dots).

In addition, wire-like structures with maximum diameters of 80 nm and a maximum length of 2 µm appeared. SAED (Fig. 3.10d) confirmed that the nanowires are a different phase, actually the final product, and they are significantly more crystalline than the nanotubes. The Na:Ti ratio for the nanowires was 1:2, independent from the reaction time.

After reaction time of 10 minutes the amount and average size of the nanowires increase significantly (Fig. 3.11a). A nanowire length can reach several micrometers, yet many much shorter wires are found as well.

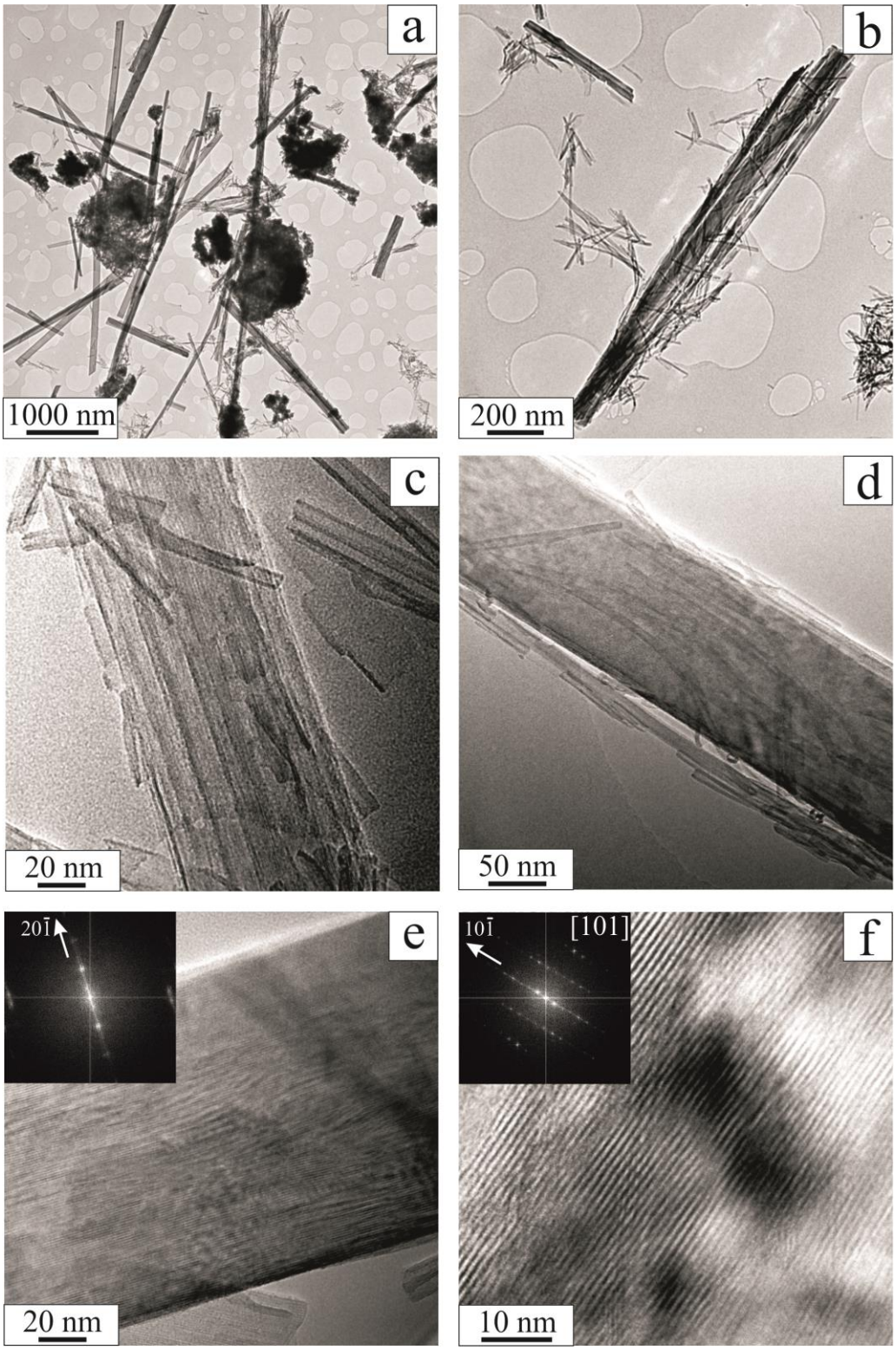


**Figure 3.11 TEM overview images of the sodium titanate sample after 10 minutes heating ramp and 10 minutes of reaction time ("10 minute sample").** (**a**) Overview image showing flake-like aggregates and nanowires. (**b**) Bundles of nanotubes and nanowires. (**c**) A bundle of oriented nanotubes surrounding a nanowire. (**d**) Nanowire with oriented nanotubes at the surface. (**e - f**) HRTEM images of a nanowire showing bent layers and stacking faults. Insets show the corresponding Fourier transforms.

The nanowires were surrounded by nanotubes (Fig. 3.11b), which attach along the long rim (Fig. 3.11c and d) and form in this way closely packed and oriented bundles. The core of the bundles usually consists of one or more small nanowires. Bigger nanowires still have a number of nanotubes attached along the long rim and the actual border of the wire shades progressively in bundles of oriented nanotubes. This morphological evolution of nanotubes into nanowires can be described by Ostwald ripening, which for the first time was proposed in 2005 by Lan *et al.* [Lan *et al.*, 2005]. Later Huang *et al.* displayed that the Ostwald ripening process is accompanied by the oriented attachment mechanism [Huang *et al.*, 2009].

HRTEM of the nanowires revealed a layered structure with pervasive lateral and stacking disorder, resulting in bent layers and stacking faults (Fig. 3.11e and f). The disorder is more pronounced for small wires. The overall crystallinity of the nanowires increases with the progression of the reaction, probably due to annealing effects.

The nanowires were distinctly non-porous, in contrast to a study by Huang *et al.* [Huang *et al.*, 2009], who reported the formation of porous wires that were filled subsequently with amorphous sodium titanate particles from the reaction mixture. Based on our current findings, this mechanism seems unlikely, as no amorphous sodium titanate was found in the reaction mixture during the first wire appearing. Still, the experimental conditions in this study were different from those of Huang *et al.*, and differences might be attributed to this fact.

Isolated nanotubes and flake-like aggregates were also present after 10 minutes of reaction although in lower relative amounts. The size of the tubes remains unchanged, and SAED and EDX showed their structure and chemical composition to be identical to those in the "0 minute sample". The tubes did not undergo any morphological or chemical change before their transformation into nanowires, i.e. they serve as a reservoir for subsequent nanowire growth.

### *Final product ("120 minute sample")*

With increasing reaction time the relative amount and size of the wires increased, while nanotubes and flake-like aggregates reduced until disappearing completely after 120 minutes. The final diameter of the nanowires was in the range from 50 to 500 nm, their lengths could reach several micrometers (Fig. 3.12a). HRTEM images (Fig. 3.12b-d) show an increasing crystalline order of the nanowire structure; some stacking faults and bent layers remained, but with a much lower frequency. As visible in the corresponding Fourier transforms diffuse scattering still occurs along **c***.

The microwave-assisted hydrothermal reaction turned out to be complete after 2 h; the reaction duration is one order of magnitude faster than a hydrothermal synthesis in a conventional stainless steel autoclave.

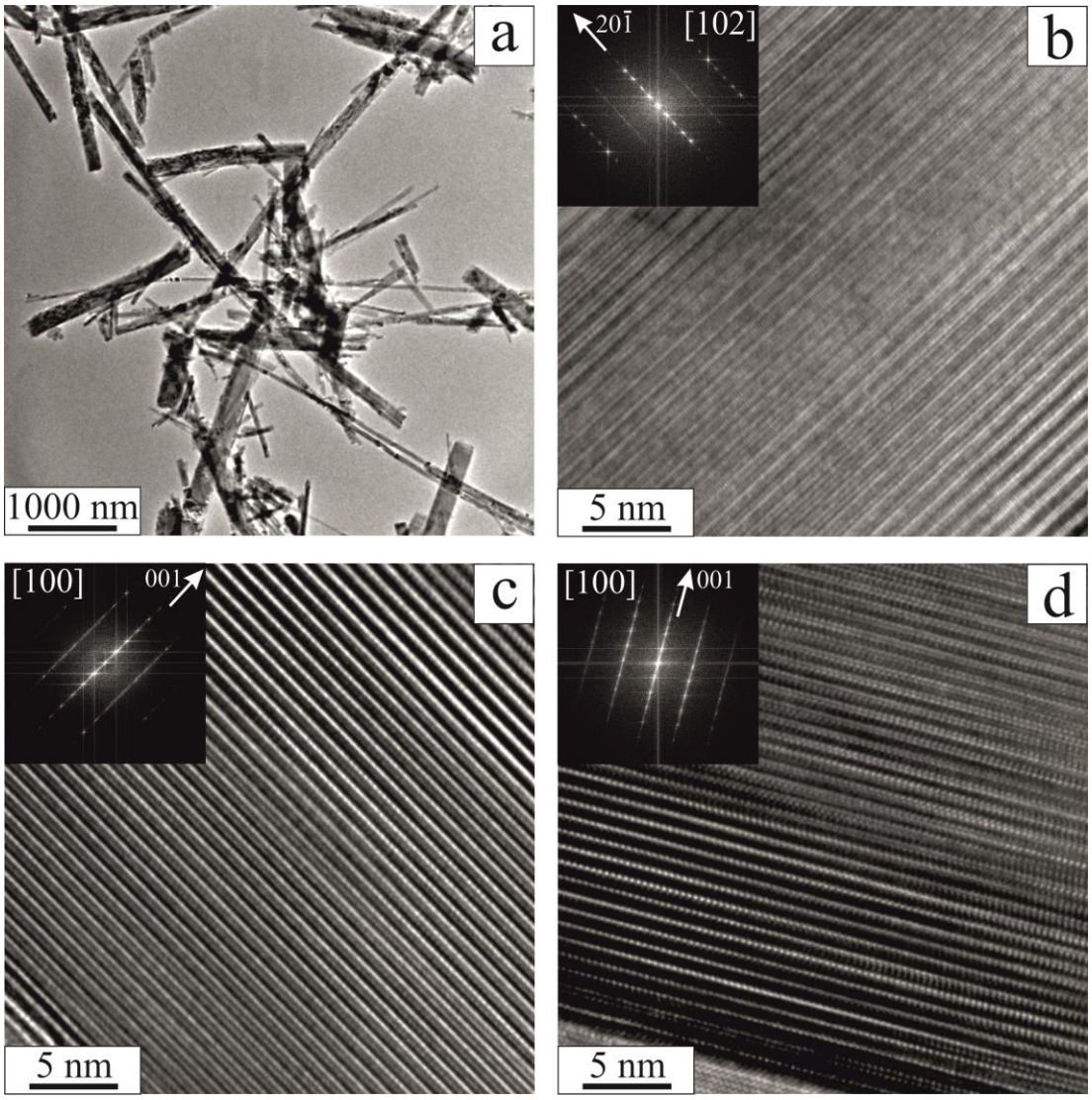


**Figure 3.12 TEM overview images of the sodium titanate sample after 10 minutes heating ramp and 120 minutes of reaction time ("120 minute sample").** (**a**) Overview image. (**b**) HRTEM images and corresponding Fourier transforms of nanowires along [102], showing no diffuse scattering along 20-1. (**c-d**) HRTEM images and corresponding Fourier transforms of a nanowire along [100] showing diffuse scattering along 001.

### 3.2.3 Zeta-Potential

The nanotube intermediates as well as the nanowires show a strong tendency to form aggregates. This tendency is more pronounced for the nanotubes, which may grow in a solution-condensation-type process $[Ti(H_2O)_m(OH)_n] \rightarrow [Ti_mO_n(OH)_o]_{(4m-2n-o)} \rightarrow TiO_2$ onto the edges of the wires *via* oriented attachment [Yuwono *et al.*, 2010]. This preference can be related to the surface charge of the tubes and wires (Zeta-Potential for the nanotubes: –52.3 mV; for the nanowires: +5.04 mV). The transformation of nanotubes to nanowires is accompanied by a chemical reaction of the titanate nanotubes with NaOH, resulting in an increment of sodium in the nanowires. The different chemical composition and crystal structure of nanotubes and nanowires indicate that this reaction is a key step in the formation of sodium titanate nanowires. This process shows that the

morphological and structural changes of the product are intimately connected and related to the sample composition.

### 3.2.4 Thermogravimetric analysis (TGA)

TGA of the final product show several stages of weight loss in the sample (Fig. 3.13). The initial step below 150 °C can be described as a release of physisorbed water [Shirpour *et al.*, 2013]. From 150 °C to 300 °C the weight decreases by 7% from its initial value. According to Peng *et al.* [Peng *et al.*, 2008], who investigated a sodium titanate synthesized under similar reaction conditions, this can be attributed to the decomposition of carbonates. Shirpour *et al.* [Shirpour *et al.*, 2013], who investigate the same system, claim that structural changes (the appearance of a second layered phase with smaller interlayer spacing) are taking place during this step. The weight loss in the region between 300 °C and 600 °C arises from a continued slow release of water from the nanowires. After this stage, 91.5% of the initial weight remains. At 600 °C an abrupt loss of water is observed and the sample is completely dehydrated. At higher temperatures the sample does not undergo any further change of weight. In total, 90.5% of the initial weight remains at the end of the experiment.

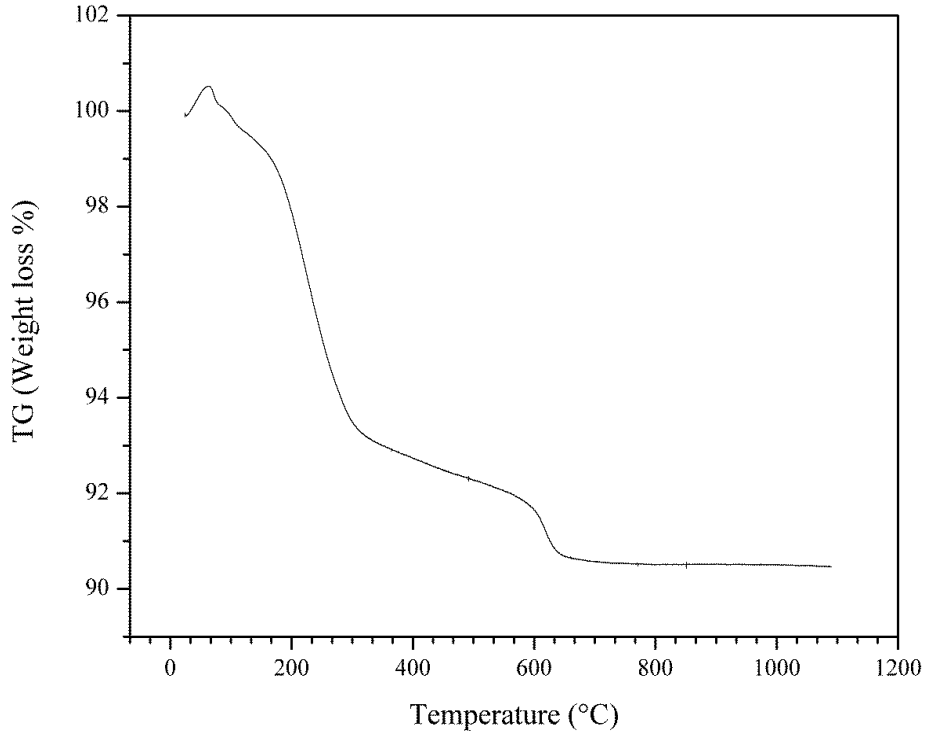


**Figure 3.13 Thermogravimetric curve of sodium titanate nanowires.**

The TGA results obtained here are in full agreement with the literature [Peng *et al.*, 2008; Shirpour *et al.*, 2013]. Dehydrated sample is stable at room temperature and do not take interlamellar water from the atmosphere.

### 3.2.5 ADT structure analysis of the final product

Automated diffraction tomography (ADT) [Kolb *et al.*, 2007, 2008] data sets were collected from six different nanowires of different dimensions (Fig. 3.14). For all acquisitions, the reconstructed 3D reciprocal volumes show more or less pronounced diffuse scattering intensities (Fig. 3.14a and c) visible as streaks exclusively along one crystallographic direction.

The two tilt series exhibiting the weakest diffuse scattering were selected for cell parameter determination and reflection intensity integration (Fig. 3.14c and d). From the selected acquisitions, a *C*-centered monoclinic cell with the parameters $a$ = 21.53 Å, $b$ = 3.79 Å, $c$ = 11.92 Å, $\beta$ = 136.3 °, V = 672 Å$^3$ was determined. Systematic extinctions due to *C*-centering were clearly identified in all reconstructed volumes. No further extinction was identified. Therefore, three space groups were taken into consideration for the structure solution: *C2*, *Cm* and *C2/m*.

The two data sets used for reflection intensity integration were collected coupling ADT with precession electron diffraction (PED) [Vincent & Midgley, 1994]. The most important parameters of the two data sets are listed in Table 3.5. The structure solution was performed *ab-initio* by direct methods as implemented in *SIR2008* [Burla *et al.*, 2007] using a fully kinematic approach ($I \sim F^2$). No correction was applied to the data.

For the first data set the structure solutions performed in space groups *C2* and *Cm* showed a clearly recognizable inversion center and were very similar to that performed in *C2/m*. Therefore, *C2/m* was chosen as the correct space group and the corresponding solution was used for further refinement.

The structure solution from the second data set basically delivered the same structural model. Imposing the space group *C2/m*, the solution obtained was very similar to that obtained with the first data set, confirming the structure model.

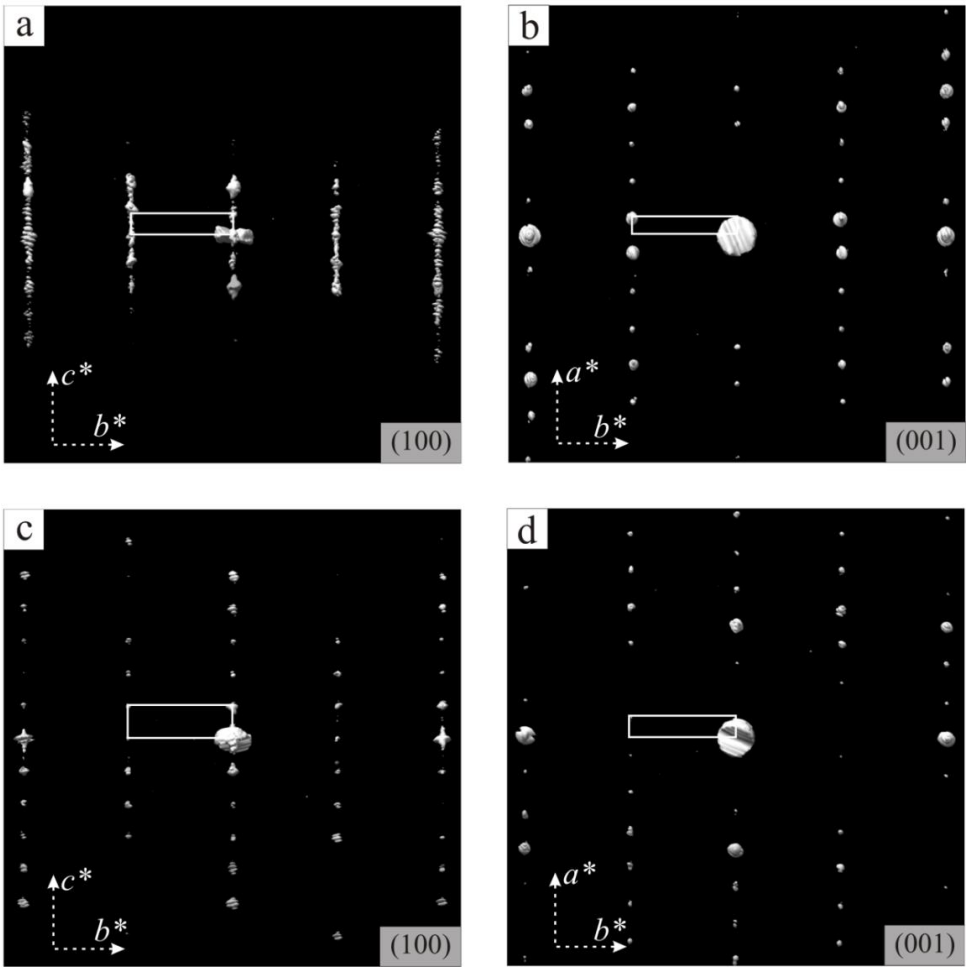


**Figure 3.14 Reconstructed three-dimensional diffraction volume obtained by ADT data from the final product.** (**a**) and (**b**) (100) and (001) projections of a strong disordered data set. (**c**) and (**d**) (100) and (001) projections of the almost ordered data set used for structure solution. In (100) projections the streaks along **c*** are evident for the first data set. In (001) projections no diffuse scattering is observed and the systematic extinctions due to the *C*-centering are well resolved.

**Table 3.5 Important experimental parameters of the ADT/PED acquisitions used for structure solution of $NaTi_3O_6(OH)\cdot 2H_2O$.** The tilt range of the second acquisition was limited by overlapping of the surrounding rods.

| **Data set** | **(I)** | **(II)** |
|---|---|---|
| tilt range (°) | -60/+60 | -45/+40 |
| no. of total reflections | 1749 | 1133 |
| no. of independent reflections | 628 | 436 |
| resolution (Å) | 0.8 | 0.8 |
| reflection coverage (%) | 79 | 58 |
| $R_{sym}$ (%) | 11.7 | 14.7 |
| overall $U$ (Å$^2$) | 0.025 | 0.032 |
| residual $R$(F) (*SIR2008*) (%) | 35.8 | 34.4 |

All maxima of the Fourier map are located on a mirror plane (y = 0.0 or 0.5). The structure consists of groups of corrugated layers of corner- and edge-sharing $TiO_n$ polyhedra arranged parallel to the (001) plane. The three strongest maxima detected in the centers of the octahedra were assigned to the Ti atoms. The remaining weaker maxima were assigned to O, Na and water molecules of crystallization.

The model was refined against electron diffraction data using *SHELXL97* [Sheldrick, 2008], without imposing any geometrical restraints (Fig. 3.15). The refinement was stable with a final $R1 = 0.267$. The assignment of $OH^-$ and the two water molecules ($O_{w1}$ and $O_{w2}$) were performed based on the interatomic distances observed, TGA results and crystal chemistry considerations. The resulting composition is therefore $NaTi_3O_6(OH)\cdot 2H_2O$.

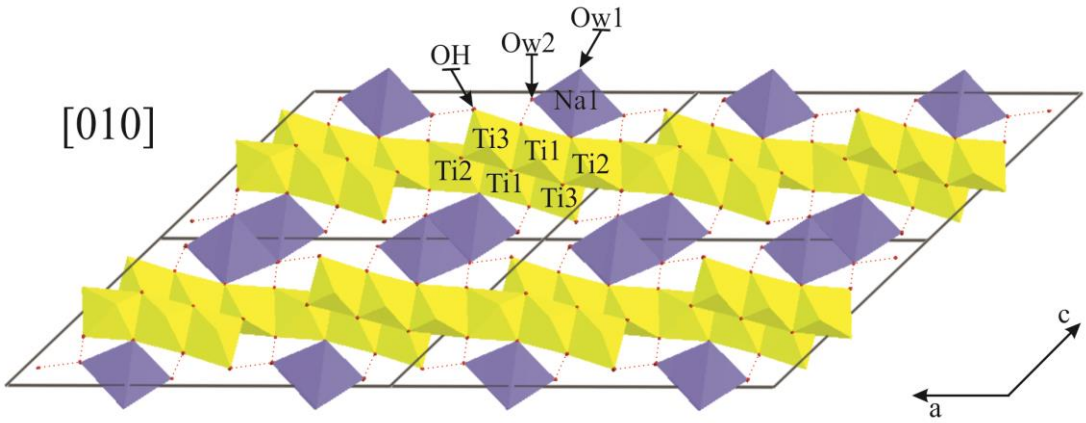


**Figure 3.15 Final model of sodium titanate $NaTi_3O_6(OH)\cdot 2H_2O$ structure** (view along [010]). Hydrogen atoms omitted for the sake of clarity. $\{NaO_6\}$ octahedral are viewed edge-on. Hydrogen bonds are drawn as dotted lines.

In order to estimate the possibility of forming hydrogen bonds, H atoms were added assuming that H(water) points to the closest and the least coordinated oxygen of the $\{Ti_3O_6(OH)\}^-$ layers ($O_{W1}\ldots O5$ 2.39 Å and $O_{W2}\ldots O2$ 2.45 Å). The H atom of the hydroxyl group, positioned on the mirror plane in the special position 4*i*, was assumed to point toward the water ($O_{W1}\ldots OH$ 2.36 Å) that lies on the same plane.

According to the proposed structure the Na:Ti ratio should be 1:3, that is higher than the experimental ratio observed by EDX of 1:2. The deviations can be ascribed to the presence of trona impurity and the possibility of $Na^+/H^+$ exchange during the manipulation of the compound [Shirpour *et al.*, 2013]. This ratio has been shown to vary with synthesis and washing procedures, as well as environmental conditions such as humidity and temperature during storage [Merceille *et al.*, 2011]. Other authors observed an unexpectedly high amount of Na for similar nanowires and correlated it with the presence of residual $Na^+$ bound to the wire surface [Nagase *et al.*, 1999; Meng *et al.*, 2004]. On the other hand, the presence of additional $Na^+$ cations between the layers cannot be excluded and may be correlated with the pervasive disorder responsible for the diffuse scattering observed in *ADT 3D* reconstructed reciprocal space.

### 3.2.6 Structure refinement against XRPD data

Despite the similarities with the above mentioned structural description [Peng *et al.*, 2008], XRPD patterns collected from this samples do not fit any crystalline phase listed in the PDF-2 database (ICDD, USA) or a plausible mixture. Due to substantial reflection profile broadening, independent indexing of the pattern was not successful. Pawley fits based on the lattice parameters derived from ADT data converges at compatible reliability factors ($R_{wp}$ = 12.7 %). Attempts to solve the structure by means of charge flipping [Coelho, 2007*b*] or direct methods implemented in *EXPO2009* [Altomare *et al.*, 2009] were not successful due to the low resolution of the data and overlapping reflections. Therefore, XRPD data were used only for the refinement of the model obtained by ADT data. Nevertheless, due to the low quality of the XRPD data, the refinement of the O positions was problematic. After applying penalty functions [Coelho & Cheary, 1997] the Rietveld refinement (Fig. 3.16) converged at $R_{wp}$ = 20.3 % and a feasible structural model close to that refined on ADT data could be achieved. All observed Bragg maxima were modelled by the fit.

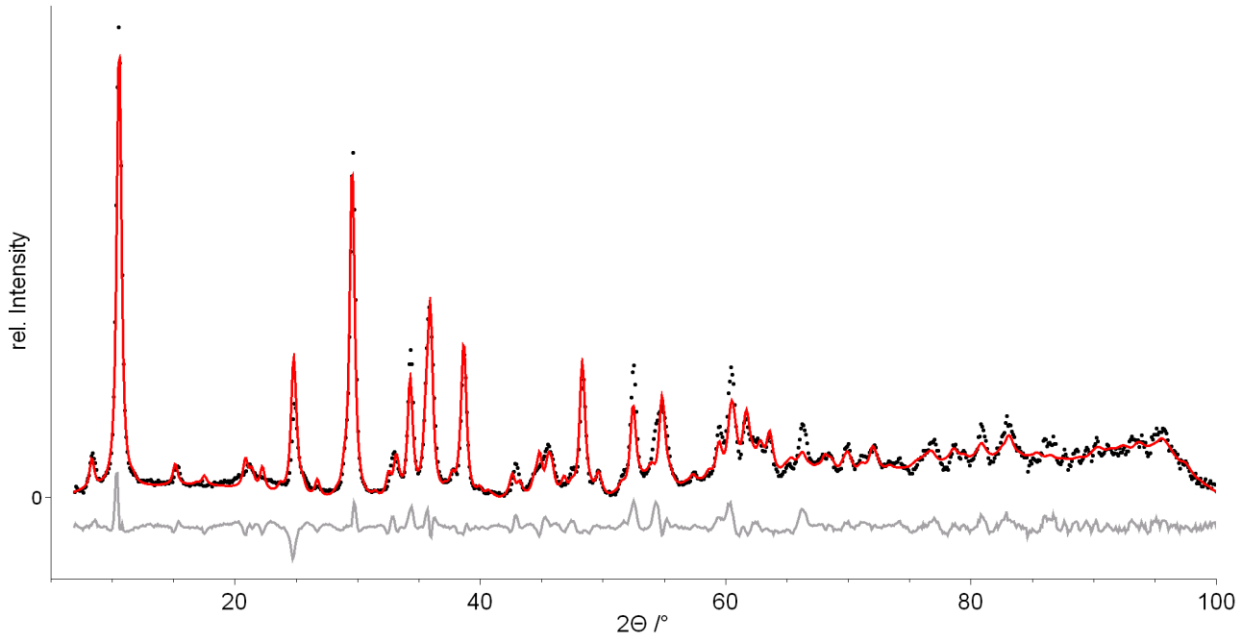


**Figure 3.16 Rietveld fit of $NaTi_3O_6(OH)\cdot 2H_2O$ structure.** Black dots: experimental data; red line: fit; grey line: difference.

## 3.3 Snapshots of calcium carbonate formation

In order to carry out a detailed step by step analysis, we prolonged the precipitation process by using DEC as a carbonate precursor (slow method). This led to a slower buildup of supersaturation in the prenucleation stage and a reduced particle growth rate in the postnucleation stage. In this setup, three different stages could clearly be discriminated (Fig. 3.17).

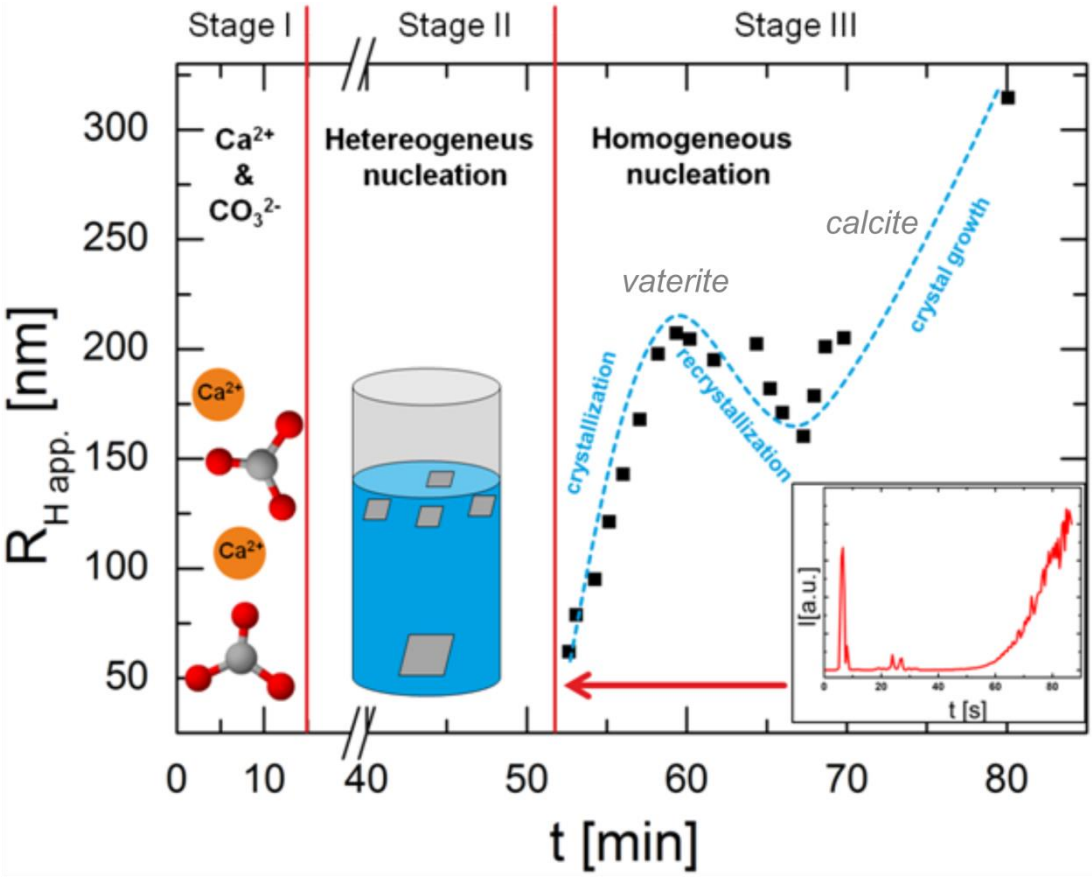


**Figure 3.17 Scheme of $CaCO_3$ precipitation (slow method).** The apparent hydrodynamic radius measured with DLS at a constant angle of $\Theta = 30°$ and $T = 20$ °C is plotted versus *t*. The red bars show the transitions between the different stages of the precipitation process. The scheme in stage II illustrates heterogeneous nucleation at the air-water interface of the DLS cuvette followed by sedimentation of the grown crystals. The inset displays the change in the scattering intensity profile during the transition from stage II (intensity spikes) to stage III (continuous intensity increase).

The first stage was characterized by the lag time necessary to produce a critical carbonate concentration to induce nucleation. TEM snapshots taken at minute 9 and the constant scattering intensity showed no evidence of particle formation at this point. At around minute 15, single particles start to form and diffuse through the scattering volume causing a reflection of the laser

beam and a spike in the scattering intensity. Evaluation of the resulting correlation function was not possible, and therefore DLS did not provide particle size information at this point. TEM snapshots taken during this second stage showed a non-homogeneous distribution of micrometer-sized calcite crystals on the grid (Fig. 3.18). Judging from the scattering intensity profile and STEM images, relatively few crystals were formed, which kept growing with time and eventually sedimented. At this point, the solution was still transparent to the naked eye but particles on the water surface could be observed. Therefore we interpret $CaCO_3$ formation during this second stage as heterogeneous nucleation at the air-water interface.

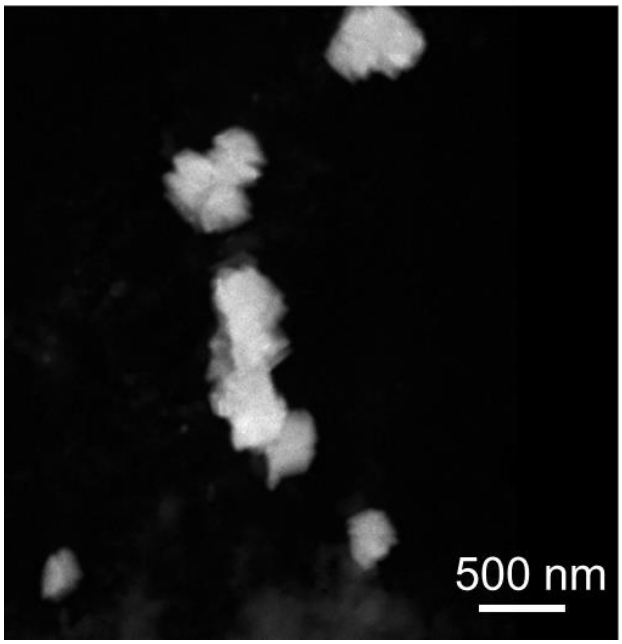


**Figure 3.18 TEM snapshot taken during the second stage of the $CaCO_3$ formation (slow method).**

After minute 52, when the carbonate concentration exceeded the critical level, a new calcium carbonate formation pathway commenced. This pathway could be discriminated from the previous one by a sharp change in the scattering intensity profile, as now a continuous and progressive increase in the scattering intensity was observed (see inset in Fig. 3.17). TEM snapshots taken at this stage showed the formation of ACC particles with sizes of about 30 nm (Fig. 3.19a) which further grow and crystallized into vaterite ( Fig. 3.19b). The formation of vaterite was eventually followed by a phase transformation to calcite *via* a dissolution and recrystallization process, starting at about 65 minutes (Fig. 3.19c). This process was indicated by a decrease and a subsequent increase in the scattering intensity, related with decrease and increase of the average size of scattering species (Fig. 3.17). The transition is most likely heterogeneous in nature, as it took place on the vaterite surface. The final stage of the experiment was governed by calcite crystal growth (Fig. 3.19d). Hence, $CaCO_3$ evolved along the pathway ACC-vaterite-calcite, in agreement with the results of other precipitation methods [Rodriguez-Blanco *et al.*, 2011].

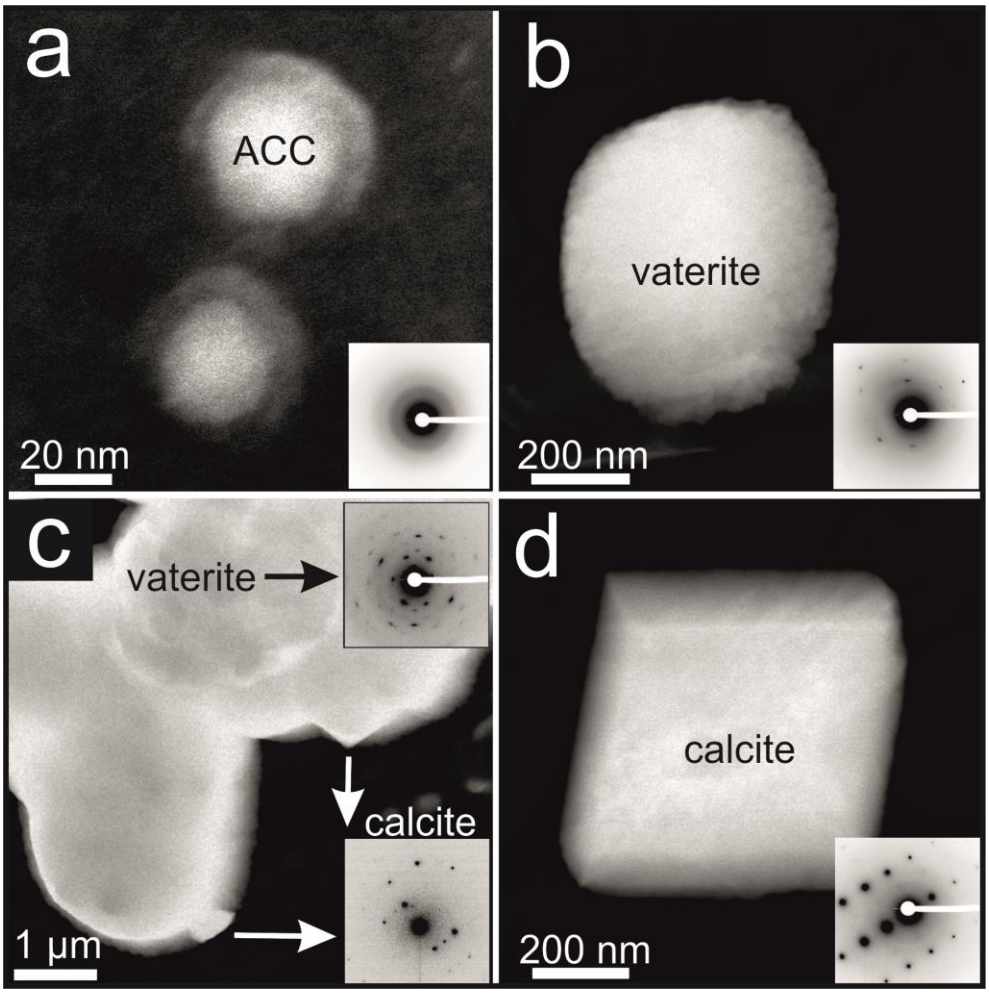


**Figure 3.19 TEM snapshots taken during the third stage of $CaCO_3$ formation (slow method).** (**a**) ACC particles observed after 52 minutes. (**b**) Aggregates of vaterite crystals observed after 62 minutes. (**c**) Vaterite aggregates and calcite single crystals observed after 65 minutes. (**d**) Single crystal of calcite observed after 70 minutes. The insets show correspondent electron diffraction patterns.

The experiment was repeated with DMC as carbonate precursor (fast method). Despite utilizing concentrations of $[Ca^{2+}]$ = [DMC] = 10 mM and [NaOH] = 8 mM, which were smaller than those in the experiment described above, the faster hydrolysis kinetics of DMC compare to DEC decreased the lag time significantly. Although the overall precipitation sequence remained the same (Fig. 3.20), the starting point of the third stage turned out to be better reproducible and took place after 17 minutes. Several quenching experiments utilizing cryo-TEM (Fig. 3.21) were carried out shortly after the point of nucleation. The earliest intermediates that could be identified unambiguously as $CaCO_3$ were 40-50 nm particles of ACC, confirming the results obtained with the slow method. Although we could not identify with certainty any earlier precipitation species, the fact that nucleation could be traced with DLS indicates that this nucleation process occurred very uniformly in solution and might serve as an additional hint for a liquid-liquid phase separation in the initial step.

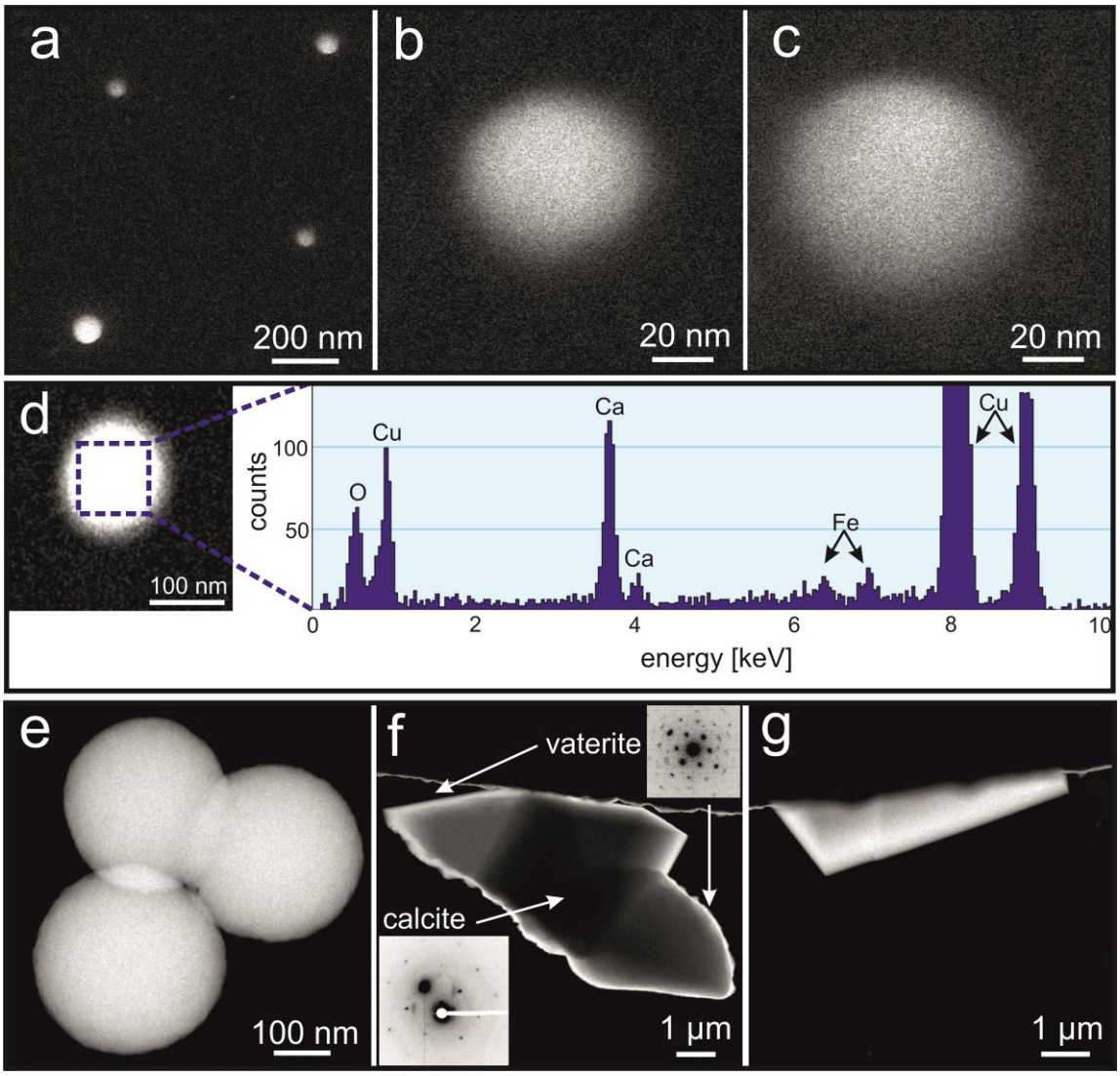


**Figure 3.20 TEM snapshots taken during the third stage of $CaCO_3$ formation (fast method).** (**a - c**) Snapshots taken directly after the beginning of stage III. The particles did not diffract. (**d**) Snapshot taken 1 minute after the beginning of stage III. EDX indicates the presence of $CaCO_3$. The Cu- and Fe-signal originate from the grid and the microscope, respectively. (**e**) ACC particles observed after 22.5 minutes. (**f**) Vaterite aggregate and calcite single crystal observed after 26 minutes. (**g**) Single crystal of calcite observed after 33.5 minutes.

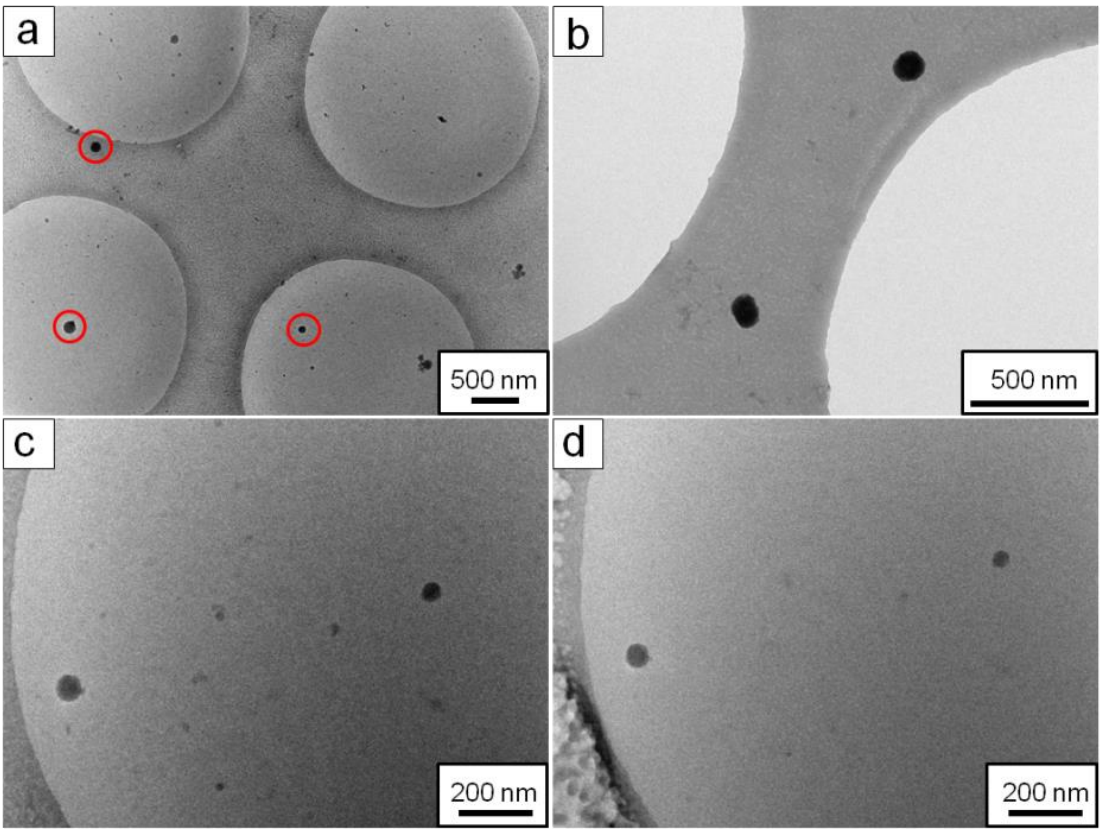


**Figure 3.21 Cryo-TEM snapshots taken 60 seconds after the beginning of third stage of the $CaCO_3$ formation (fast method).** (**a**) An overview image. The family of particles with higher contrast and sized 50-100 nm could be identified as ACC (marked with red circle). (**b**) ACC after slow unfreezing of the cryo-TEM specimen in vacuum. (**c**) and (**d**) ACC imaged in cryo-TEM is persistent after continuous exposure to the electron beam during 3 minutes.

## 3.4 Crystal structure solution of vaterite (μ-$CaCO_3$)

### 3.4.1 SEM / TEM overview

The first vaterite sample (aqueous synthesis) mainly consisted of spherical aggregates of vaterite nanocrystals with diameters of about 1 μm (Fig. 3.22a and b). Several micrometer sized crystals of calcite were present as well. After ball milling isolated single crystals of vaterite with sizes of 50 nm or less could be found isolated on the TEM grid and analyzed (Fig. 3.22c).

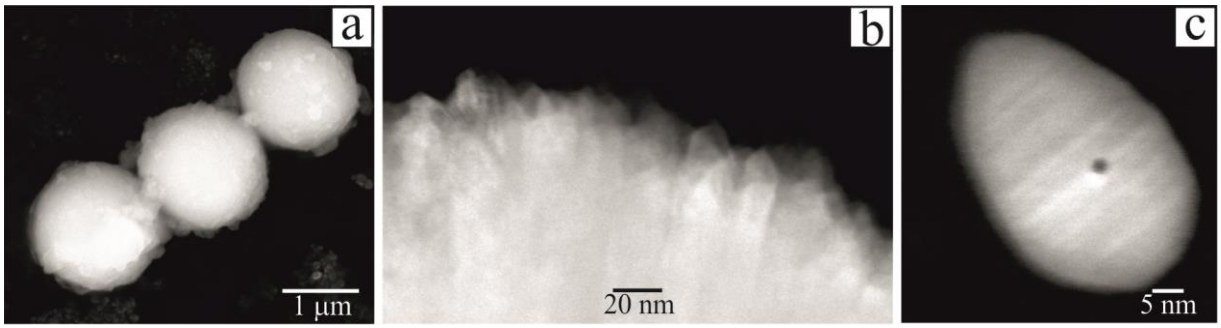


**Figure 3.22 SEM and STEM overview images of typical vaterite nanocrystals from the aqueous synthesis.** (**a**) SEM secondary-electrons image of spherical vaterite aggregates. (**b**) Dark-field STEM image of the edge of one sphere. (**c**) Dark-field STEM image of an isolated vaterite nanocrystal after ball-milling. The hole in the middle of the crystal derives from EDX analysis performed later in order to confirm the composition of the crystal.

The second vaterite sample (non-acqueous synthesis) consisted of smaller aggregates with single domain sizes of up to 70 nm (Fig. 3.23a). Usually, vaterite crystals are aggregated in clusters of tens to thousands of individuals, but it is possible to find isolated nanocrystals on the TEM grid (Fig. 3.23b). No calcite was detected in this second sample, as also expected from Raman and XRPD investigations [Schüler & Tremel, 2011].

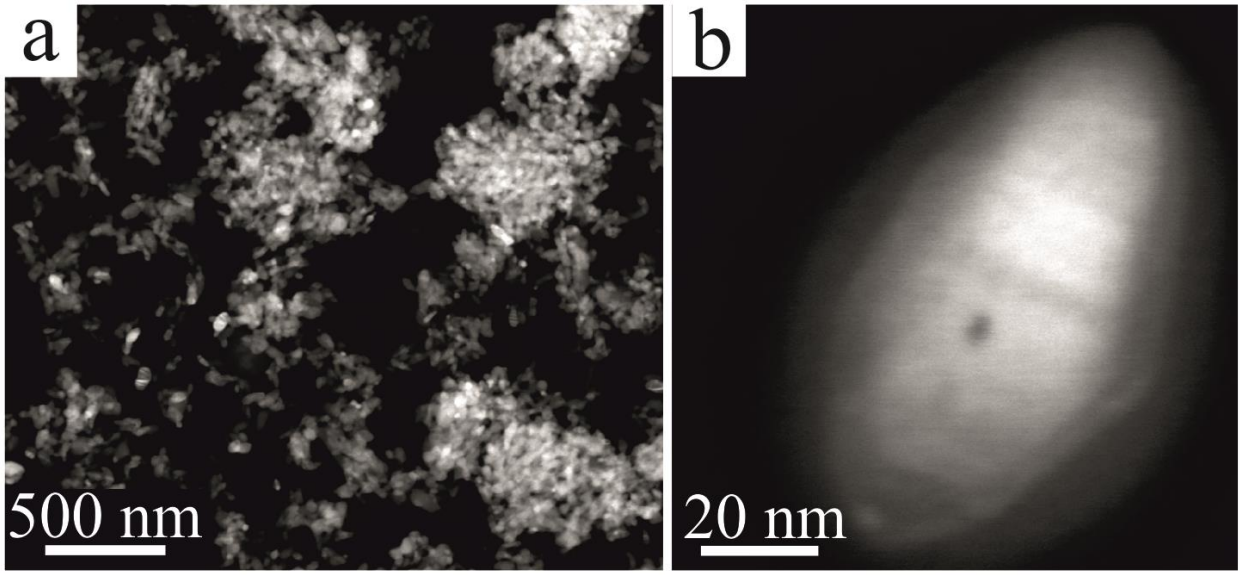


**Figure 3.23 STEM overview images of vaterite nanoparticles from non-aqueous synthesis.** (**a**) Dark-field STEM image of vaterite clusters. (**b**) Dark-field STEM image of the isolated vaterite nanocrystal. The surrounding high background is due to organic contamination accumulated during ADT acquisition, while the hole in the middle of the crystal derives from EDX analysis performed later in order to confirm the composition of the crystal.

### 3.4.2 ADT structure determination

For both samples more than 10 independent ADT data sets were collected and reconstructed in 3D diffraction volumes (Fig. 3.24).

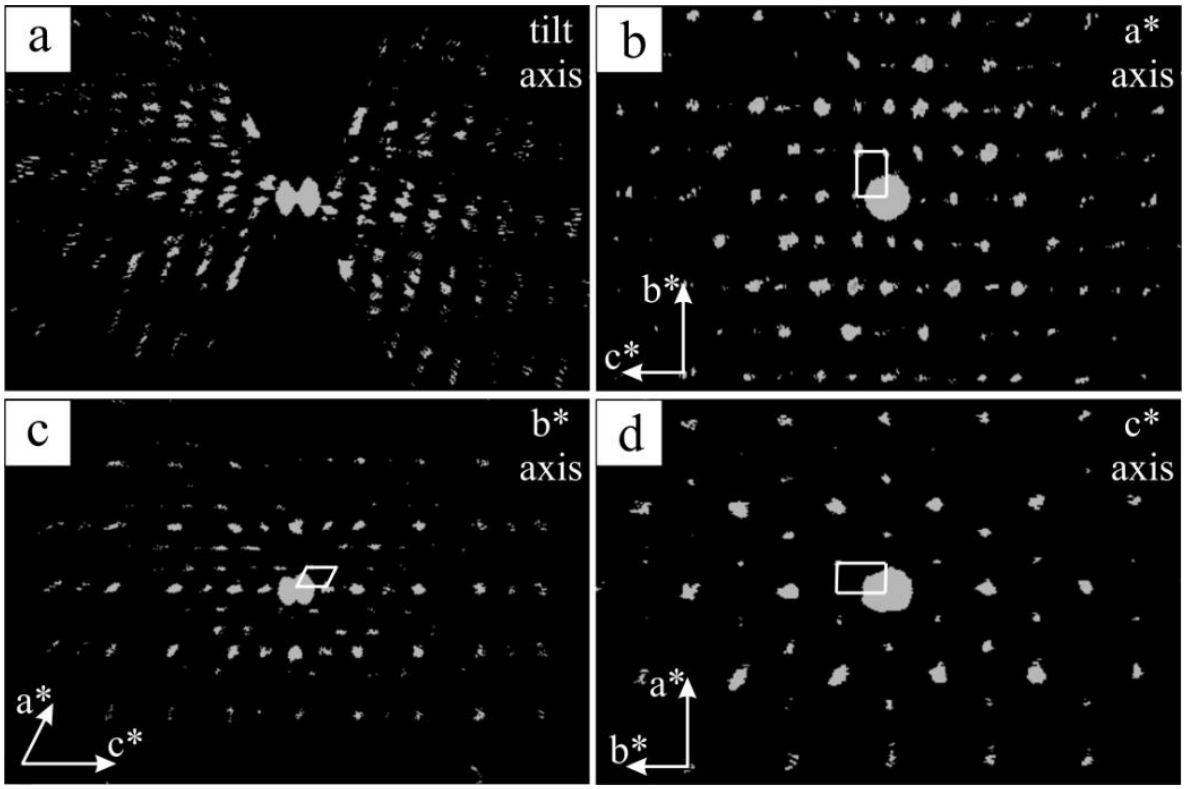


**Figure 3.24 Reconstructed three-dimentional diffraction volume obtained by ADT data from a vaterite crystal.** (**a**) View down the tilt axis. (**b**) View down **a*** axis. (**c**) View down **b*** axis. (**d**) View down **c*** axis. Note that these are projections of a 3D diffraction volume and not 2D oriented diffraction patterns.

All the volumes delivered a monoclinic cell with parameters $a$ = 12.17 Å, $b$ = 7.12 Å, $c$ = 9.47 Å, $\beta$ = 118.948°. As for the models reported in literature, this cell is a geometric transformation of the smallest hexagonal cell proposed by Kamhi [Kamhi, 1963]. The cell transformations from the previous models to the cell derived by ADT data are shown in Figure 3.25 and reported in Table 3.6. Systematic extinctions due to *C*-centering are detectable down **c*** axis (Fig. 3.24d), while down **a*** extinctions due to a *c*-glide plane orthogonal to **b** can be recognized (Fig. 3.24b) despite the presence of residual dynamical scattering. Finally, looking down **b*** it becomes evident that general reflections (*hkl*) with $h \neq 3N$ are very weak and characterized by diffuse scattering along **c***(Fig. 3.24c).

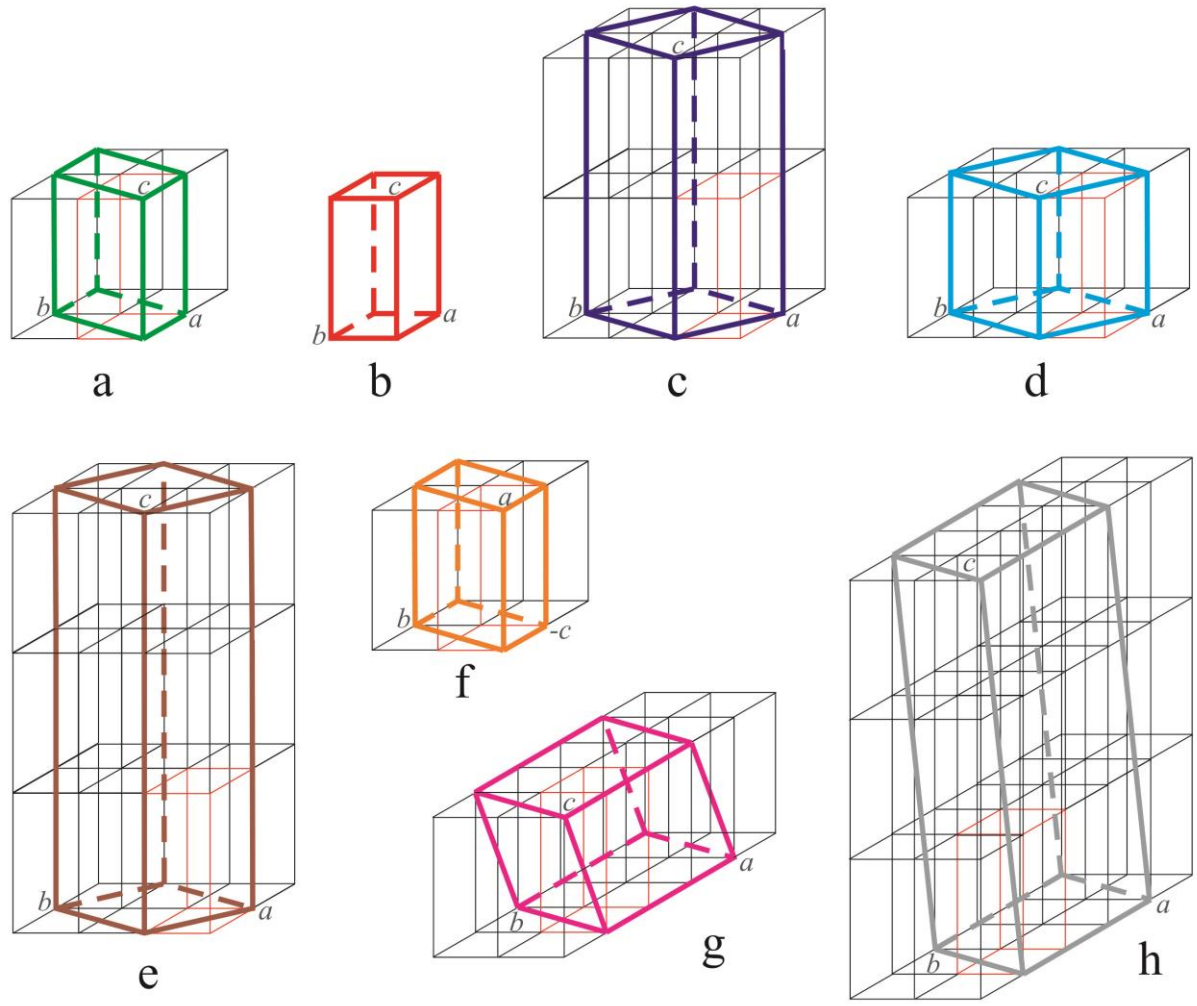


**Figure 3.25 Comparison of different vaterite cells**. (**a**) Meyer´s experimental model [Meyer, 1959]. (**b**) Kamhi´s experimental model [Kamhi, 1963]. (**c**) Meyer´s revised experimental model [Meyer, 1969]. (**d**) Lippman´s experimental model [Lippman, 1973]. (**e**) Wang´s & Becker´s theoretical model [Wang & Becker, 2009]. (**f**) le Bail's *et al.* experimental model [le Bail *et al.*, 2011]. (**g**) Monoclinic cell proposed on the basis of three-dimensional ADT data. (**h**) Anorthic modulated cell. All unit cells are geometrically related to the smallest hexagonal cell proposed by Kamhi [Kamhi, 1963] (in red).

**Table 3.6 Cell transformation matrixes between previous proposed and actual monoclinic vaterite cells.**

| **Previous model** | $a_{11}$ | $a_{12}$ | $a_{13}$ | $a_{21}$ | $a_{22}$ | $a_{23}$ | $a_{31}$ | $a_{32}$ | $a_{33}$ |
|---|---|---|---|---|---|---|---|---|---|
| From Meyer, 1959 | 3 | 0 | 0 | 0 | 1 | 0 | $\bar{1}$ | 0 | 1 |
| From Kamhi, 1963 | 3 | 0 | 0 | 1 | 2 | 0 | $\bar{1}$ | 0 | 1 |
| From Meyer, 1969 | 2 | 1 | 0 | 0 | 1 | 0 | $\bar{2}/3$ | $\bar{1}/3$ | $1/2$ |
| From Lippman, 1973 | 2 | 1 | 0 | 0 | 1 | 0 | $\bar{2}/3$ | $\bar{1}/3$ | 1 |
| From Wang & Becker, 2009 | 2 | 1 | 0 | 0 | 1 | 0 | $\bar{2}/3$ | $\bar{1}/3$ | $1/3$ |
| From le Bail *et al.*, 2011 | 0 | 0 | $\bar{3}$ | 0 | 1 | 0 | 1 | 0 | 1 |

The structure was determined independently from three ADT/PED electron diffraction data sets collected in tilt ranges of ±60° and 1° steps. The most important experimental parameters are listed in Table 3.7.

**Table 3.7 Important experimental parameters of the ADT/PED acquisitions used for vaterite structure determination.**

| **Data set** | **(I)** | **(II)** | **(III)** |
|---|---|---|---|
| Synthesis | aqueous | non-aqueous | non-aqueous |
| tilt range (°) | -60/+60 | -60/+60 | -60/+60 |
| no. of total reflections | 1844 | 2592 | 1490 |
| no. of independent reflections | 416 | 575 | 427 |
| resolution (Å) | 0.9 | 0.8 | 0.9 |
| reflection coverage (%) | 80 | 77 | 83 |
| $R_{sym}$ (%) | 16.0 | 20.0 | 15.0 |
| overall $U$ (Å$^2$) | 0.037 | 0.040 | 0.032 |
| residual $R$(F) (*SIR2008*) (%) | 34.0 | 41.0 | 32.0 |

Structure solution was performed *ab-initio* by direct methods implemented in the program *SIR2008* [Burla, 2007] assuming the kinematic approximation – i.e. neglecting dynamical effects. In all three cases the structure solution converged to the same structure model in space group *C2/c*, Z=12. The strongest 9 maxima in the potential map correspond to the 9 independent atoms

of the structure and remaining maxima are negligible. Least-square refinement was performed with *SHELXL97* [Sheldrick, 2008] imposing flat $\{CO_3\}^{2-}$ groups and restraints of 1.28 Å on C-O distances and 2.22 Å on O-O distances. The final configuration, obtained after 30 cycles of refinement, was close to the structure obtained by direct methods. Atomic positions where stable and all atomic thermal factors $u$ were in the reliable range of 0.036–0.101 $Å^2$. The residual $R1(4\sigma)$ was 37.76%, a high value when compared with residuals of structure solutions from standard X-ray diffraction data, but inside the expected range for electron diffraction refinements based on kinematic theory [Weirich, 2001; Klein, 2011]. The correctness of the structure was assumed on the basis of the reproducibility and stability of the refinement. Figure 3.26 shows the final model along projections [010] and [103].

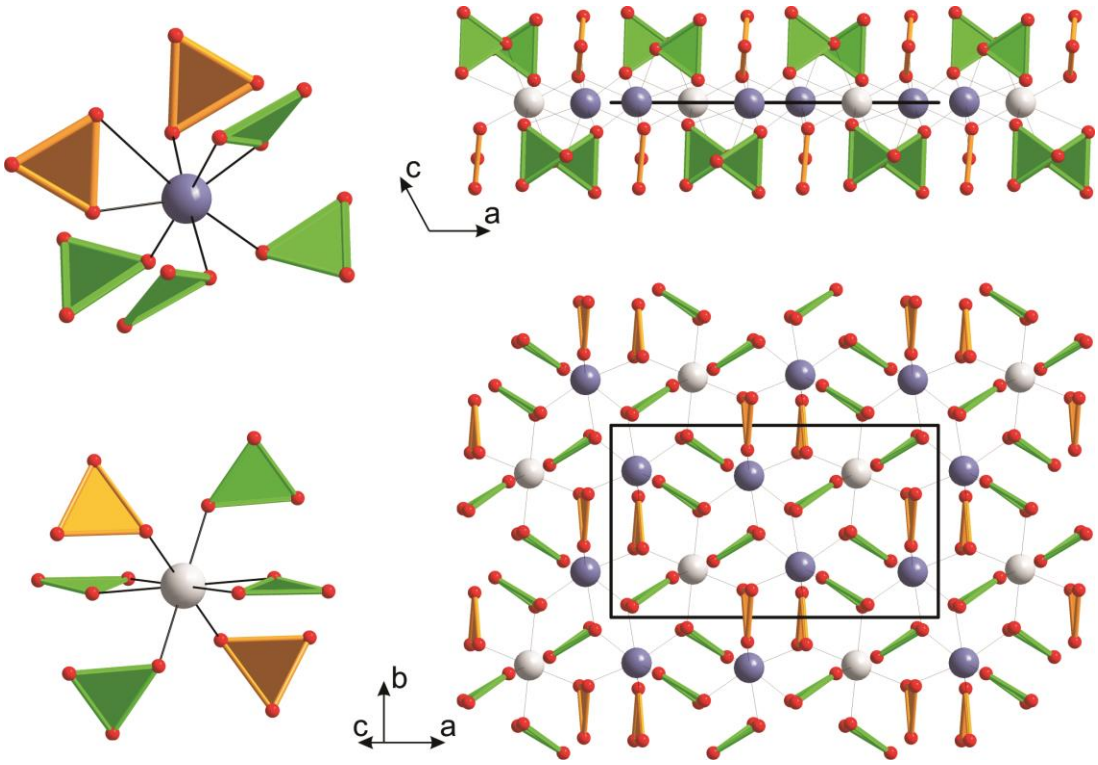


**Figure 3.26 Final 2-layer model of vaterite crystal structure.** Left: coordination of the $Ca^{2+}$ ions (light gray: Ca(1), blue: Ca(2)) by the oxygen atoms of the two different carbonate groups (orange: $CO_3^{2-}$(1), green: $CO_3^{2-}$(2)). Right: views down [010] and [103] (equivalent to [001] in the previous hexagonal structure models) illustrating the layer type structure and the pseudo-hexagonal arrangement of the $Ca^{2+}$ ions.

### 3.4.3 Stacking disorder and modulation

A closer inspection of the 3D reconstructed diffraction volume shows diffuse scattering along **c*** (Fig. 3.24c). Additionally, single oriented diffraction patterns collected along [010] reveal that general reflections (*hkl*) with $h \neq 3N$ exhibit a small non-rational shift along **c*** of around $0.17 \cdot |\mathbf{c^*}|$ (Fig. 3.27a). Nevertheless, the accurate measurement of this shift is hampered by the presence of diffuse scattering and extra-periodicities. The main periodicity is 0.83 nm (equivalent

to $d_{001}$), but longer periodicities of 6, 12, and 16 nm (namely in the same order of magnitude of the crystal size) are also recognizable (Fig. 3.27b). HRTEM images (Fig. 3.28a and b) confirm the presence of a long-range stacking fault type disorder along the **c*** direction, which locally can generate ordered modulated sequences.

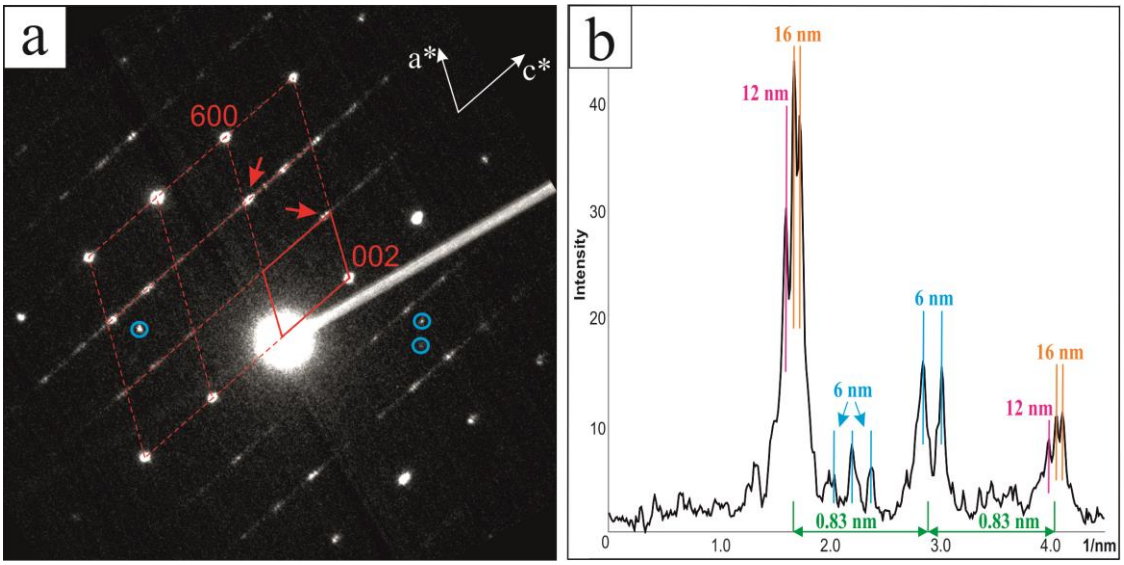


**Figure 3.27 Diffuse scattering and local modulation along c* in vaterite structure (NED observation).** (**a**) In-zone [010] nano electron diffraction (NED) patterns. The doubled reciprocal vectors are shown. Reflections (*hkl*) with $h \neq 3N$ show diffuse scattering and a systematic small shift along c* (marked with red arrows). Three foreign reflections are marked with blue circles. (**b**) Intensity profile taken along the 40*l* diffraction line, showing a main periodicity of 0.83 nm and other longer periodicities up to 16 nm.

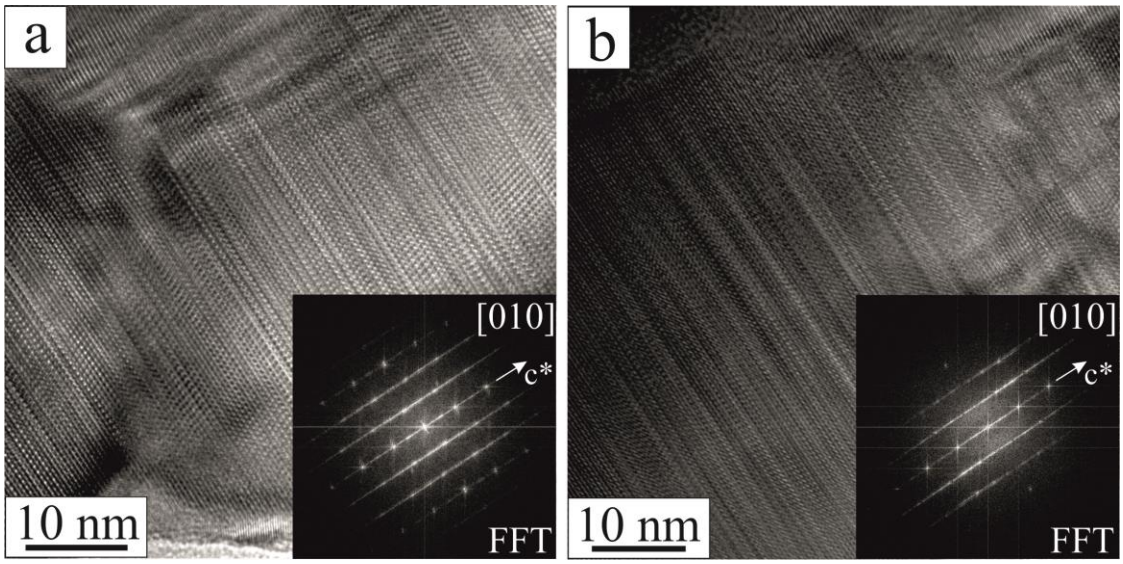


**Figure 3.28 Diffuse scattering and local modulation along c* in vaterite structure (HRTEM confirmation).** (**a**) HRTEM image down [010] and related fast Fourier transform (FFT) showing disorder and local modulation along the **c*** direction. (**b**) HRTEM image down [010] and relative FFT showing a more disordered vaterite nanocrystal.

An exhaustive incommensurate structure analysis of vaterite is hampered by diffuse scattering, extra periodicities and fast deterioration of the material under HRTEM conditions. At present, ADT data analysis is not able to provide conclusive quantitative information about disorder and incommensurate modulation even for larger domains and more stable phases. [Andrusenko *et al.*, 2011; Palatinus *et al.*, 2011] In order to understand the structural implication of the reflection shift along **c***, a larger cell with triple *c*-periodicity was defined (Fig. 3.29a). This setting is a close approximation of the postulated incommensurate modulation. The resulting cell parameters are: $a$ = 12.17 Å, $b$ = 7.12 Å, $c$ = 25.32 Å, $\alpha$ = 90.008°, $\beta$ = 99.228°, $\gamma$ = 90.008° (Fig. 3.29b).

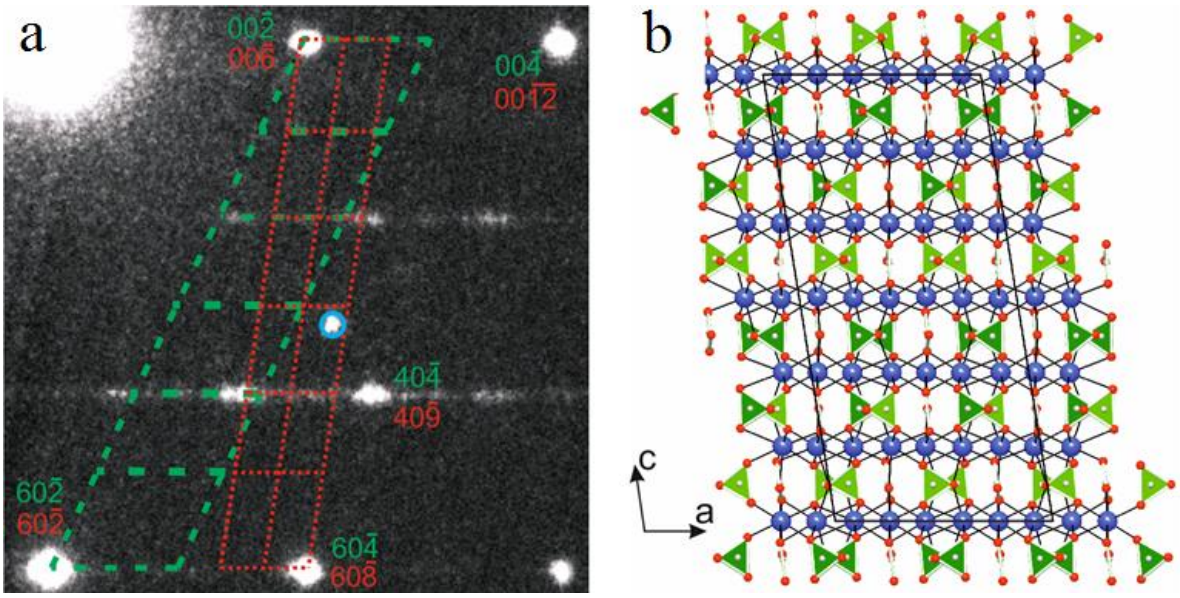


**Figure 3.29 Final 6-layer model of vaterite crystal structure.** (**a**) Section of a [010] diffraction pattern with a 2-layer monoclinic cell (green) and 6-layer triclinic cell (red) superimposed. Exemplary reflections are indexed according to both cells. 10l and 30l lines are extinguished because of the *C*-centering. One foreign reflection is marked with blue circles. (**b**) [010] projection of the 6-layer model (blue: Ca, gray: C, red: O). The stacking vector is shown in black.

Intensities were extracted from the best electron diffraction volume (ADT data set III), collected on a nanoparticle obtained by the non-aqueous synthesis. The structure was solved *ab-initio* by direct methods in the triclinic space group $C\bar{1}$. It is worth to point out that 45 of the 46 independent atoms of the structure were automatically localized within the first 48 peaks of the potential map, although most of them were light atoms as oxygen and carbon. The structure was subsequently refined imposing geometrical restraints on the $\{CO_3\}^{2-}$ groups. The structure is very similar to the 2-layer monoclinic model described above with the same basic motif of $Ca^{2+}$ layers connected by orthogonal $\{CO_3\}^{2-}$ groups (Fig. 3.30). The local atom coordination is preserved, the main difference is that the stacking rule along **c** changes from the simple sequence (+,+,…) to a sequence (+,+,-,+,+,-,…), where + and – respectively a shift of +1/3**a** and –1/3**a** every two anion layers.

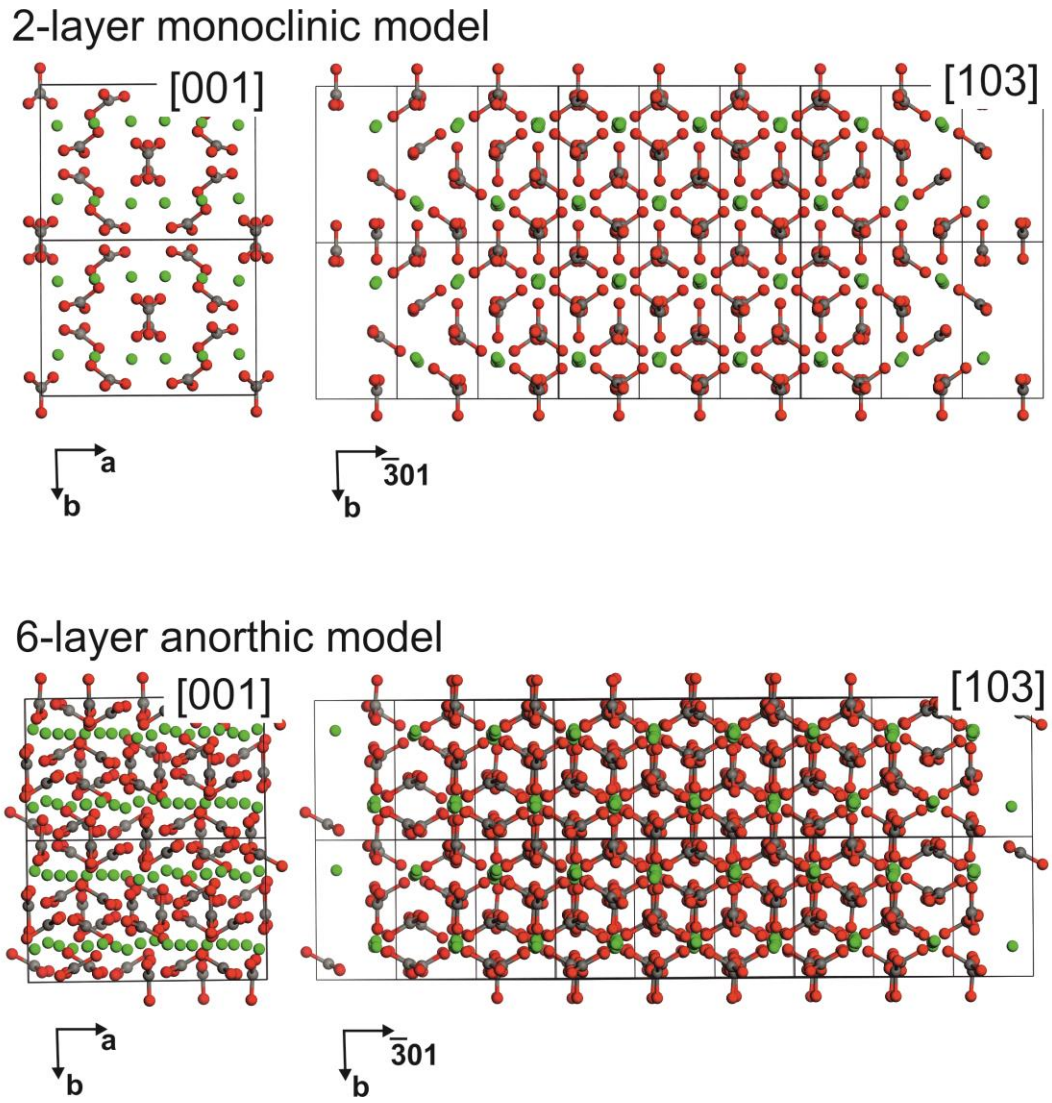


**Figure 3.30 Selected projections of vaterite 2-layer and 6-layer models.** Ca atoms are shown in green, C in grey, O in red. Note the pseudo-hexagonal symmetry when the structure is oriented along the [103] projection.

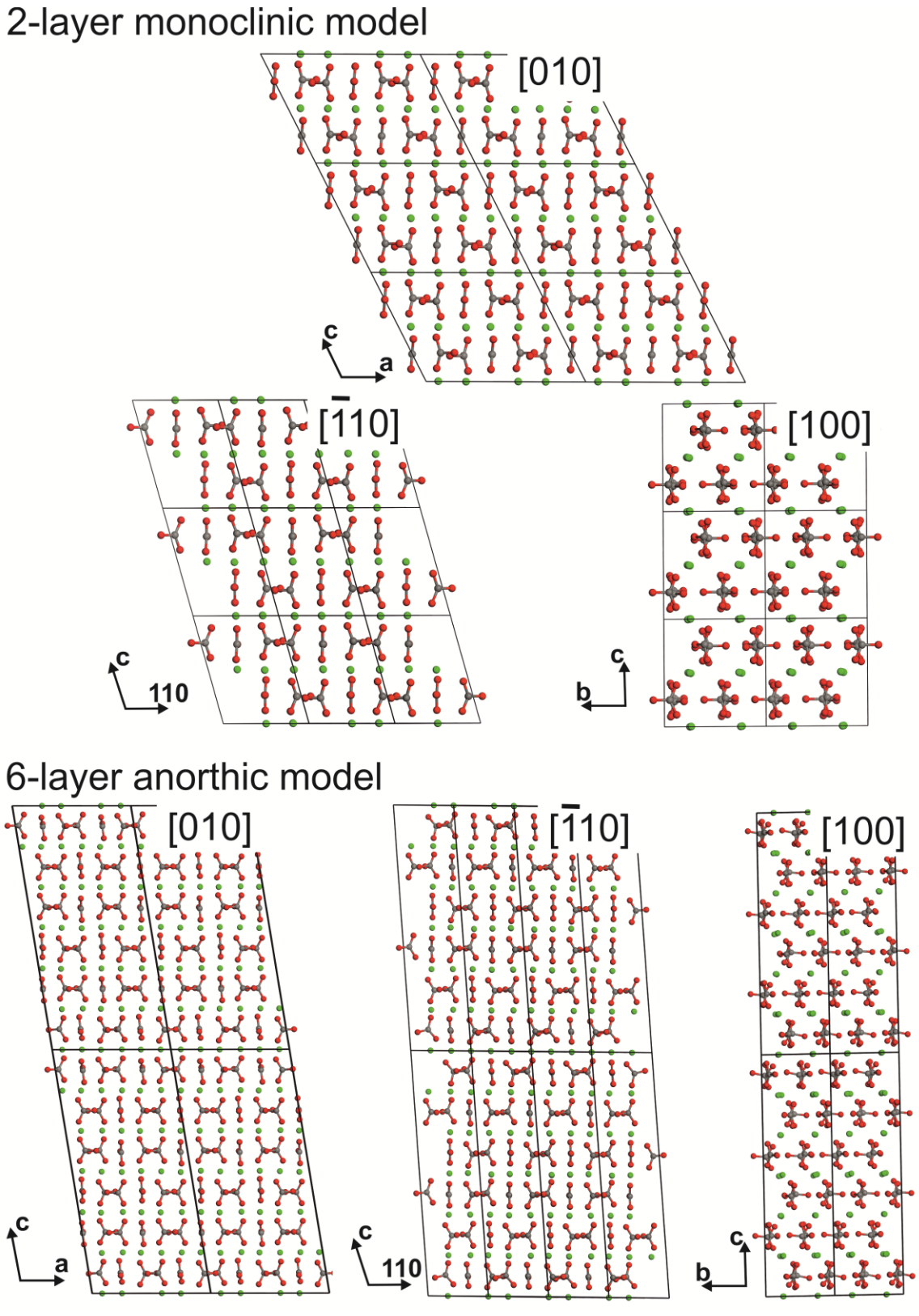


**Figure 3.30** Continues from previous page.

### 3.4.4 Structure refinement against XRPD data

Due to the low scattering power of carbon and oxygen only the background parameters, cell parameters, crystallite sizes, one overall displacement parameter and the positional parameters of the calcium atoms were refined. Compared with previous acquisitions, these data have the advantage of being collected on a pure vaterite sample without calcite impurities. Rietveld refinement based on the 2-layer monoclinic model showed a moderately good fit but converged at relatively high residuals even for nanocrystalline samples (Fig. 3.31a). In particular the scattering maxima at $Q \approx 27.5$ nm$^{-1}$ and $Q \approx 37.4$ nm$^{-1}$ were not modelled correctly. In contrast, the Rietveld refinement based on the triclinic 6-layer superstructure converged at lower residuals and allowed a better fit of the diffractogram features (Fig. 3.31b). Selected experimental details are given in Table 3.8.

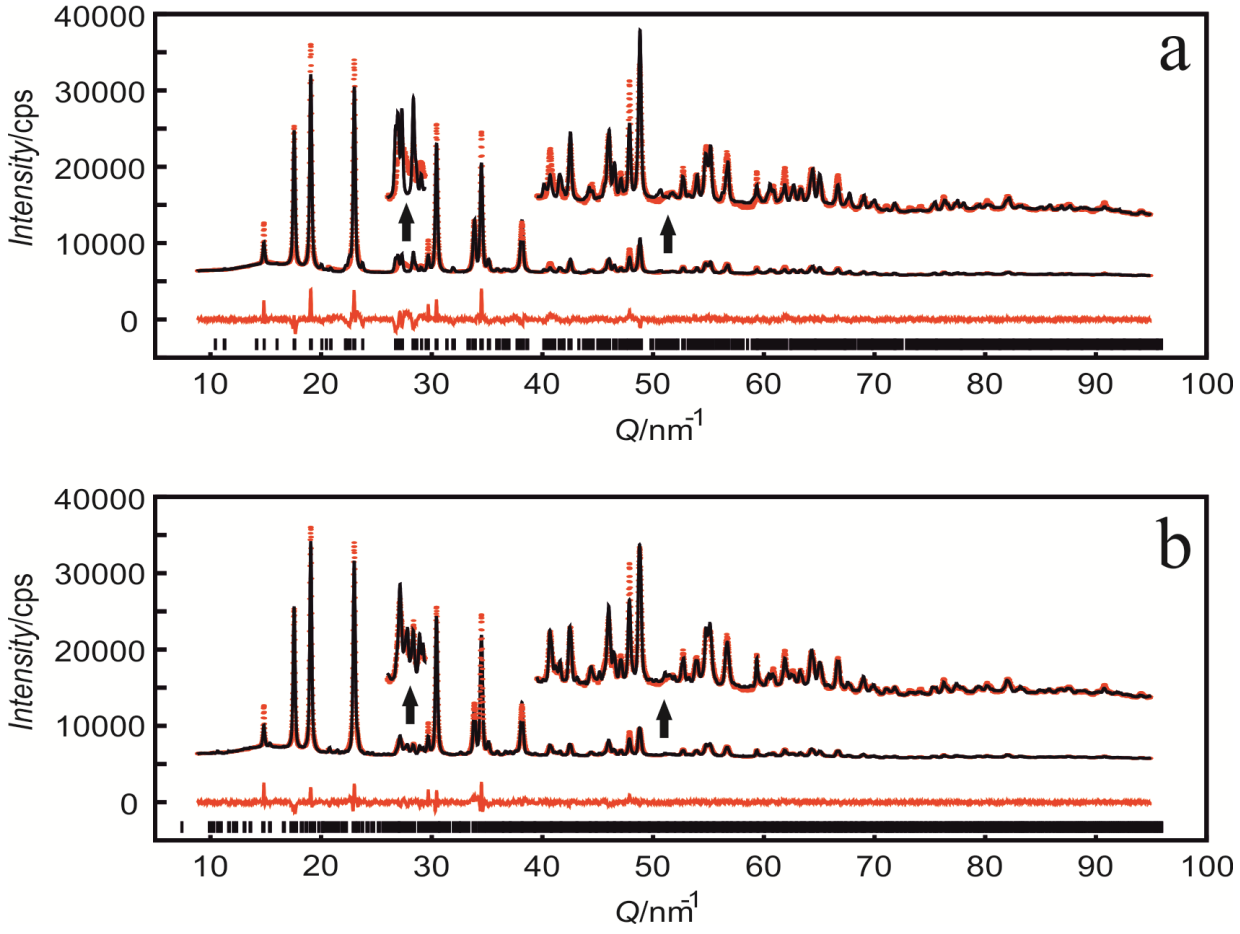


**Figure 3.31 Structure refinement of vaterite 2-layer and 6-layer models against XRPD data.** (**a**) Rietveld refinement (black line) of synchrotron data (red dots) and difference (red line) for the 2-layer monoclinic model. (**b**) Rietveld refinement for the 6-layer triclinic model. cps = counts per second.

**Table 3.8 Selected crystallographic information and experimental details for the Rietveld refinement of vaterite 2-layer and 6-layer models.**

| **Refined structure** | **2-layer monoclinic model** | **6-layer triclinic model** |
|---|---|---|
| ***Crystallographic information*** | | |
| space group | *C2/c* | *P-1* |
| *a* (Å) | 12.408(1) | 7.1668(4) |
| *b* (Å) | 7.1372(5) | 7.1340(4) |
| *c* (Å) | 9.4067(5) | 25.7210(8) |
| $\alpha$ (°) | 90.0 | 82.305(4) |
| $\beta$ (°) | 115.852(5) | 90.254(4) |
| $\gamma$ (°) | 90.0 | 59.966(5) |
| V (Å$^3$) | 748.68(9) | 1125.3(1) |
| $B_{iso}$ (Å$^2$) | 2.29(3) | 1.61(2) |
| ***Experimental details*** | | |
| 2$\Theta$ range (°) | 1-60 | |
| $\Delta$2$\Theta$ step (°) | 0.005 | |
| $R_p$ (%) | 7.77 | 5.21 |
| $R_{wp}$ (%) | 10.44 | 6.41 |
| $R_{exp}$ (%) | 1.98 | 1.98 |
| GoF | 5.274 | 3.246 |
| no. of parameters | 33 | 54 |

# Chapter IV Discussion

## 4.1 Ternary oxide system $M_2O$-$Al_2O_3$-$WO_3$ ($M$ = Na, K)

### 4.1.1 Structure relations with other phases in the $M_2O$-$Al_2O_3$-$WO_3$ system

***$K_5Al(W_3O_{11})_2$***

$K_5Al(W_3O_{11})_2$ is structurally related with $KW_3O_9$ [Klug, 1977] and $K_2W_3O_{10}$ [Okada *et al.*, 1976] (Fig. 4.1). $KW_3O_9$ orthorhombic structure (Fig. 4.2a) is made of building unit of 5·($WO_6$-octahedra). Such building units compose flat layers parallel to (001). All the octahedra connect to other octahedra by vertexes and $K^+$ ions are confined inside mono-dimensional channels defined by 6-octahedra rings.

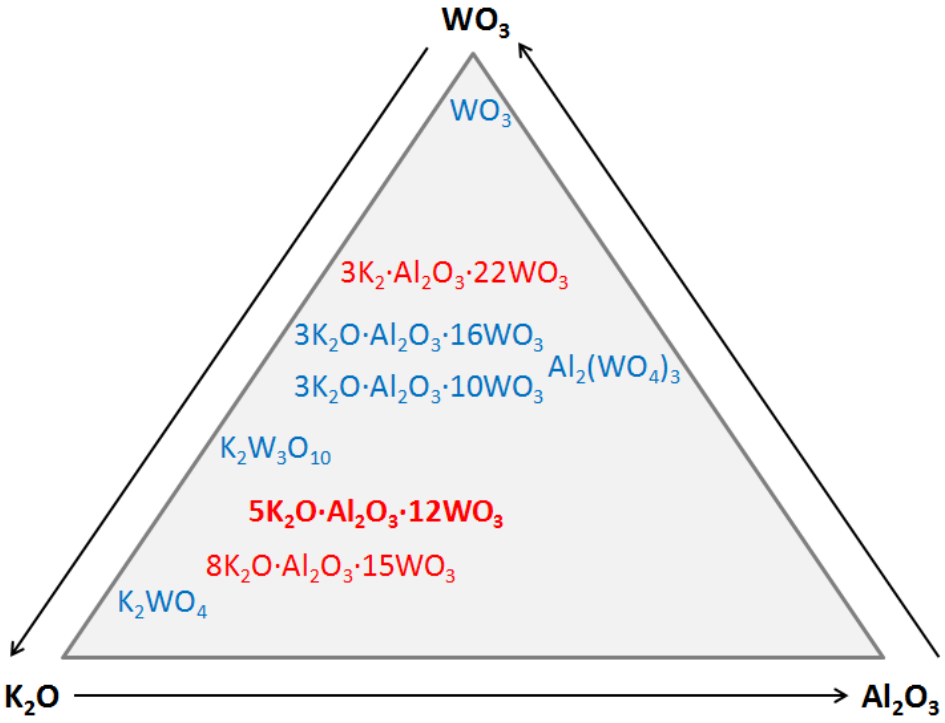


**Figure 4.1 Phase diagram of $K_2O$-$Al_2O_3$-$WO_3$ system.** Six known phases are in blue. Three unknknown phases are in red. In bold is indicated the structure that was solved during this study.

The addition of K up to a composition of $K_2W_3O_{10}$ has the effect of reducing the density of the structure (Fig. 4.2b). The 5·($WO_6$-octahedra) building units are still recognizable, but now they form two-dimensional bands connected by 4·($WO_6$-octahedra) linker. While octahedra in the building unit are connected by vertexes, octahedra in the linker are connected by edges. $K^+$ ions are confined inside mono-dimensional "channels" that stretch along (10-3) and give the structure a certain degree of cleavage. The angle $\beta$ (analogous to $\gamma$ in $KW_3O_9$) is 108.44°, and symmetry drops to monoclinic *P2/c*.

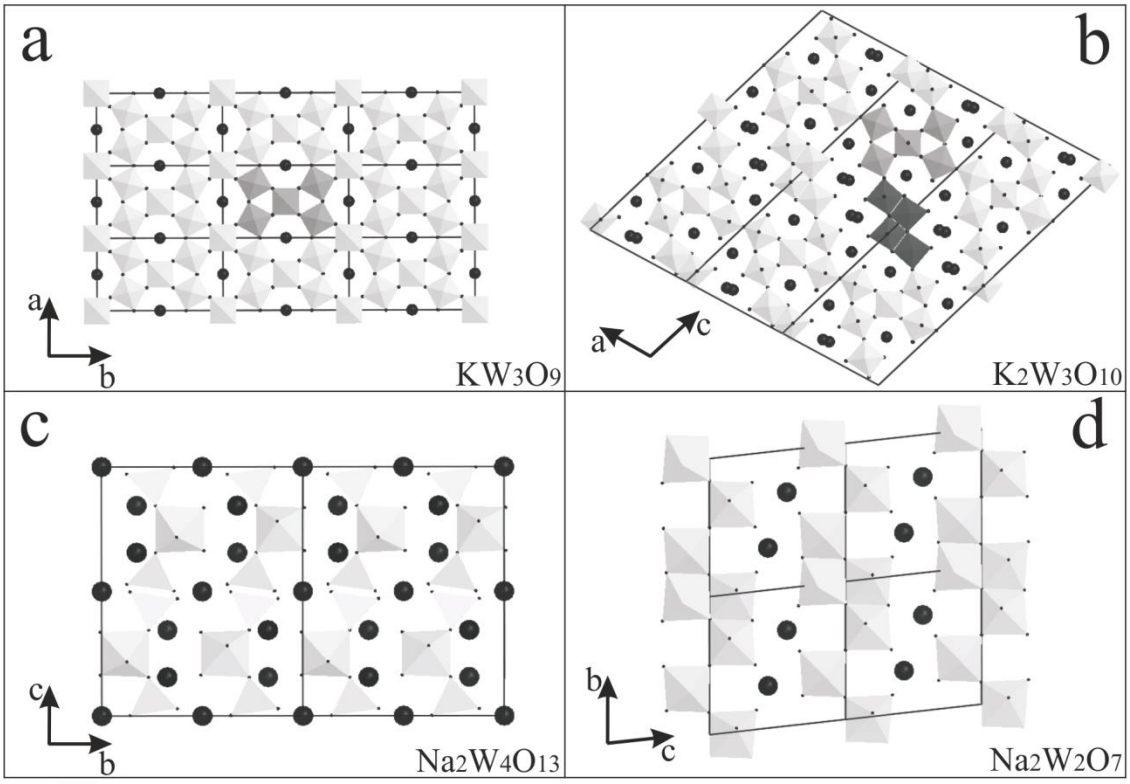


**Figure 4.2 Structurally related phases in the $M_2O$-$Al_2O_3$-$WO_3$ system.** $WO_6$-octahedra and $WO_4$-tetrahedra are shown in light grey, K and Na in black. (**a**) $KW_3O_9$ viewed along [001], with one of the 5·($WO_6$-octahedra) building units highlighted in dark grey. (**b**) $K_2W_3O_{10}$ viewed along [010], with a 5·($WO_6$-octahedra) building units and a 4·($WO_6$-linker) highlighted in dark grey. (**c**) $Na_2W_4O_{13}$ viewed along [100]. (**d**) $Na_2W_2O_7$ viewed along [100].

The addition of more K and Al up to $K_5Al(W_3O_{11})_2$ reduces further the coordination of W atoms, that now are all 5-coordinated in square pyramids, connected either by vertexes or edges. The 5·($WO_6$-octahedra) units twist in spirals where two (over five) W atoms are substituted by $K^+$ ions. The main effect of such substitution is a doubling of the cell parameter **b**. The $WO_6$-octahedra linkers are replaced by vertex-connected $AlO_4$-tetrahedra. Layers of $K^+$ ions cut the structure in two-dimensional planes, along which the pseudo glide-plane is located. The marked cleavage favors stacking disorder, as evidenced by the diffuse scattering along **c***. The cell of $K_5Al(W_3O_{11})_2$ can be deduced from the cell of $K_2W_3O_{10}$ applying the transformation:

$$\begin{bmatrix} 1 & 0 & 1/4 \\ 0 & 2 & 0 \\ -2 & 0 & 1/2 \end{bmatrix}$$

***$NaAl(WO_4)_2$ – phase II***

$NaAl(WO_4)_2$ structure consists of layers of $AlO_6$-octahedra and $WO_4$-tetrahedra, intercalated by layers of $Na^+$ ions. Establishing structural connections between this phase and other phases of the

$Na_2O$-$Al_2O_3$-$WO_3$ system is not trivial, as most of the closest members are structurally unknown (Fig. 4.3). The two known structures $Na_2W_4O_{13}$ [Viswanathan, 1974; Gorelik *et al.*, 2011] and $Na_2W_2O_7$ [Okada *et al.*, 1975] are layered with $WO_6$-octahedra and $WO_4$-tetrahedra bands interconnected by $Na^+$ ions (Fig. 4.2c and d). The fact that $Na_2W_2O_7$ is closely related to $NaAl(WO_4)_2$ is evident when the octahedrally coordinated W is replaced by Al and the respective **a** and **b** vectors are exchanged.

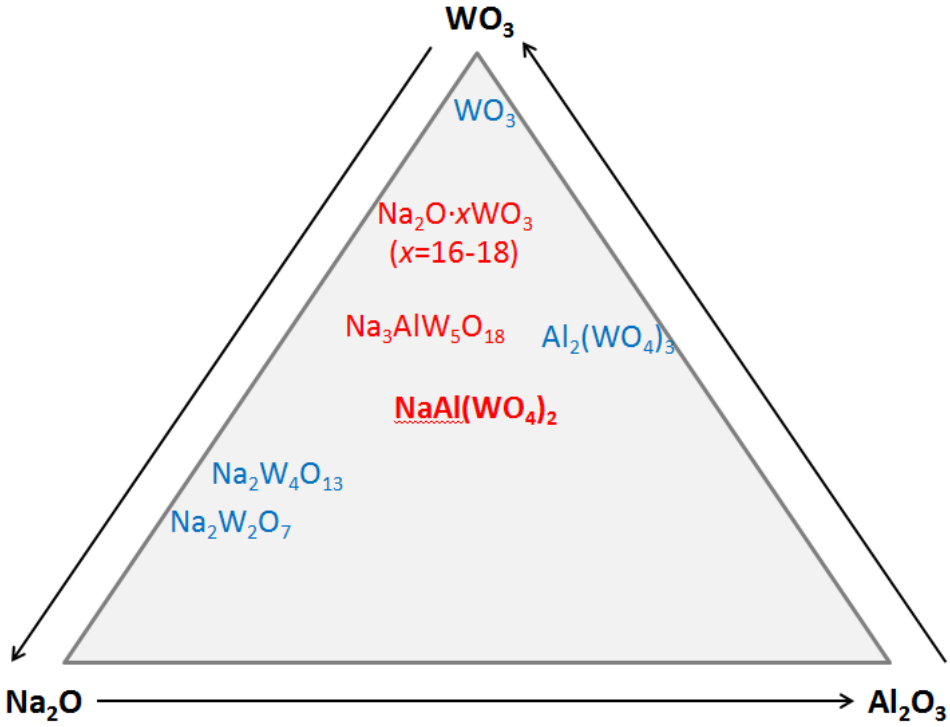


**Figure 4.3 Phase diagram of $Na_2O$-$Al_2O_3$-$WO_3$ system.** Four known phases are in blue. Three unknknown phases are in red. In bold is indicated the structure that was solved during this study.

### 4.1.2 Pseudo-symmetries of $M_2O$-$Al_2O_3$-$WO_3$ system

All structures investigated in $K_2O$-$Al_2O_3$-$WO_3$ and $Na_2O$-$Al_2O_3$-$WO_3$ samples were found to be affected by pseudo-symmetries, which actually concurred in complicating any structure solution based on mono-dimensional X-ray powder diffraction data (XRPD). In such cases even optimal, synchrotron-acquired XRPD data could be not successful for the structure characterization of the material. Previous attempts of structure solution of $K_5Al(W_3O_{11})_2$ based on XRPD failed due to the incorrect space group assignment, misled by the weak reflections *hk*0 with $h$ = 1, 3, 5. $Na_2O$-$Al_2O_3$-$WO_3$ sample presented even greater difficulties as it consists of two phases, both characterized by pseudo-hexagonal lattices. The problem is particular severe for $NaAl(WO_4)_2$, where an "almost" hexagonal lattice has to be reduced to the monoclinic crystal class in order to achieve structure solution.

Symmetry determination can be performed with automatic routines implemented in *SIR2011* [Burla *et al.*, 2012; Camalli *et al.*, 2012], but such routines are not able to compare different

lattices (hexagonal or orthorombic), as it was the case for $Na_2W_2O_7$ and $NaAl(WO_4)_2$. The internal residual $R_{sym}$ calculated on three-dimensional data, even if affected by residual dynamical effects, is the best indicator for recognizing the correct symmetry and identifying eventual pseudo-symmetries. Remarkably, a wrong space group always delivers a higher structural residual and does not lead to any interpretable structure solution.

### 4.1.3 Applications of $M_2O$-$Al_2O_3$-$WO_3$ system

$K_5Al(W_3O_{11})_2$ have four-coordinated Al sites. When part of Al is substituted by $Cr^{3+}$, this material can be an active media for lasers with emission between 1100 and 1600 nm. These lasers have important application for telecommunication and medical technologies. $NaAl(WO_4)_2$ have six-coordinated Al sites. When part of Al is substituted by $Cr^{3+}$, this material may be a good active media for tunable solid state lasers in the region between 700 and 1000 nm.

## 4.2 $NaTi_3O_6(OH)\cdot 2H_2O$ nanowires

### 4.2.1 Growth mechanism of $NaTi_3O_6(OH)\cdot 2H_2O$ nanowires

The growth process of $NaTi_3O_6(OH)\cdot 2H_2O$ nanowires can be divided into five different stages (Fig. 4.4):

(1) Conversion of the precursor: Complete transformation of the crystalline $TiO_2$-P25 precursor into sodium titanate nanosheets, which appeared in solution as flake-like aggregates. The nanosheets are formed by reaction of $TiO_2$ with NaOH. Structure and exact composition of this sodium titanate phase are still unknown, but probably related to the final product of the hydrothermal reaction: $NaTi_3O_6(OH)\cdot 2H_2O$ nanowires.

(2) "Roll up": The sodium titanate nanosheets roll up and form nanotubes/scrolls. The process starts at the surface of the flake-like aggregates and leads to the formation of isolated nanotubes/scrolls.

(3) Oriented attachment: While the amount of isolated nanotubes still increases, the first titanate nanowires are formed, whose chemical composition and crystal structure differs from that of the nanotubes. The wires are formed *via* oriented attachment [Yuwono *et al.*, 2010] of the sodium titanate nanotubes to the nanowire surface, followed by chemical reaction with NaOH to form a phase that is richer in sodium. The passage from a layer-like 2D to a proper 3D structure appears to be associated with the more ionic character of the Na-rich nanowires.

(4) Ostwald ripening: Nanowires grow at the expense of the nanotubes/scrolls. During the ripening process new wires are still being formed until the supply from the initially formed nanotubes/scrolls is exhausted.

(5) Growth and recrystallization: No nanotubes are present anymore, the growth and recrystallization process ("annealing") is limited by the availability of soluble sodium and titanate species.

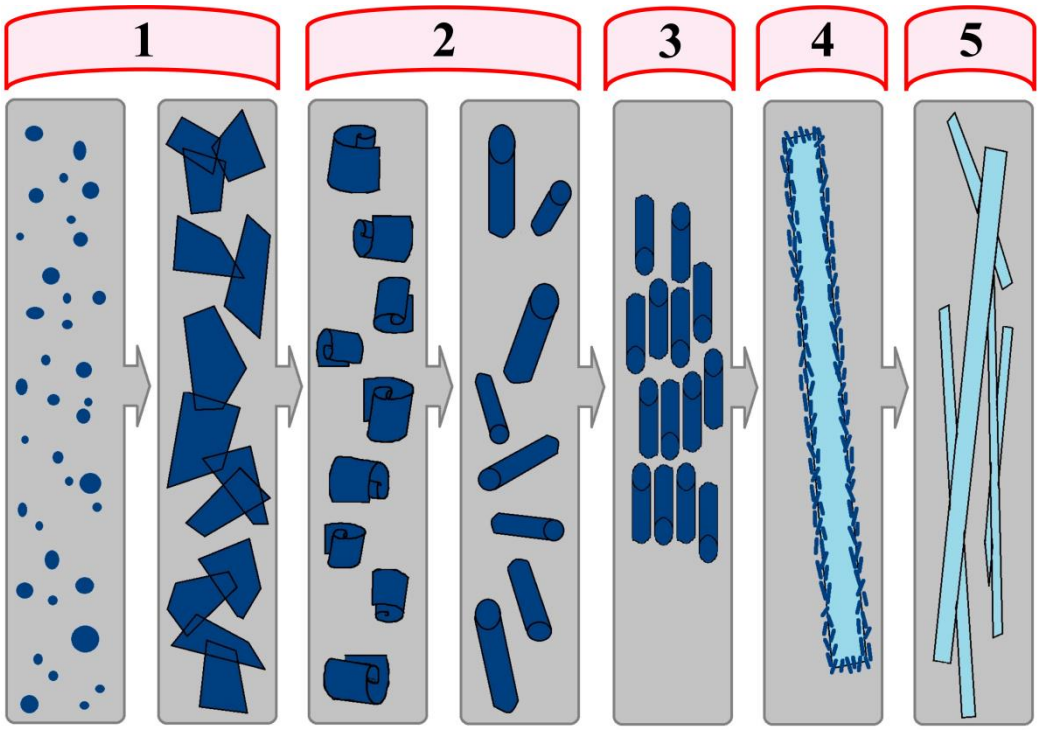


**Figure 4.4 Summary of the growth steps of $NaTi_3O_6(OH)\cdot 2H_2O$ nanowires.**

### 4.2.2 Comparison of $NaTi_3O_6(OH)\cdot 2H_2O$ with related structures

Sodium titanate nanowires with composition $NaTi_3O_6(OH)\cdot 2H_2O$ crystallize in the monoclinic space group *C2/m*. The structure is built up from distorted $\{TiO_6\}$ and $\{NaO_6\}$ octahedra. The Ti-O distances range from 1.78 to 2.26, 1.88 to 2.21, and 1.73 to 2.31 Å for Ti1, Ti2 and Ti3. The individual $\{TiO_6\}$ octahedra share two common vertices and six, four or five common edges for Ti1, Ti2 and Ti3, respectively. This conformation leads to corrugated layers of condensated $\{Ti_6O_{14}\}^{4-}$ complex ions. Despite the similarity of the Ti-atom topology in $Na_2Ti_3O_7$, [Peng *et al.*, 2008] the connectivity of the $\{TiO_6\}$ octahedra is different. Yet, both $NaTi_3O_6(OH)\cdot 2H_2O$ and $Na_2Ti_3O_7$ may be deduced from the lepidocrocite structure [Ewing, 1935] type (Fig. 4.5).

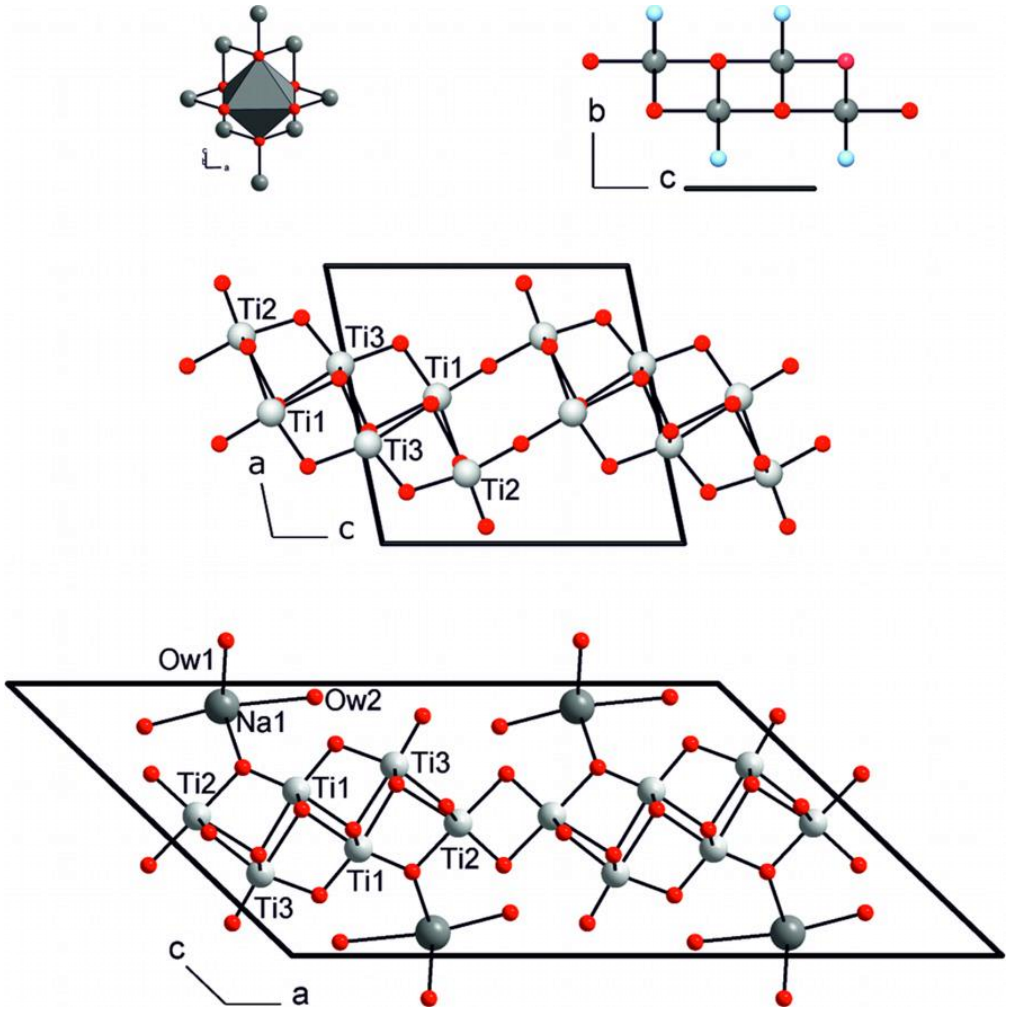


**Figure 4.5 Comparison of $NaTi_3O_6(OH)\cdot 2H_2O$ with related structures.** $MO_6$ octahedra (top left) and view on one layer of the lepidocrocite-type structure (top right; blue: $OH^-$, red: $O^{2-}$). $\{Ti_3O_7\}^{2-}$ layers in $Na_2Ti_3O_7$ (middle) and $\{Ti_3O_6(OH)\}^-$ layers in $NaTi_3O_6(OH)\cdot 2H_2O$ (bottom).

Starting from a hypothetical lepidocrocite-type $TiO_2$, both structure types can be built up by cutting and rejoining the $MO_2$ layers at any third translational period in the [100] direction in such a way that corrugated ribbons of edge-sharing $TiO_6$ octahedra are formed. While the rejoining of the resulting triple chains in $Na_2Ti_3O_7$ occurs *via* two common vertices (per translational period in [010]), in $NaTi_3O_6(OH)\cdot 2H_2O$ it occurs *via* one common edge (per translational period in [010]). In both cases this affords an additional $O^{2-}$ ligand, resulting in negatively charged $\{Ti_3O_7\}^{2-}$ layers. Charge compensation is achieved by inserting two $Na^+$ cations per formula unit for $Na_2Ti_3O_7$ or one hydrated $Na^+$ cation and a $H^+$ forming a hydroxyl group for $NaTi_3O_6(OH)\cdot 2H_2O$. Due to the additional water molecules the crystal structure of $NaTi_3O_6(OH)\cdot 2H_2O$ is more open, which is a prerequisite for its well-known cation-exchange behavior. Recently, the correctness of our structural model was supported by near-edge X-ray absorption spectroscopy (NEXAFS) study [Guttmann *et al.*, 2012].

### 4.2.3 Disorder

The structure is built up from rigid $\{Ti_6O_{14}\}^{4-}$ layers interconnected by relatively weak Coulomb interactions with intercalated $Na^+$ cations and water molecules of crystallization. Therefore, an intrinsic possibility exists for shifting the $\{Ti_6O_{12}(OH)_2\}^{2-}$ layers with respect to each other in the (001) plane. The presence of such planar defects can actually produce the formation of bundles of small wires.

These shifts do not occur in the **b** direction, because the lattice parameter is too short – basically a shift along **b** is a translation transformation. In contrast, the shift of the layers along **a** is very plausible and can be chemically realized by dislocation of sodium cations and structural water molecules. This produces a deviation of the stacking vector **c**. In reciprocal space we observe a change in direction and length of vector **a***, resulting in the observed diffuse scattering along **c***. Disorder along **a** or **b** (i.e. the presence of shorter blocks or fragments of $\{Ti_6O_{14}\}^{4-}$) cannot be realized as it would cause a significant change in the layer topology. In fact, there is no experimental evidence in either the ADT three-dimensional reconstructed reciprocal space or the HRTEM imaging that suggests this kind of defect.

### 4.2.4 Applications of $NaTi_3O_6(OH)\cdot 2H_2O$ nanowires

Sodium titanate nanowires are interesting not only as an important intermediate product in the synthesis of $TiO_2$ nanorods, but also as a raw material that is able to store large amounts of electrochemical energy in a highly reversible and safe manner. $NaTi_3O_6(OH)\cdot 2H_2O$ layered structure consists of $\{Ti_6O_{14}\}^{4-}$ units with hydrated sodium cations and protons in the interlayer space. Upon heating to 600 °C, water is removed irreversibly, the interlayer distances become smaller, and connecting bonds between the octahedral layers form. It was shown [Shirpour *et al.*, 2013] that this dehydrated material have important implications for the development of high-energy-density dual-intercalation systems.

## 4.3 Calcium carbonate

### 4.3.1 Growth mechanism

A heterogeneous nucleation process at the air-water interface occurred in the first step, followed by a second homogeneous nucleation process in solution. The latter led to the formation of amorphous calcium carbonate particles with diameters of approximately 30 nm, which transformed into vaterite and later into calcite *via* a dissolution and recrystallization pathway. Although earlier precipitation species could not be identified with certainty, we can state that this second nucleation process occurs very uniformly in solution and appears to be unique for the $CaCO_3$ system. From our results we could not state if the first calcium carbonate particles form following CNT, SD or another nucleation path. Therefore, further experiments have been carried out using polymethacrylates in order to stabilized ACC and prevent particle growth [Dietzsch *et al.*, 2014].

### 4.3.2 Structure description and properties of vaterite

The determined structure contains most of the motifs present in previously reported models and exclusively explains all the features observed in the Raman spectrum. Moreover it is isotypic with the high-temperature polymorph of $(Y_{0.92}Er_{0.08})BO_3$, previously described as a vaterite-like structure (Fig. 4.6) and recently solved in monoclinic symmetry by the use of neutron diffraction [Lin *et al.*, 2004]. In contrast to calcite and aragonite, the two crystallographic distinct $Ca^{2+}$ cations (8*f*- and 4*c*- site), and the two crystallographic distinct $\{CO_3\}^{2-}$ anions (8*f*- and 4*e*- site) are well separated in layers parallel to (001). The $Ca^{2+}$ cations form distorted hexagonal packed planar arrangements that are interconnected by the $\{CO_3\}^{2-}$ anions in a bridging mode. All planar trigonal $\{CO_3\}^{2-}$ anions are aligned orthogonally to the planes containing the $Ca^{2+}$ cations. Yet, the first set of $\{CO_3\}^{2-}$ anions is oriented with its 2-fold axis along the crystallographic **b** axis, while the second set of $\{CO_3\}^{2-}$ anions is tilted with respect to **b**. This finding is in accordance with the reported optically positive character of vaterite, which was explained by the orthogonal orientation of the $\{CO_3\}^{2-}$ anions to the basal (**a**, **c**) plane of the structure [Bunn, 1946]. The presence of two crystallographic distinct $\{CO_3\}^{2-}$ anions, respectively on site symmetry $C_2$ (4*e*) and $C_1$ (8*f*), gives rise to three Raman active stretching modes, as experimentally reported for natural, biological and synthetic vaterite samples from different origins [Wehrmeister *et al.*, 2010].

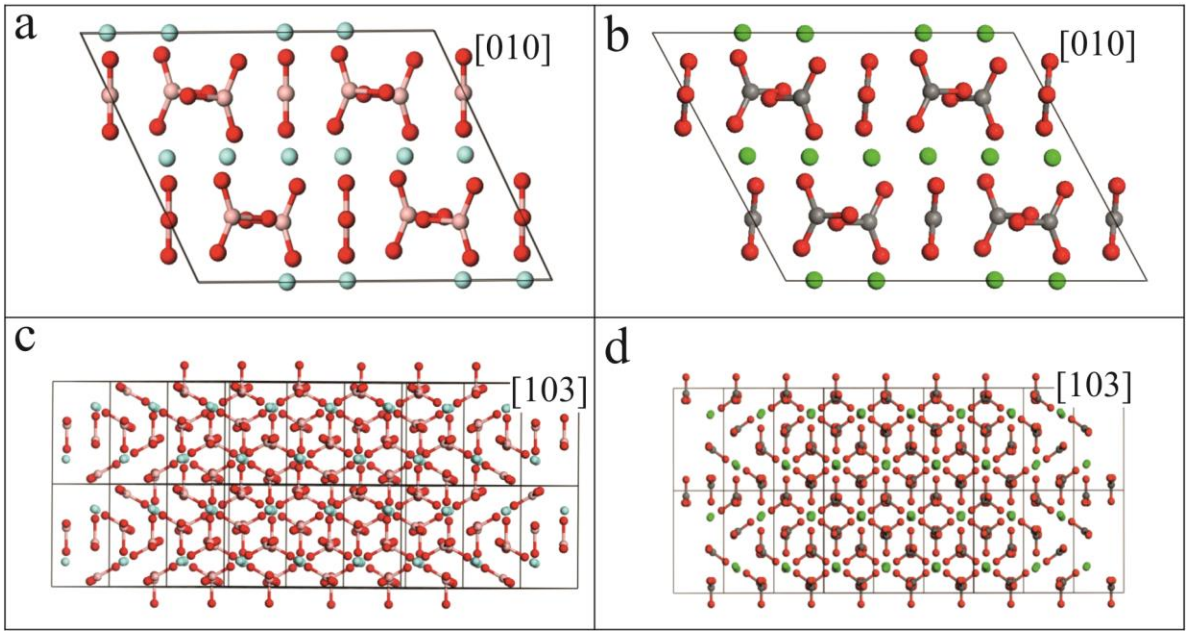


**Figure 4.6 Structure comparison between 2-layer monoclinic model of vaterite and high-temperature polymorph of $(Y_{0.92}Er_{0.08})BO_3$.** (**a**) View down [010] of isotypic structure. (**b**) View down [010] of vaterite structure. (**c**) View down [103] of isotypic structure. (**d**) View down [103] of vaterite structure.

The principle difference between the previous models and the structure reported here is a shift of the $\{CO_3\}^{2-}$ anions layers along the **a** axis, which destroys the hexagonal symmetry. This

structural peculiarity may give rise to a systematic merohedral twinning ("drilling") suggesting the hexagonal symmetry underlying most structure models reported earlier.

The crystal structure of vaterite shows an unusual stacking of cation and anion layers along the [001] direction. This leads to an unfavorable Coulomb contribution to the lattice energy in comparison to the calcite and aragonite polymorphs. Thus, calcite and aragonite are stable polymorphs with well-defined stability regimes in the p,T-phase diagram whereas vaterite is a metastable polymorph whose long-term stabilization is only possible when confined to boundary conditions, such as the nanosize regime and biological activity.

The proposed structure of vaterite is in agreement with a number of experimental findings: (i) The density of vaterite is lower than that of calcite/aragonite even though the $Ca^{2+}$ coordination number (CN) is 8. (ii) The zeta potential of vaterite is highly positive ($Ca^{2+}$ surface layer), whereas that of calcite is slightly negative [Sawada, 1997]. The formation of vaterite under Langmuir monolayers is promoted by highly charged amphiphilic dendron–calixarene [Fricke *et al.*, 2006] or polymeric additives [Aziz *et al.*, 2011]. (iii) Consequently, calcite prefers the adsorption of electrically neutral species whereas negatively charged species are adsorbed on vaterite. (iv) Under sufficiently high $CO_2$ partial pressure the $CaCO_3$ crystallization is controlled kinetically, and vaterite is formed [Dickinson *et al.*, 2002]. (v) The higher surface charge of vaterite leads to a stronger surface hydration, in particular in the presence of 3d transition metal ions, such as $Cu^{2+}$ (CN=6) [Nassrallah-Aboukaïs *et al.*, 1998]. The preference of most 3d transition metals for 6-fold coordination induces a transformation of vaterite into calcite, while a gradual replacement of $Ca^{2+}$ with lanthanides ($Ln^{3+}$) stabilizes the vaterite polymorph.

It is worth to notice that even after all these promising evidences, the discussion about the vaterite structure is still on-going. Some authors [Demichelis *et al.*, 2012] support our finding about disorder inside the vaterite structure, others [Kabalah-Amitai *et al.*, 2013] claim that vaterite is actually composed of at least two different crystallographic structures that coexist within a pseudo-single crystal, the major structure exhibiting hexagonal symmetry and the minor one still unknown.

# Conclusions and Outlook

In order to follow the evolution of a synthesis it is crucial to study the structural features of the intermediate states and metastable phases appearing during the reaction. The investigation of the necessarily small crystallites is difficult or even impossible by X-ray diffraction methods but can be achieved by electron microscopical studies. The most powerful approach appears to be the recently developed method of automated diffraction tomography (ADT). Structure solutions based on electron diffraction data, even collected with a tomographic approach, do not provide the same quality of typical structure solutions based on X-ray single crystal data. This is partially due to the persistent dynamical effects and partially to the immaturity of the method. Remarkably, all structure solutions achieved up to now are based on "as-integrated" intensities because no correction for absorption and Lorentz factor has been applied, despite the evident change in sample thickness during the tilt. Consequently the structural residual *R* is typically in a range of 15-30%, some light atoms cannot be recognized in the *ab-initio* potential map and the interatomic distances have a relatively high deviation. Despite this, the tomographic acquisition of electron diffraction data can nowadays be considered a quasi-routine and relatively fast protocol for structure determination of nanocrystalline phases, able to deliver reliable models that describe the main features of the structure and the atomic coordination.

The main strength of ADT method is the ability to collect data from single nanoscopic crystallites, whose structure characterization eludes conventional crystallographic methods due to small crystalline size, low purity, structural complexity, or low volumetric availability. Hence, ADT method allows the structure determination of minor phases in polyphasic mixtures and of intermediate metastable species that are energetically confined to a nanocrystalline size. Moreover the analysis of the internal residual $R_{sym}$ against three-dimensional data for different crystal classes is an efficient way to recognize the correct symmetry and detect pseudo-symmetries that could be unseen in XRPD data. Finally, this method delivers a three-dimensional description of disorder features at the nanoscale, such as planar defects and local modulations. Due the low electron dose rate required for performing ADT, this method can be straightforwardly applied to any type of nanocrystalline material, even if highly beam sensitive. ADT applications may have important impacts on a wide range of scientific disciplines, from Inorganic and Organic Chemistry to Material Sciences, Geology and Pharmaceutics.

# Bibliography


1. Abraham F.F. (1974) *Homogeneous Nucleation Theory*. Academic Press, Amsterdam.
2. Adachi M., Murata Y., Harada M., Yoshikawa S. (2000) *Chem. Lett.* **29**:942.
3. Adrian M., Dubochet J., Lepault J., McDowall A.W. (1984) *Nature* **308**:32.
4. Altomare A., Camalli M., Cuocci C., Giacovazzo C., Moliterni A., Rizzi R. (2009) *J. Appl. Crystallogr.* **42**:1197.
5. Anderson A. (1996) *Spectrosc. Lett.* **29**:819.
6. Andreassen J.-P. (2005) *J. Cryst. Growth* **274**:256.
7. Andrusenko I., Mugnaioli E., Gorelik T.E., Koll D., Panthöfer M., Tremel W., Kolb U. (2011) *Acta Crystallogr. B* **67**:218.
8. Astier J.P. & Veesler S. (2008) *Cryst. Growth Des.* **8**:4215.
9. Avanesov A.G., Lebedev V.A., Zhorin V.V., Okhrimchuk A.G., Shestakov A.V. (1997) *J. Lumin*. **72–74**:155.
10. Aziz B., Gebauer D., Hedin N. (2011) *CrystEngComm.* **13**:4641.
11. Bach U., Corr D., Lupo D., Pichot F., Ryan M. (2002) *Adv.Mater.* **14**:845.
12. Baerlocher C., Gramm F., Massüger L., McCusker L.B., He Z., Hovmöller S., Zou X. (2007) *Science* **315**:1113.
13. Bavykin D.V., Friedrich J.-M., Walsh F.-C. (2006) *Adv. Mater.* **18**:2807.
14. Bavykin D.V., Walsh F.C. (2009) *Eur. J. Inorg. Chem.* **2009**:977.
15. Beck M., Lučić V., Förster F., Baumeister W., Medalia O. (2007) *Nature* **449**:611.
16. Becker R. & Döring W. (1935) *Ann. Phys*. **24**:719.
17. Behrens G., Kuhn L.T., Ubic R., Heuer A.H. (1995) *Spectrosc. Lett.* **28**:983.
18. Bellussi G., Montanari E., Di Paola E., Millini R., Carati A., Rizzo C., Parker W.O., Gemmi M., Mugnaioli E., Kolb U., Zanardi S. (2012) *Angew. Chem. Int. Ed.* **51**:666.
19. Birkel A., Reuter F., Koll D., Frank S., Branscheid R., Panthöfer M., Rentschler E., Tremel W. (2011) *CrystEngComm.* **13**:2487.
20. Birkel C.S., Mugnaioli E., Gorelik T., Kolb U., Panthöfer M., Tremel W. (2010) *J. Am. Chem. Soc.* **132**:9881.
21. Boistelle R. & Astier J.P. (1988) *J. Cryst. Growth* **90**:14.
22. Boullay P., Palatinus L., Barrier N. (2013) *Inorg. Chem.* **52**:6127.
23. Bragg W.L. (1913) *P. R. Soc. London A* **89**:248.
24. Bragg W.L. (1924) *P. R. Soc. London A* **105**:16.
25. Brecevic L., Nothig-Laslo V., Kralj D., Popovic S. (1996) *J. Chem. Soc. Faraday Trans*. **92**:1017.
26. Brik M.G., Lebedev V.A., Stroganova E.V. (2007) *J. Phys. Chem. Solids* **68**:1796.
27. Bryce L., Bultz E.B., Aebi D. (2008) *J. Am. Chem. Soc.* **130**:9282.
28. Bunn C.W. (1946) *Chemical Crystallography*. Clarendon Press, Oxford.
29. Burla M.C., Caliandro R., Camalli M., Carrozzini B., Cascarano G.L., de Caro L., Giacovazzo C., Polidori G., Siliqi D., Spagna R. (2007) *J. Appl. Crystallogr.* **40**:609.
30. Burla M.C., Caliandro R., Camalli M., Carrozzini B., Cascarano G.L., Giacovazzo C., Mallamo M., Mazzone A., Polidori G., Spagna R. (2012) *J. Appl. Crystallogr*. **45**:357.
31. Burton W.K. & Cabrera N. (1949*a*) *Discuss. Faraday Soc.* **5**:33.
32. Burton W.K. & Cabrera N. (1949*b*) *Discuss. Faraday Soc.* **5**:40.
33. Bykov A.B., Petricevic V., Sharonov M.Yu., Steiner J., Isaacs L.L., Avrahami T., Di Blasi R., Sengupta S., Alfano R.R. (2005) *J. Cryst. Growth* **274**:149.

34. Camalli M., Carrozzini B., Cascarano G.L., Giacovazzo C. (2012) *J. Appl. Crystallogr.* **45**:351.
35. Cavalli E., Belletti A., Brik M.G. (2008) *J. Phys. Chem. Solids* **69**:29.
36. Casey W.H. & Swaddle T.W. (2003) *Rev. Geophys.* **41**:1008.
37. Chan J.W. & Hilliard J.E. (1958) *J. Chem. Phys.* **28**:258.
38. Chan J.W. & Hilliard J.E. (1959) *J. Chem. Phys.* **31**:688.
39. Cheary R.W. & Coelho A. (1992) *J. Appl. Crystallogr.* **25**:109.
40. Chen Q., Du G., Zhang S., Peng L.-M. (2002) *Acta Crystallogr. B* **58**:587.
41. Chen W. & Boulon G. (2003) *Opt. Mater*. **24**:163.
42. Chen X. & Mao S.S. (2007) *Chem. Rev.* **107**:2891.
43. Coelho A.A. (2007*a*) *TOPAS-Academic, Version 4.1*. Coelho Software, Brisbane, Australia.
44. Coelho A.A. (2007*b*) *Acta Crystallogr. A* **63**:400.
45. Coelho A.A. (2008) *TOPAS-Academic, Version 4.2.* Bruker AXS, Karlsruhe, Germany.
46. Coelho A.A. & Cheary R.W. (1997) *Comput. Phys. Commun.* **104**:15.
47. Cowley J.M. (1956) *Acta Crystallogr.* **9**:391.
48. Cowley J.M. (1995) *Diffraction Physics*, 3rd edn. Elsevier, Amsterdam.
49. Cowley J.M., Goodman P., Vainshtein B.K., Zvyagin B.B., Dorset D.L. (2001) *International tables for crystallography. Volume B: Reciprocal space*, 2nd edn. (ed. Shmueli U.). Kluwer Academic Publishers, Dordrecht, Boston, London.
50. Cölfen H. & Antonietti M. (2008) *Mesocrystals and Nonclassical Crystallization*. John Wiley & Sons Ltd, Chichester.
51. Crewe A.V., Langmore J.P., Isaacson M.S. (1975) Chapter 4 in *Physical Aspects of Electron Microscopy and Microbeam Analysis* (eds. Siegel B.M. & Beaman D.R.). Wiley, New York.
52. Cubillas P. & Anderson M.W. (2010) *Synthesis Mechanism: Crystal Growth and Nucleation* in *Zeolites and Catalysis: Synthesis, Reactions and Applications* (eds. Čejka J., Corma A., Zones S.) Wiley-VCH Verlag GmbH & Co. KGaA, Weinheim.
53. da Silva M.A.F.M., Barthem R.B., Sosman L.P. (2006) *J. Solid State Chem*. 179:3718.
54. Dandeu A., Humbert B., Carteret C., Muhr H., Plasari E., Bossoutrot J.M. (2006) *Chem. Eng. Technol.* **29**:221.
55. Danino D. (2012) *Curr. Opin. Colloid Interface Sci.* **17**:316.
56. David W.I.F., Shankland K., McCusker L.B., Baerlocher C. (2002) *Structure Determination from Powder Diffraction Data.* Oxford University Press, New York.
57. Davisson C.J. & Germer L.H. (1927*a*) *Nature* **119**:558.
58. Davisson C.J. & Germer L.H. (1927*b*) *Phys.Rev.* **30**:705.
59. de Backer A., Garreau J.C., Razdobreev I.M., Szriftgiser P., Voroshilov I.V., Lebedev V.A., Stroganova E.V. (2003) *Opt. Commun*. **222**:351.
60. Debye P. (1915) *Ann. Phys.* **46**:809.
61. Debye P.& Scherrer P. (1916) *Phys. Z.* **17**:277.
62. Demichelis R., Raiteri P., Gale J.D., Quigley D., Gebauer D. (2011) *Nat. Commun.* **2**:590.
63. Demichelis R., Raiteri P., Gale J.D., Dovesi R. (2012) *CrystEngComm.* **14**:44.
64. Denysenko D., Grzywa M., Tonigold M., Streppel B., Krkljus I., Hirscher M., Mugnaioli E., Kolb U., Hanss J., Volkmer D. (2011) *Chem.- Eur. J.* **17**:1837.
65. Dickinson S.R., Henderson G.E., McGrath K.M. (2002) *J. Cryst. Growth* **244**:369.
66. Dietzsch M., Andrusenko I., Branscheid R., Kolb U., Tremel W. (2014) in preparation.
67. Dorset D.L. (1995*a*) *Structural Electron Crystallography.* Plenum Press, New York.
68. Dorset D.L. (1995*b*) *Proc. Nat. Acad. Sci. USA* **92**:10074.
69. Dorset D.L. (1996) *Acta Crystallogr. B* **52**:753.

70. Dorset D.L. (2003) *Z. Kristallogr.* **218**:237.
71. Dorset D.L. (2007) *Ultramicroscopy* **107**:453.
72. Dorset D.L. & Hauptman H.A. (1976) *Ultramicroscopy* **1**:195.
73. Dorset D.L., Roth W.J., Gilmore C.J. (2005) *Acta Crystallogr. A* **61**:516.
74. Dorset D.L., Gilmor C.J., Jorda J.L., Nicolopoulos S. (2007) *Ultramicroscopy* **107**:462.
75. Doyle P.A. & Turner P.S. (1968) *Acta Crystallogr. A* **24**:390.
76. Dubochet J., Adrian M., Chang J.-J., Homo J.-C., Lepault J., McDowall A.W., Schultz P. (1988) *Q. Rev. Biophys.* **21**:129.
77. Ellingboe J.L. & Runnels J.H. (1966) *J. Chem. Eng. Data* **11**:323.
78. Ewing F.J. (1935) *J. Chem. Phys.* **3**:420.
79. Faatz M., Gröhn F., Wegner G. (2004) *Adv. Mater.* **16**:996.
80. Faivre R. & Wallaeys R. (1950) *C. R. Acad. Sci. Paris* **231**:285.
81. Favvas E.P. & Mitropoulos A.Ch. (2008) *J. Eng. Sci. Technol. Rev.* **1**:25.
82. Feyand M., Mugnaioli E., Vermoortele F., Bueken B., Dieterich J.M., Reimer T., Kolb U., de Vos D., Stock N. (2012) *Angew. Chem. Int. Ed.* **124**:10519.
83. Frank F.C. (1949) *Discuss. Faraday Soc.* **5**:48.
84. Fricke M., Volkmer D., Krill C.E., Kellermann M., Hirsch A. (2006) *Cryst. Growth Des.* **6**:1120.
85. Friedrich W., Knipping P., von Laue M. (1912) *Sitzungsber. Bayer. Akad. Wiss.* **303**; reprint (1952) in *Naturwiss.* **39**:36.
86. Fultz B. & Howe J.M. (2002) *Transmission Electron Microscopy and Diffractometry of Materials*, 2nd edn. Springer, Berlin.
87. Furrer G., Phillips B.L., Ulrich K.U., Pothig R., Casey W.H. (2002) *Science* **297**:2245.
88. Gabrielli C., Jaouhari R., Joiret S., Maurin G. (2000) *J. Raman Spectrosc.* **31**:497.
89. Gebauer D., Voelkel A., Cölfen H. (2008) *Science* **322**:1819.
90. Gebauer D. & Cölfen H. (2011) *Nano Today* **6**:564.
91. Gemmi M., Klein H., Rageau A., Strobel P., le Cras F. (2010) *Acta Crystallogr. B* **66**:60.
92. Gemmi M., Fischer J., Merlini M., Poli S., Fumagalli P., Mugnaioli E., Kolb U. (2011) *Earth Planet. Sci. Lett.* **310**:422.
93. Gemmi M., Campostrini I., Demartin F., Gorelik T.E., Gramaccioli C.M. (2012) *Acta Crystallogr. B* **68**:15.
94. Gemmi M., Galanis A.S., Karavassili F., Pratim Das P., Calamiotou M., Gantis A., Kollia M., Margiolaki I., Nicolopoulos S. (2013) *Microsc. Anal.* **27**:24.
95. Gluchowski P., Pazik R., Hreniak D., Strek W. (2009) *J. Lumin.* **129**:548.
96. Gorelik T.E., Stewart A.A., Kolb U. (2011) *J. Microsc.* **244**:325.
97. Gorelik T.E., van de Streek J., Kilbinger A.F.M., Brunklaus G., Kolb U. (2012*a*) *Acta Crystallogr. B* **68**:171.
98. Gorelik T.E., Sarfraz A., Kolb U., Emmerling F., Rademann K. (2012*b*) *Cryst. Crowth Des.* **12**:3239.
99. Gurov V.V., Tsvetkov E.G., Yurkin A.M. (2008) *Opt. Mater.* **30**:1399.
100. Guttmann P., Bittencourt C., Rehbein S., Umek P., Ke X., van Tendeloo G., Ewels C.P., Schneider G. (2012) *Nat. Photonics* **6**:25.
101. Haider M., Rose H., Uhlemann S., Kabius B., Urban K. (1998) *J. Electron Microsc.* **47**:395.
102. Hanneman R.L. (2013) *Salt, the essence of life - Interdisciplinary Curriculum for High School Students*. The Salt Institute, Alexandria, Virginia.
103. Hartman P. & Bennema P. (1980) *J. Cryst. Growth* **49**:145.

104. Hermanowicz K., Hanuza J., Maczka M., Deren P.J., Mugenski E., Drulis H., Sokolska I., Sokolnicki J. (2001*a*) *J. Phys. Condens. Matter*. **13**:5807.
105. Hermanowicz K., Maczka M., Deren P.J., Hanuza J., Strek W., Drulis H. (2001*b*) *J. Lumin.* **92**:151.
106. Hermanowicz K. (2006) *J. Phys. Condens. Matter*. **18**:10601.
107. Holton J.M. & Frankel K.A. (2010) *Acta Crystallogr. D* **66**:393.
108. Hono K. & Hirano K.-I. (1987) *Phase Transit.* **10**:223.
109. Horn D. & Rieger J. (2001) *Angew. Chem. Int. Ed.* **40**:4330.
110. Howie A. & Whelan M.J. (1961) *P. R. Soc. London A* **263**:217.
111. Hsu C.-Y., Chiu T.-C., Shih M.-H., Tsai W.-J., Chen W.-Y., Lin C.-H. (2010) *J. Phys. Chem. C* **114**:4502.
112. Huang J., Cao Y., Huang Q., He H., Liu Y., Guo W., Hong M. (2009) *Cryst. Growth Des.* **9**:3632.
113. Huang J., Cao Y., Deng Z., Tong H. (2011) *J. Solid State Chem.* **184**:712.
114. Huang N. (2011) *Digitimes.*
115. Huang N. (2012) *Digitimes.*
116. Hull A.W. (1917) *Phys. Rev.* **10**:661.
117. Hull A.W. (1919) *J. Am. Chem. Soc.* **41**:1168.
118. Hull A.W. (1921) *Phys. Rev.* **17**:571.
119. Ivanova D., Nikolov V., Peshev P. (2007) *J. Cryst. Growth*. **308**:84.
120. Jiang J., Jorda J.L., Yu J., Baumes L.A., Mugnaioli E., Diaz-Cabanas M.J., Kolb U., Corma A. (2011) *Science* **333**:1131.
121. Kabalah-Amitai L., Mayzel B., Kauffmann Y., Fitch A.N., Bloch L., Gilbert P.U.P.A., Pokroy B. (2013) *Science* **340**:454.
122. Kamhi S.R. (1963) *Acta Crystallogr.* **16**:770.
123. Kaminskii A.A. (1996) *Crystalline Lasers: Physical Processes and Operating Schemes*. London, CRC Press.
124. Kashchiev D. (2000) *Nucleation: Basic Theory with Applications*. Butterworth-Heinemann, Oxford.
125. Kasuga T., Hiramatsu M., Hoson A., Sekino T., Niihara K. (1998) *Langmuir* **14**:3160.
126. Kavan L., Kalbac M., Zukalova M., Exnar I., Lorenzen V., Nesper R., Graetzel M. (2004) *Chem. Mater.* **16**:477.
127. Kim J.S., Kim J.S., Park H.L. (2004) *Solid State Commun*. **131**:735.
128. Kisielowski C., Erni R., Freitag B. (2008*a*) *Microsc. Microanal.* **14**:78.
129. Kisielowski C., Freitag B., Bischoff M., van Lin H., Lazar S., Knippels G., Tiemeijer P., van der Stam M., von Harrach S., Stekelenburg M., Haider M., Uhlemann S., Müller H., Hartel P., Kabius B., Miller D., Ptrov I., Olson E.A., Donchev T., Kenik E.A., Lupini A.R., Bentley J., Pennycook S.J., Anderson I.M., Minor A.M., Shmid A.K., Duden T., Radmilovic V., Ramasse Q.M., Watanabe M., Erni R., Stach E.A., Denes P., Dahmen U. (2008*b*) *Microsc. Microanal.* **14**:469.
130. Klein H. (2011) *Acta Crystallogr. A* **67**:303.
131. Klevtsova R.F. (1975) *Dokl. Akad. Nauk SSSR*. **221**:1322; *Sov. Phys. Dokl. (Engl. Transl.)* **20**:242.
132. Klug A. (1977) *Mater. Res. Bull*. **12**:837.
133. Knoll M. & Ruska E. (1932) *Phys. Z.* **78**:318.

134. Kolb U., Nihtianova D., Li J., Kovacheva D., Nikolov I., Nikolov V. (2005) *Юбилеен сборник 10 години Централна лаборатория по минералогия и кристалография „Акад. Иван Костов" към БАН.* Marin Drinov, Sofia.
135. Kolb U., Gorelik T., Kübel C., Otten M.T. & Hubert D. (2007) *Ultramicroscopy* **107**:507.
136. Kolb U., Gorelik T., Otten M.T. (2008) *Ultramicroscopy* **108**:763.
137. Kolb U., Gorelik T.E., Mugnaioli E., Stewart A. (2010) *Polym. Rev.* **50**, 385.
138. Kolb U., Mugnaioli E., Gorelik T.E. (2011) *Cryst. Res. Technol.* **46**:542.
139. Kolen'ko Y.V., Kovnir K.A., Gavrilov A.I., Garshev A.V., Frantti J., Lebedev O.I., Churagulov B.R., van Tendeloo G., Yoshimura M. (2006) *J. Phys. Chem.* B**110**:4030.
140. Koseva I., Nikolov V., Yordanova A., Tzvetkov P., Kovacheva D. (2011) *J. Alloys Compd*. **509**:7022.
141. Kossel W. & Möllenstedt G. (1939) *Ann. Phys.* **36**:113.
142. Krell A., Klimke J., Hutzler T. (2009) *Opt. Mater*. **31**:1144.
143. Kuck S., Fornasiero L., Mix E., Huber G. (2000) *J. Lumin*. **87–89**:1122.
144. Kuwahara N., Sato H., Kubota K. (1992) *J. Chem. Phys.* **97**:5905.
145. Kühlbrandt W., Wang D.N., Fujiyoshi Y. (1994) *Nature* **367**:614.
146. Lan Y., Gao X.P., Zhu H.Y., Zheng Z.F., Yan T.Y., Wu F., Ringer S.P., Song D.Y. (2005) *Adv. Funct. Mater*. **15**:1310.
147. Langer J.S. (1971) *Ann. Phys.* **65**:53.
148. Larson M.A. (1991) *Adv. Ind. Cryst.* **1991**:20.
149. Larson M.A. & Garside J. (1986) *Chem. Eng. Sci.* **41**:1285.
150. le Bail A., Ouhenia S., Chateigner D. (2011) *Powder Diffr.* **26**:16.
151. Lim S.H., Luo J., Zhong Z., Ji W., Lin J. (2005) *Inorg. Chem.* **44**:4124.
152. Lin J., Sheptyakov D., Wang Y., Allenspach P. (2004) *Chem. Mater.* **16**: 2418.
153. Lipson H. & Cochran W. (1966) *The Determination of Crystal Structures*. Cornell University Press, Ithaca, New York.
154. Lippmann F. (1973) *Sedimentary Carbonate Materials.* Springer, New York.
155. López-Sandoval E., Vázquez-López C., Zendejas-Leal B.E., Ramos G., San Martín-Martínez E., Muñoz Aguirre N., Reguera E. (2007) *Desalination* **217**:85.
156. Lupei V. (2009) *Opt. Mater*. **31**:701.
157. Ma R., Bando Y., Sasaki T. (2003) *Chem. Phys. Lett.* **380**:577.
158. Mangin D., Puel F., Veesler S. (2009) *Org. Process Res. Dev.* **13**:1241.
159. McLaren A.C. (1991) *Transmission electron microscopy of minerals and rocks.* Cambridge University Press, New York.
160. Meng X., Wang D., Liu J., Zhang S. (2004) *Mater. Res. Bull.* **39**:2163.
161. Merceille A., Weinzaepfel E., Barre Y., Grandjean A. (2011) *Adsorption* **17**:967.
162. Meyer H.J. (1959) *Angew. Chem.* **71**:678.
163. Meyer H.J. (1969) *Z. Kristallogr.* **128**:183.
164. Miller M.K., Hyde J.M., Hetherington M.G., Cerezo A., Smith G.D.W., Elliott C.M. (1995) *Acta Metall. Mater* **43**:3385.
165. Morgado E.-J., de Abreu M.-A.-S., Moure G.-T., Marinkovic B.-A., Jardim P.-M., Araujo A.-S. (2007) *Chem. Mater.* **19**:665.
166. Morse J.W., Arvidson R.S., Lüttge A. (2007) *Chem. Rev*. **107**:342.
167. Mugnaioli E., Gorelik T., Kolb U. (2009) *Ultramicroscopy* **109**:758.
168. Mugnaioli E., Andrusenko I., Schüler T., Loges N., Dinnebier R.E., Panthöfer M., Tremel W., Kolb U. (2012*a*) *Angew. Chem. Int. Ed.* **51**:7041.

169. Mugnaioli E., Sedlmaier S.J., Öckler O., Kolb U., Schnick W. (2012*b*) *Eur. J. Inorg. Chem.* **2012**:121.
170. Mugnaioli E., Gorelik T.E., Stewart A., Kolb U. (2012*c*) *"Ab-initio" structure solution of nano-crystalline minerals and synthetic materials by automated electron tomography* in *Minerals as Advanced Materials II* (ed. Krivovichev S.V.) Springer, Berlin, Heidelberg.
171. Mugnaioli E., Kolb U. (2013) *Microporous Mesoporous Mater.* **166**:93.
172. Mullin J.W. (2001) *Crystallization,* 4th ed. Butterworth-Heinemann, Oxford.
173. Nagase T., Ebina T., Iwasaki T., Hayashi H., Onodera Y., Chatterjee M. (1999) *Chem. Lett.* **9**:911.
174. Nassrallah-Aboukaïs N., Boughriet A., Laureyns J., Aboukaïs A., Fischer J.C., Langelin H.R., Wartel M. (1998) *Chem. Mater.* **10**:238.
175. Navrotsky A. (2004) *P. Natl. Acad. Sci. USA* **101**:12096.
176. Ngamsinlapasathian S., Sakulkhaemaruethai S., Pavasupree S., Kitiyanan A., Sreethawong T., Suzuki Y., Yoshikawa S. (2004) *J. Photochem. Photobiol. A* **164**:145.
177. Nicolopoulos S., González-Calbet J.M., Vallet-Regí M., Corma A., Corell C., Guil J.M., Pérez-Pariente J. (1995) *J. Am. Chem. Soc.* **117**:8947.
178. Nikolov I., Nikolov V., Kovacheva D., Peshev P. (2003*a*) *J. Alloys Compd*. **349**:341.
179. Nikolov I., Nikolov V., Kovacheva D., Peshev P. (2003*b*) *J. Alloys Compd*. **351**:289.
180. Nikolov I., Nikolov V., Kovacheva D., Peshev P. (2003*c*) *J. Alloys Compd*. **351**:202.
181. Nikolov I., Nikolov V., Peshev P. (2003*d*) *J. Cryst. Growth* **254**:107.
182. Nikolov I., Mateos X., Güell F., Massons J., Nikolov V., Peshev P., Diaz F. (2004) *Opt. Mater*. **25**:53.
183. Ohara M. & Reid R.C. (1973) *Modeling Crystal Growth Rates from Solution*. Prentice Hall, Englewood Cliffs, New Jersey.
184. Ohnishi N. & Hiraga K. (1996) *J. Electron Microsc.* **45**:85.
185. Ohtani B., Prieto-Mahaney O.O., Li D., Abe R. (2010) *J. Photochem. Photobiol. A* **216**:179.
186. Okada K., Morikawa H., Marumo F., Iwai S. (1975) *Acta Crystallogr. B* **31**:1200.
187. Okada K., Morikawa H., Marumo F., Iwai S. (1976) *Acta Crystallogr. B* **32**:1522.
188. O'Regan B. & Graetzel M. (1991) *Nature* **353**:737.
189. Ostwald W. (1897) *Z. Phys. Chem.* **22**:289.
190. Padlyak B.V., Grinberg M., Lukasiewicz T., Kisielewski J., Swirkowicz M. (2003) *J. Alloys Compd*. **361**:6.
191. Palatinus L., Klementová M., Dřínek V., Jarošová M., Petříček V. (2011) *Inorg. Chem.* **50**:3743.
192. Patnaik P. (2003) *Handbook of Inorganic Chemical Compounds*. McGraw-Hill, New York.
193. Patra A., Tallman R.E., Weinstein B.A. (2005) *Opt. Mater*. **27**:1396.
194. Peng C.-W., Richard-Plouet M., Ke T.-Y., Lee C.-Y., Chiu H.-T., Marhic C., Puzenat E., Lemoigno F., Brohan L. (2008) *Chem. Mater.* **20**:7228.
195. Peng L.-M., Dudarev S.L., Whelan M.J. (2004) *High-Energy Electron Diffraction and Microscopy.* Oxford University Press, New York.
196. Perry C. (2003) *Biomineralization* **54**:291.
197. Pettersen E.F., Goddard T.D., Huang C.C., Couch G.S., Greenblatt D.M., Meng E.C., Ferrin T.E. (2004) *J. Comput. Chem.* **25**:1605.
198. Pinsker Z.G. (1953) *Electron Diffraction*. Butterworth, London.

199. Pouget E.M., Bomans P.H.H., Goos J.A.C.M., Frederik P.M., de With G., Sommerdijk N.A.J.M. (2009) *Science* **323**:1455.
200. Punda I. & Prikhodko D. (2009) *Agribusiness Handbook: Sugar beet white sugar*. Food and Agriculture Organization, Rome, Italy.
201. Reimer L. & Kohl H. (2008) *Transmission electron microscopy, physics of image formation*, 5th edn. Springer, New York.
202. Rietveld H.M. (1969) *J. Appl. Crystallogr.* **2**:65.
203. Rigamonti R. (1936) *Gazzetta Chimica Italiana* **66**:174.
204. Rius J., Mugnaioli E., Vallcorba O., Kolb U. (2013) *Acta Crystallogr. A* **69**:396.
205. Rodriguez-Blanco J.D., Shaw S., Benning L.G. (2011) *Nanoscale* **3**:265.
206. Rose H. (1990) *Optik* **85**:19.
207. Rosenberger F. (1979) *Fundamentals of Crystal Growth* in *Solid-State Sciences. Springer Series Volume1*. Springer-Verlag, Berlin.
208. Rozhdestvenskaya I., Mugnaioli E., Czank M., Depmeier W., Kolb U., Reinholdt A., Weirich T. (2010) *Mineral. Mag.* **74**:159.
209. Rozhdestvenskaya I., Mugnaioli E., Czank M., Depmeier W., Kolb U., Merlino S. (2011) *Mineral. Mag.* **75**:2833.
210. Ruska E. (1935) *Res. Prog.* **1**:18.
211. Ruska E. & Knoll M. (1931) *Z. Techn. Phys.* **12**:389.
212. Sander B. & Golas M.M. (2011) *Microsc. Res. Tech.* **74**:642.
213. Sarakinou E., Mugnaioli E., Lioutas C.B., Vouroutzis N., Frangis N., Kolb U., Nikolopoulos S. (2012) *Semicond. Sci. Technol.* **27**:105003.
214. Sawada K. (1997) *Pure Appl. Chem.* **69**:921.
215. Schlitt S., Gorelik T.E., Stewart A.A., Schömer E., Raasch T., Kolb U. (2012) *Acta Crystallogr. A* **68**:536.
216. Schüler T. & Tremel W. (2011) *Chem. Commun.* **47**:5208.
217. Sedlmaier S.J., Mugnaioli E., Oeckler O., Kolb U., Schnick W. (2011) *Chem.-Eur. J.* **17**:11258.
218. Sheldrick G.M. (2008) *Acta Crystallogr. A* **64**:112.
219. Shirpour M., Cabana J., Doeff M. (2013) *Energy Environ. Sci.* **6**:2538.
220. Shlossmacher P., Matijevic M., Thesen A., Benner G. (2005) *Imaging & Microscopy* **2**:50.
221. Smolders C.A., van Aartsen J.J., Steenbergen A. (1971) *Kolloid Z. Z. Polym.* **243**:14.
222. Spence J.C.H. (2003) *High-resolution electron microscopy*, 3rd edn. Oxford University Press, New York.
223. Tanner P.A. (2004) *Chem. Phys. Lett*. **388**:488.
224. Tavare N.S. (1995) *Industrial Crystallization*. Plenum Press, New York.
225. Taylor K.A. & Glaeser R.M. (1976) *J. Ultrastructure Res.* **55**: 448.
226. Thomson G.P. & Reid A. (1927) *Nature* **119**:890.
227. Torchia G.A., Schinca D., Khaidukov N.M., Tocho J.O (2002) *Opt. Mater*. **20**:301.
228. Toschev S. (1973) *Homogeneous nucleation* in *Crystal Growth: An Introduction* (ed. Hartman P.), North Holland, Amsterdam.
229. Tzvetkov P., Ivanova D., Kovacheva D., Nikolov V. (2009) *J. Alloys Compd*. **470**:492.
230. Umek P., Korošec R.C., Jančar B., Dominko R., Arčon D. (2007) *J. Nanosci. Nanotechnol.* **7**:3502.
231. Unwin P.N.T. & Henderson R. (1975) *J. Mol. Biol.* **94**:425.
232. Vainshtein B.K. (1956) *Soviet Phys. – Crystallogr.* **1**:117.

233. Vainshtein B.K. (1964) *Structure analysis by electron diffraction*. Pergamon Press, Oxford.
234. Vainshtein B.K. & Ibers J.A. (1958) *Soviet Phys. – Crystallogr.* **3**:417.
235. Varghese O.K., Gong D., Paulose M., Ong K.G., Dickley E.C., Grimes C.A. (2003) *Adv. Mater.* **15**:624.
236. Vincent R. & Midgley P.A. (1994) *Ultramicroscopy* **53**:271.
237. Viswanathan K. (1974) *Dalton Trans*. **20**:2170.
238. Voigt-Martin I.G., Yan D.H., Yakimansky A., Schollmeyer D., Gilmore C.J., Bricogne G. (1995) *Acta Crystallogr. A* **51**:849.
239. Volmer M. & Weber A. (1925) *Z. Phys. Chem*. **119**:277.
240. Volmer M. & Schultz W. (1931) *Z. Phys. Chem.* **156**:1.
241. Wagner P., Terasaki O., Ritsch S., Nery J.G., Zones S.I., Davis M.E., Hiraga K. (1999) *J. Phys. Chem. B* **103**:8245.
242. Wang G., Han X., Song M., Lin Z., Wang G., Long X. (2007) *Mater. Lett*. **61**:3886.
243. Wang G., Long X., Zhang L., Wang G. (2008) *J. Cryst. Growth*. **310**:624.
244. Wang J. & Becker U. (2009) *Am. Mineral.* **94**:380.
245. Wehrmeister U., Soldati A.L., Jacob D.E., Häger T., Hofmeister W. (2010) *J. Raman Spectrosc.* **41**:193.
246. Weirich T.E. (2001) *Acta Crystallogr. A* **57**:183.
247. Weirich T.E. (2003) *Z. Kristallogr.* **218**:269.
248. Weirich T.E., Ramlau R., Simon A., Hovmöller S., Zou X. (1996) *Nature* **382**:144.
249. Weirich T.E., Portillo J., Cox G., Hibst H., Nicolopoulos S. (2006) *Ultramicroscopy* **106**:164.
250. Williams D.B. & Carter C.B. (1996*a*) *Transmission Electron Microscopy. Part I.* Plenum Press, New York.
251. Williams D.B. & Carter C.B. (1996*b*) *Transmission Electron Microscopy. Part II.* Plenum Press, New York.
252. Williams D.B. & Carter C.B. (1996*c*) *Transmission Electron Microscopy. Part IV.* Plenum Press, New York.
253. Williams R.C. & Fisher H.W. (1970) *J. Mol. Biol.* **52**:121.
254. Wolf S.E., Müller L., Barrea R., Kampf C.J., Leiterer J., Panne U., Hoffmann T., Emmerling F., Tremel W. (2011) *Nanoscale* **3**:1158.
255. Yang J., Jin Z., Wang X., Li W., Zhang J., Zhang S., Guo X., Zhang Z. (2003) *Dalton Trans.* **2003**:3898.
256. Yuwono V.M, Burrows N.D., Soltis J.A. (2010) *J. Am. Chem. Soc.* **132**:2163.
257. Zhuang J.-L., Lommel K., Ceglarek D., Andrusenko I., Kolb U., Maracke S., Sazama U., Fröba M., Terfort A. (2011) *Chem. Mater.* **23**:5366.
258. Zhukhlistov A.P., Avilov A.S., Ferraris D., Zvyagin B.B., Plotnikov V.P. (1997) *Crystallogr. Rep.* **42**:774.
259. Zhukhlistov A.P. & Zvyagin B.B. (1998) *Crystallogr. Rep.* **43**:950.
260. Zettlemoyer A.C. (1969) *Nucleation*. Marcel Dekker, New York.
261. Zubko M., Wspaniała J., Stróż D., Mugnaioli E. (2013) *Solid State Phenom.* **203-204**:262.
262. Zvyagin B.B. (1967) *Electron Diffraction Analysis of Clay Mineral Structures.* Plenum, New York.